Computer Simulations of Electrostatic Solitary Waves(Dissertation_全文)

AUTHOR(S):

Miyake, Taketoshi

Computer Simulations of Electrostatic Solitary Waves

by

Taketoshi MIYAKE

February 2000

Acknowledgments

I would like to express my sincere appreciation to my research supervisor Prof. Hiroshi Matsumoto for his continual guidance, stimulating and helpful suggestions throughout the present study. I am also grateful to him for providing an opportunity for me to participate in the present study.

I am especially grateful to Dr. Yoshiharu Omura for constructive discussions in analyzing the simulation results in every stage of the present study and a careful reading the entire manuscript and for making a number of helpful suggestions.

I wish to express my deep gratitude to Prof. Kozo Hashimoto for many suggestions and discussions in our laboratory meetings. I also thank him for his careful reading of the manuscript in completing this thesis.

I am indebted to Dr. Hideyuki Usui for his helpful assistance and comments in performing computer simulations. I am also grateful to Dr. Hirotsugu Kojima for his appropriate advises in particular on Geotail data analyses. Dr. Naoki Shinohara also provided many useful suggestions at our laboratory meetings. I would like to express my gratitude for variable advises I received from them.

I wish to express my appreciations to Professors Shoichiro Fukao, Toshitaka Tsuda and Toru Sato, and all the staff of Radio Atmospheric Science Center and Advanced Signal Processing Laboratory in Kyoto University, for their many discussions and suggestions in the seminars.

The computer simulations in the present study are performed with the two-dimensional electrostatic particle code based on KEMPO, which has been developed for more than two decades by a lot of researchers in Radio Atmospheric Science Center. I am very grateful to them for developing such a useful and powerful tool in investigating nonlinear plasma phenomena in space.

The present study is mainly based on the data analyses of the Geotail spacecraft carried out with help of lots of researchers. This thesis was motivated by the Geotail plasma wave data analyses conducted by the Geotail/PWI team. I am very grateful to the members of the Geotail/PWI team.

Many thanks are also due to Messrs. Takeshi Miura, Koichi Shin, Yoshikatsu Ueda and all the colleagues of Matsumoto and Hashimoto Laboratories of Radio Atmospheric Science Center in Kyoto University for their kind assistance and useful discussions. I also thank to Mrs. Keiko Miwa, Tomomi Kawamata and other assistants in the laboratories for their kind encouragements in completing the present work.

All the computer simulations in the present study were performed on the KDK and AKDK computer system at Radio Atmospheric Science Center of Kyoto University.

Finally, I thank my parents and my grandparents for their hearty encouragement and continual support throughout the present study.

Abstract

The waveform observations by the Geotail spacecraft discovered a lot of new natures of plasma waves in the Earth's magnetosphere. One of the most splendid discoveries is Electrostatic Solitary Waves (ESW), which has been observed as Broadband Electrostatic Noise (BEN). The Geotail spacecraft observed the waveforms of BEN emissions, and found they are composed of sequences of impulsive solitary waves. These impulsive solitary waves are termed ESW. This thesis is devoted to clarify the generation mechanism of ESW via one- and two-dimensional electrostatic particle simulations.

In the present study, we investigated generation mechanisms of two types of ESW observed in different regions. One is observed by the Geotail spacecraft in the Earth's PSBL region. This ESW has a weak electric field and an one-dimensional spatial structure uniform in the direction perpendicular to the ambient magnetic field. The other is observed by the FAST and the Polar satellites in the auroral region. This ESW has a strong electric field and a two-dimensional spatial structure. According to the Geotail observations and previous simulation studies of electron beam instabilities, we proposed a generation model of ESW that electrostatic potentials of ESW are stable BGK potentials, and these BGK potentials are generated through nonlinear evolutions of some kinds of electron beam instabilities. We performed computer simulations to confirm our generation model of ESW. To perform one- and two-dimensional electrostatic particle simulations efficiently, we developed a new electrostatic particle code (kuES2) based on KEMPO. This simulation code is optimized to one- and two-dimensional electrostatic particle simulations with a huge number of superparticles.

At first, we performed one-dimensional electrostatic particle simulations without ion dynamics of three typical electron beam instabilities, and confirmed that isolated electrostatic potentials are formed through nonlinear evolutions of the two-stream instability and the bump-on-tail instability. These potentials are very stable for a long time, and they are thought to be BGK potentials, which are assumed as the stable potentials of ESW. Next, we further performed one-dimensional simulations with ion dynamics, and estimated effects of the ion dynamics on the formation mechanism and the long time stability of ESW. We confirmed ESW formed from the two-stream instability are critically affected and tend to be diffused by the ion dynamics. On the other hand, ESW formed from the bump-on-tail instability are hardly affected by the ion dynamics. We compared these results of the one-dimensional simulations and ESW observations of the Geotail spacecraft and those of the FAST and the Polar satellites, and concluded that ESW are generated by the bump-on-tail instability in the Earth's PSBL region, and ESW are generated by the two-stream instability in the auroral region.

On the basis of the results of the above one-dimensional simulations, we performed two-dimensional electrostatic particle simulations and confirmed spatial structures of ESW excited by the electron beam instabilities and their stabilities in the two-dimensional system. At first, we performed two-dimensional simulations of the bump-on-tail instability as a generation mechanism of ESW in the Earth's PSBL region and confirmed formation of clear one-dimensional ESW. In this formation process of ESW, the strength of the magnetic field is a controlling parameter of the coherency of ESW in the direction perpendicular to the ambient magnetic field. In simulation runs with weaker magnetic fields, ESW are much more coherent even in the initial state. In the nonlinear stage, however, potentials are aligned in the perpendicular direction, forming uniform one-dimensional potentials due to the potential striation process. These simulation results are consistent with the Geotail observations that the clear one-dimensional ESW are observed in the Earth's PSBL region, where the magnitude of the magnetic field is very weak.

Next, we performed two-dimensional simulations of the electron two-stream instability as a generation mechanism of ESW in the auroral region and confirmed the formation of isolated two-dimensional ESW. We performed simulation runs of two types of the two-stream instabilities, the cold and the warm two-stream instabilities. The cold two-stream instability excites isolated two-dimensional ESW due to the existence of the quasi-perpendicular electrostatic whistler waves. In a long time evolution, however, these two-dimensional potentials gradually diffused by the strongly excited electrostatic whistler mode waves. On the other hand, the warm two-stream instability excite very stable one-dimensional ESW without ion dynamics. In the simulation run with ion dynamics, however, the lower hybrid waves are excited through coupling with parallel drifting potentials. These lower hybrid waves separate potentials in the direction perpendicular to the ambient magnetic field, forming isolated two-dimensional potentials. These potentials are very stable for a long time. The spatial scale of these two-dimensional potentials is almost equal to the ion Larmor radius. These natures of the isolated two-dimensional potentials are consistent with the observations of ESW in the auroral region. In a long time evolution, these isolated two-dimensional potentials are gradually aligned in the perpendicular direction again due to the potential striation process. This indicates that the perpendicular spatial scale of the two-dimensional ESW becomes larger as time goes on. Therefore, the perpendicular spatial scale of such two-dimensional ESW will be larger in a far region than those in a near region from their generation point.

Contents

List of Figures

List of Tables

Chapter 1

General Introduction

The International Solar-Terrestrial Physics (ISTP) mission was planed in the 1980s, as the international cooperation in space program. This is proceeded under the cooperation of ISAS (Institute of Space and Astronautical Science), NASA (National Aeronautics and Space Administration) and ESA (Europe Space Agency). A fleet of spacecraft have been deployed in space to study the solar-terrestrial environment surrounding the Earth. [Figure 1.1]. The ISTP fleet and a part of related spacecraft shown in Figure 1.1 are listed in Table 1.1.

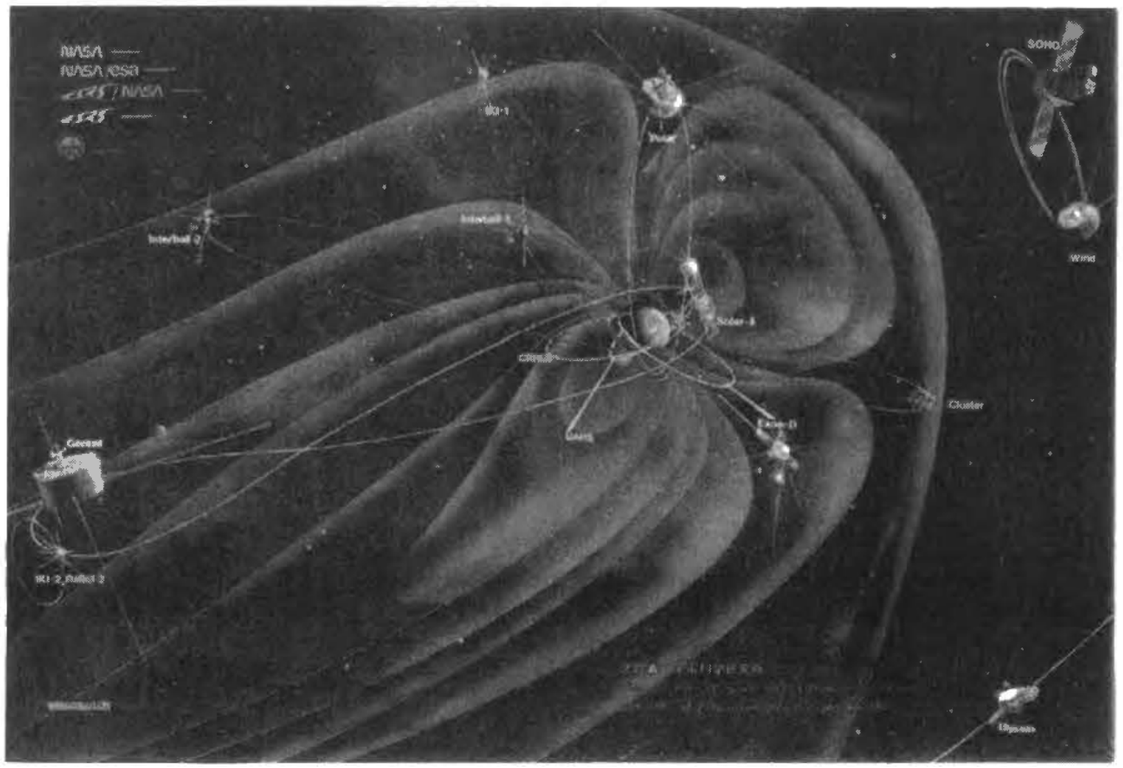

Figure 1.1: Orbits of several spacecrafts related to International Solar-Terrestrial Physics (ISTP) program [*Copyright ISAS/ISTP*].

The ISTP mission has started by the successful launch of the first spacecraft, Geotail, in 1992. In the present study, we focus on one of the highly nonlinear phenomena observed by

Spacecraft	Agency	Mission	Region
Geotail	ISAS(Japan), NASA(US)	July 26, 1992~	Magnetotail
Wind	NASA(US)/ESA(Europe)	Nov. 1, 1994~	Solar wind
SOHO	ESA(Europe)	Dec. 2, 1995~	Sun
Polar	NASA(US)	Feb. 24, 1996~	Polar region
IMP-8	NASA(US)	Oct. 26, 1973~	Magnetotail/Solar wind
Ulyssees	NASA(US)	Oct. 6, 1990~	High latitude solar wind
Interball(Tail)	IKI(Russia)	Aug. 3, 1995~	Magnetotail
Interball(Auroral)	IKI(Russia)	Aug. 29, 1996~	Polar region
Equator-S	ESA(Europe)	Dec. 2, 1997~	Near Earth Equator

Table 1.1: ISTP and related spacecrafts

the Geotail spacecraft, which is the Japanese contribution to the ISTP mission. The detailed information of the spacecraft which collaborate with the ISTP fleet is summarized by *King* [1997].

As the background of the present study motivated by the ISTP mission, we provides brief descriptions of natures of the Earth's magnetotail region and the auroral region, a review of Broadband Electrostatic Noise (BEN) observations, a significance of computer simulations and a contribution of the present work, in the following sections.

1.1 Earth's magnetosphere

The Earth has a dipole magnetic field and it interacts with the solar wind which is a supersonic plasma flow ejected from the sun [*Parker*, 1958]. Because of this interaction, the magnetic field lines of the Earth are trailed out behind the Earth in the anti-sunward direction [*Chapman*, 1931]. In the dayside region, the field lines are compressed. This deformed magnetic field of the Earth is called "magnetosphere". The magnetosphere consist of various regions of characterized by different plasma and magnetic field parameters. Among various regions in the Earth's magnetosphere, we focus on plasma waves observed in two regions, "geomagnetic tail" and "auroral region", in the present study. We introduce these two regions in the following subsections.

1.1.1 Geomagnetic tail

The structure of the Earth's magnetosphere is largely different between in the dayside region and in the nightside region. The dayside magnetosphere is compressed by the solar wind by generally maintains dipole-like configuration. On the contrary, the nightside magnetosphere is a cylindrically-shaped region looks like a tail. The nightside tail-like region of the magnetosphere is called "geomagnetic tail" or "magnetotail". Such a static structure of the magnetosphere is theoretically expected by *Chapman and Ferraro* [1931], and the geomagnetic tail was discovered by *Ness* [1965], using the IMP 1 satellite. This static structure of the geomagnetic tail is schematically illustrated in Figure 1.2 [*Lui*, 1987].

A large portion of the magnetotail consists of two low density region known as the tail lobes, one is the northern half of the magnetotail and the other is the southern half. These

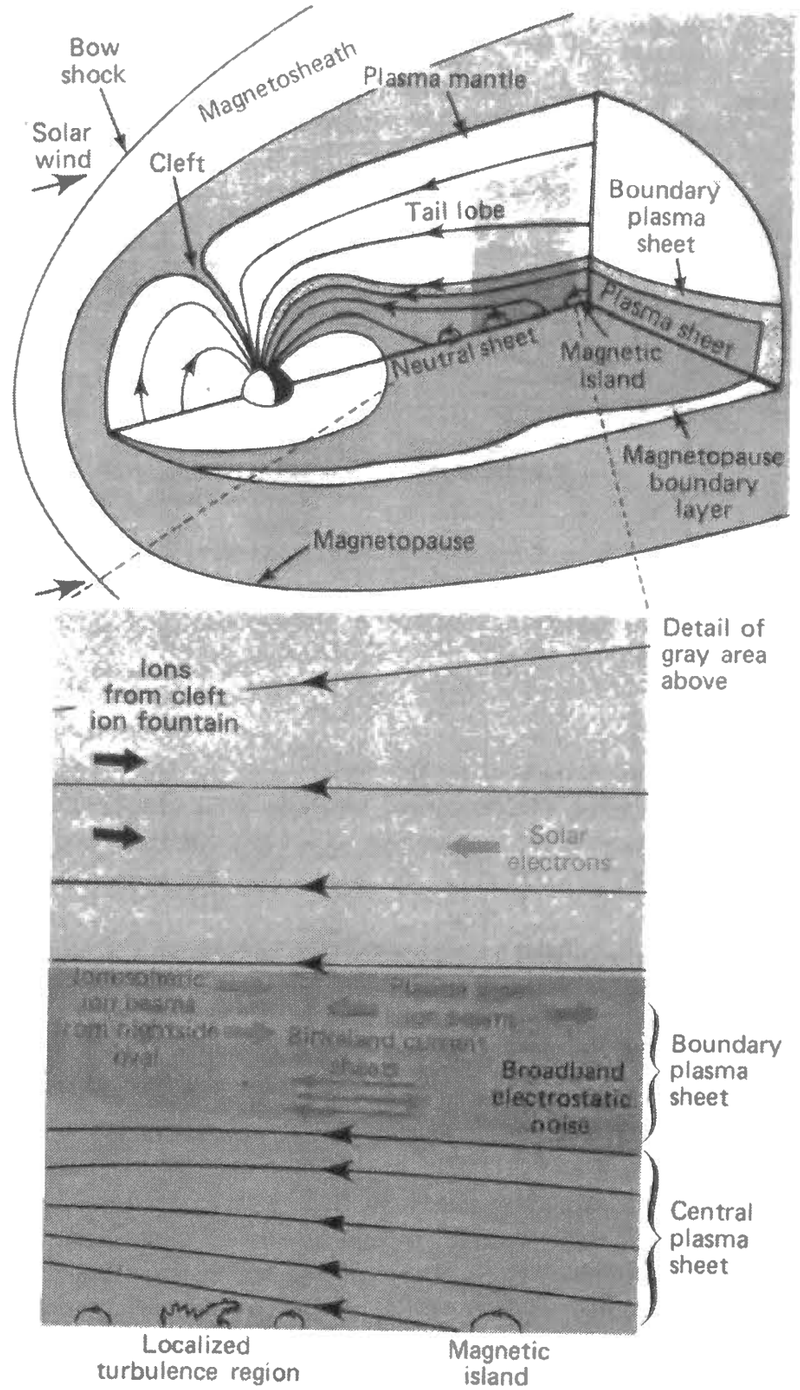

Figure 1.2: Three-dimensional drawing of the geomagnetic tail region [*after Lui*, 1987].

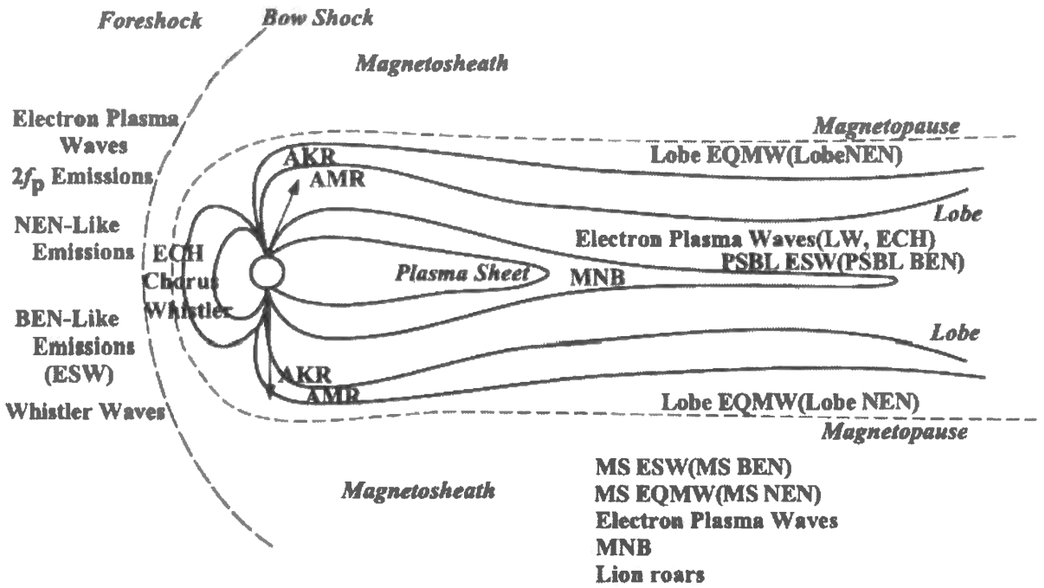

Figure 1.3: Plasma wave signatures illustrated on the meridian plane around the Earth's magnetosphere [*after Kojima*, 1998].

two half of the tail lobes are separated by the existence of the hot plasmas. This region is called as the plasma sheet which was discovered by *Bame et al.* [1967]. Typical electron and ion temperatures in the plasma sheet are reported as 4.4 keV (protons) and 1.0 keV at 20 R_E [*Speiser*, 1991]. The plasma sheet consists of the plasma sheet boundary layer (PSBL) and the central plasma sheet (CPS).

The PSBL region is characterized by high speed and hot ion flows as well as hot electrons. Magnetic field-aligned currents, flowing earthward or anti-earthward, are often observed in this region. In the PSBL region, plasma wave activities are highest in the Earth's magnetotail. These plasma activities, however, diminish near the central plasma sheet. The plasma waves observed in the PSBL and other regions are summarized by *Matsumoto et al.* [1998] and *Kojima* [1998] on the basis of the Geotail plasma wave observations. This plasma wave signatures is illustrated in Figure 1.3.

The recent Geotail observations reported that there exist two x type neutral lines in the magnetotail region, the near earth neutral line and the distant neutral line, as schematically illustrated in Figure 1.4 [*Mcpherron*, 1991]. The x type neutral lines are thought to be associated with the magnetic reconnections. The near earth neutral line is a new discovery of the Geotail observations. The Geotail observation results show that the near earth neutral lines are located between -20R_E and -30 R_E [*e.g.*, *Nishida et al.*, 1996; *Nagai et al.*, 1997, 1998]. On the other hand, the existence of the permanent distant neutral line is suggested by the ISEE-3 observations of magnetic field and plasma measurements [*e.g.*, *Cowley et al.*, 1984; *Baker et al.*, 1984; *Slavin and Kamide*, 1986]. The locations of the distant tail neutral lines are generally found in the downstream distances between -100 R_E and -200 R_E.

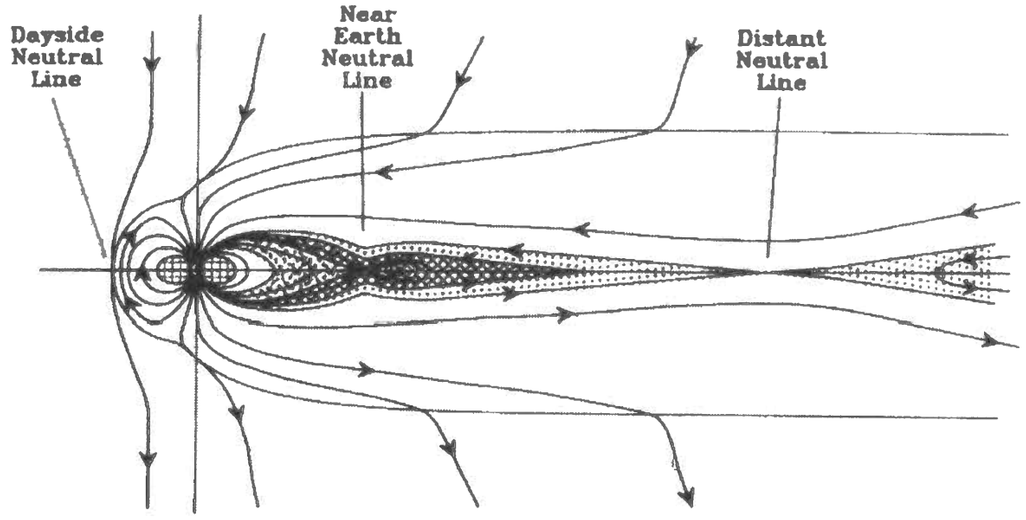

Figure 1.4: An approximate scale drawing showing the formation of neutral lines in the magnetotail [*after Mcpherron*, 1991].

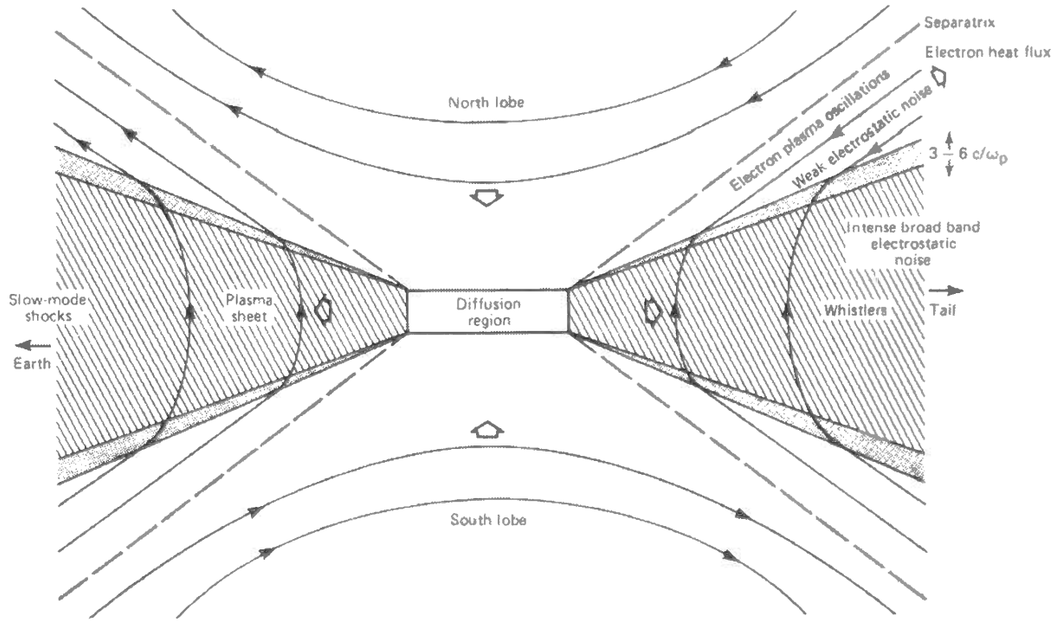

Figure 1.5: Illustration of the key features of the slow-mode shock [*after Feldman et al*, 1984 and *Scarf et al.*, 1984].

Such x type neutral lines accompany slow-mode shocks. The presence of these shocks was predicted about three and a half decades ago by some theories on the magnetic reconnection [*Petschek*, 1964], which suggest that slow-mode shocks should be formed at the plasma sheet boundary layers. Figure 1.5 is a schematic diagram of the slow-mode shocks together with some key features that have been reported. Such x type reconnection lines and accompanied slow-mode shocks are important for plasma wave physics. At x type reconnection line, the magnetic field energies convected with the inflowing plasmas are converted to kinetic and thermal energies of particles, which is forced to flow out along the interface. Such energetic particles are further accelerated at the slow-mode shock, electron and ion beams are formed. These electron and ion beams are important free energy sources of plasma waves around the plasma sheet. Especially, such energetic electron beams are thought to be energy sources of plasma waves which we study in the present study.

1.1.2 Auroral region

Auroras represent one of the most dynamic products of a solar wind-magnetized planetary system. Auroral lights are produced when energetic particles are precipitated into the Earth's ionosphere. The different auroral colors come from the atmospheric emissions characteristic of the excited constituents. There is now agreement that photon emission is controlled directly by the energy flux carried by electrons into the atmosphere [*Omholt*, 1959; *Bryant et al.*, 1970; *Lepine et al.*, 1979; *McEwen et al.*, 1981] and measurements from the DMSP satellite [*Fennell et al.*, 1981] give further reassurance on this point.

An auroral curtain or arc is produced by an electron sheet beam. Its energy spectrum is characterized by a mono-energetic peak [*e.g.*, *Burch*, 1991]. The observations of such beam-like distributions of precipitating electrons above auroral arcs led researchers to conclude that there are electrostatic-potential drops above auroral arcs that act to accelerate the electrons downward [*e.g.*, *Hoffman and Evans*, 1968; *Heikkila*, 1970; *Albert and Lindstrom*, 1970; *Evans*, 1975; *Bosovsky*, 1992]. The S3-3 satellite observation showed that the electron sheet beam is formed by the potential structure with a V-shaped geometry at an altitude of about 3000 to 10,000 km on the auroral field lines [*e.g.*, *Mozer et al.*, 1980]. The potential drop along the geomagnetic field lines is several kV, and it accelerates electrons downward and ions upward. Accelerated electrons and ions gain energy of several keV. Such potential drops are thought to be so-called "double layers".

Figure 1.6 shows a sketch depicting the equipotential contours of a double layer structure above an auroral arc [*Borovsky*, 1993]. Two types of double layers are proposed as those accelerating electrons above in the auroral region, one is a strong double layer (SDL) [*e.g.*, *Knorr and Goertz*, 1974; *Borovsky*, 1988, 1993] and the other is a series of Weak Double Layers (WDL) [*e.g.*, *Koskinen et al.*, 1987; *Boström et al.*, 1988; *Mälkki et al.*, 1989]. Here, "strong" (or "weak") means that the potential energy of double layer is larger (or smaller) than thermal energies of background electrons as follow:

$$\begin{aligned} e\phi_{\text{potential}} &\geq T_e : \text{ Strong Double Layer} \\ &\leq T_e : \text{ Weak Double Layer} \end{aligned} \tag{1.1}$$

where e is the electron charge, $\phi_{\text{potential}}$ and T_e present an electrostatic potential of WDL and thermal energies of background electrons, respectively.

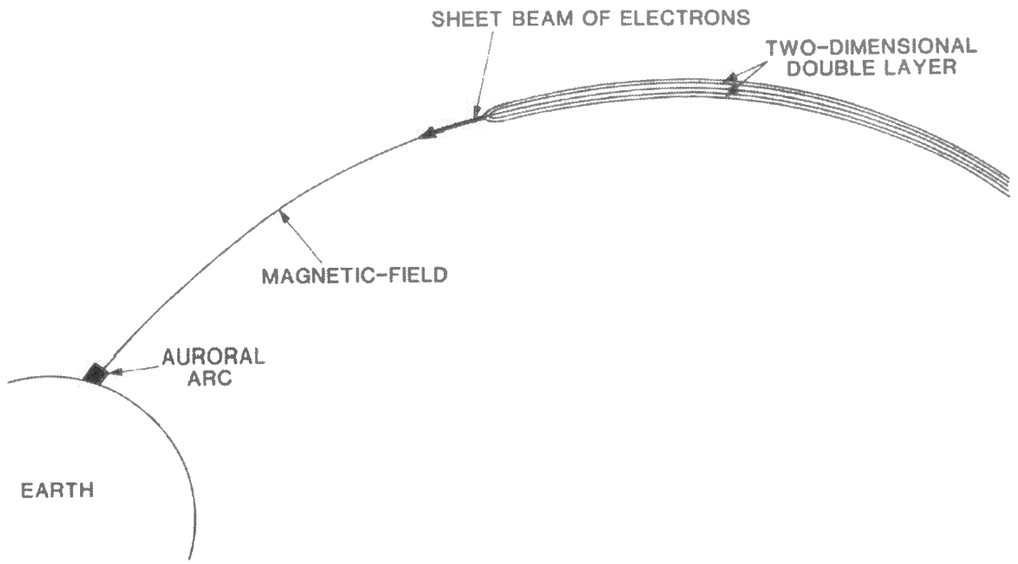

Figure 1.6: Schematic illustration (not to scale) of the equipotential contours of a double layer structure above an auroral arc [*after Borovsky*, 1993].

The presence of the parallel potential drop suggests that plasma waves are excited in this region. If plasma waves are not excited, the potential drop is immediately canceled since electrons can move easily along the magnetic field line. The potential drop is furthermore necessary to maintain the field-aligned currents that flow between the ionosphere and the magnetosphere. The reason is as follows: the carrier of the field-aligned current is usually electrons, therefore if the potential drop does not exist along the magnetic field line, a large part of precipitating electrons is reflected above the ionosphere due to the converging magnetic field geometry, as schematically illustrated in the left panel of Figure 1.7. If the auroral potential structure develops, however, the electric field in the structure accelerates the electrons downward so that it can descend to the lower ionosphere by acquiring a few keV of energy, as illustrated in the right panel of this figure. As a result, the amount of the field-aligned current carried by magnetospheric electrons is limited. Nevertheless, the field-aligned current is enhanced greatly during a magnetospheric substorm. In such a case, the parallel potential drop should be generated to reduce drastically the amount of reflected electrons. The plasma waves related to the parallel potential drop are, for example, ion acoustic waves and electron ion cyclotron waves. These waves cause the scattering of electrons and ions and produce anomalous resistivity along the geomagnetic field lines. Due to these effects of accelerated or scattered electrons and ions, many kinds of plasma waves are observed in the auroral region, as schematically illustrated in Figure 1.8.

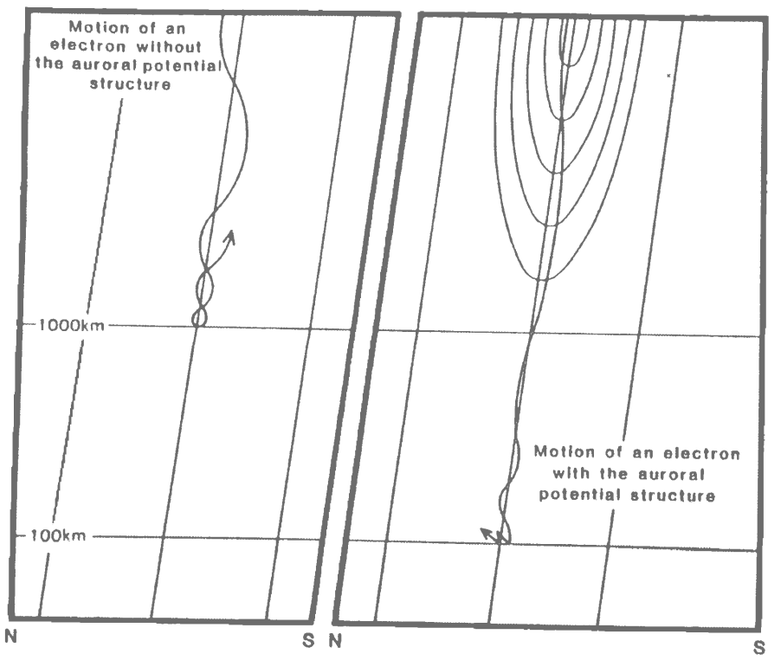

Figure 1.7: Schematic illustrations of motion of a current-carrying aurora electron with (right panel) and without (left panel) the auroral potential structure [*after Akasofu and Kamide*, 1987].

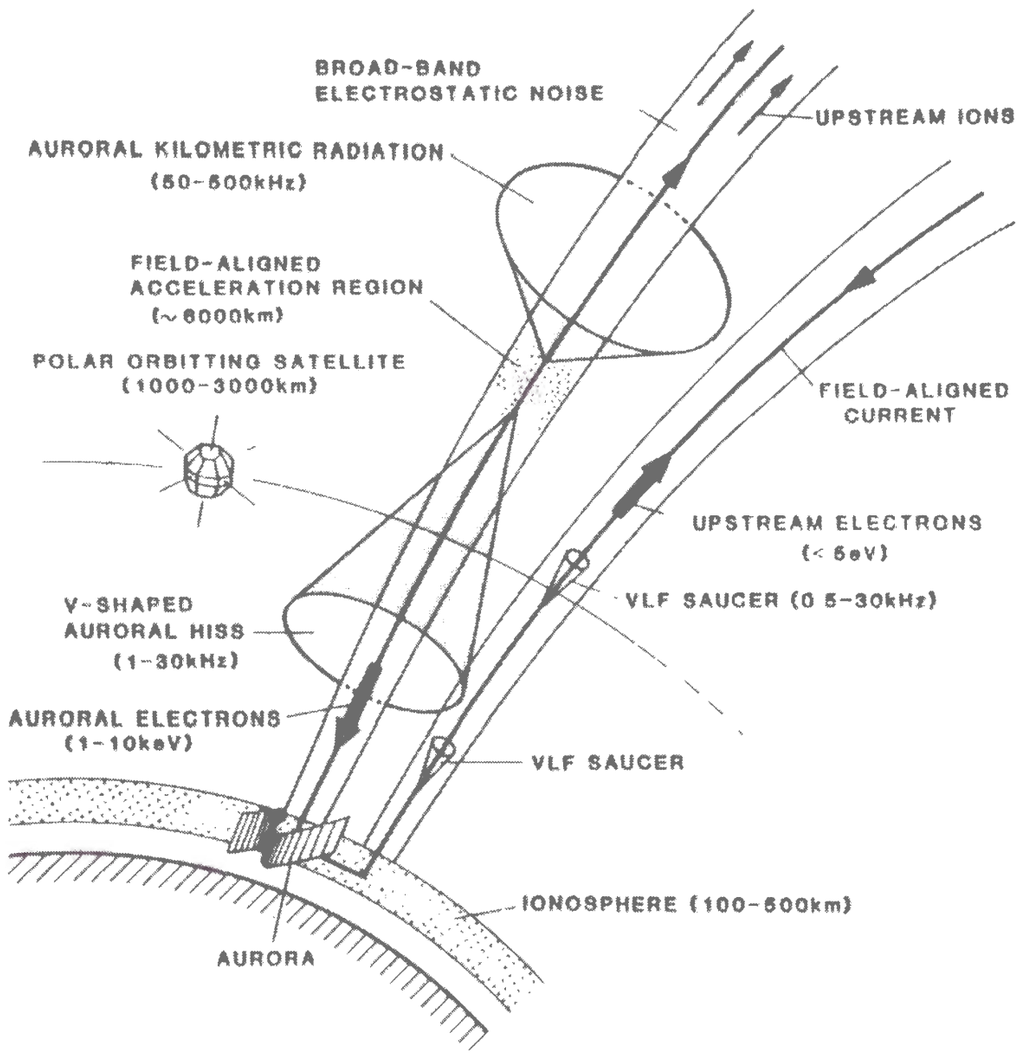

Figure 1.8: Plasma wave signatures associated with downward auroral electrons in the auroral region [*after Fukunishi*, 1987].

1.2 Review of BEN observations

Among many kinds of plasma phenomena observed in the near Earth space, "Broadband Electrostatic Noise (BEN)" emissions are one of the most interesting plasma waves. BEN emissions were first observed in the Earth's magnetotail region by the IMP 7 and 8 spacecrafts [*Scarf et al.*, 1974; *Gurnett et al.*, 1976] and later by other satellites, such as ISEE [*Cattell et al.*, 1986]. The similar broadband emissions are reported in the various regions of the Earth's magnetosphere, i.e., dayside auroral region [*Dubouloz et al.*, 1991b], cusp/cleft regions [*Pottelette et al.*, 1990], magnetosheath [*Kojima et al.*, 1997] and bow shock [*Matsumoto et al.*, 1997]. BEN emissions are also reported to be observed around the Space Shuttle orbiter [*Shawhan et al.*, 1984; *Hwang et al.*, 1987].

Gurnett et al. [1976] reported detailed natures of BEN emissions using the plasma wave data observed by the IMP 8 spacecraft, which passes through the magnetotail at radial distances ranging about 23.1~46.3 R_E. Figure 1.9 represents a typical spectrum of BEN emissions observed by the IMP 8 spacecraft. BEN emissions usually occur over a broad range of frequencies extending from about 10 Hz to a few kHz whose intensities ranging from about 50 μV/m to 5 mV/m. In this figure, there exist a quasi-upper cutoff around a few hundreds of Hz. This quasi-upper cutoff frequency is almost equal to the local electron cyclotron frequency (f_{ce}). BEN emission also have a clear lower cut-off around 10 Hz. The frequency of this lower cut-off is almost equal to the local lower hybrid resonance frequency (f_{LHR}). The wave features of BEN emissions reported by *Gurnett et al.* [1976] are summarized as follows:

1. The noise usually occurs over a broad range of frequencies up to the local electron plasma frequency.
2. They consist of many discrete bursts lasting from a few seconds to several minutes.
3. Their spectrum shows a marked decrease in intensity at the local electron cyclotron frequency.
4. They have a low frequency cutoff corresponding to the local lower hybrid resonance frequency.
5. The electric fields are oriented within ±20° from perpendicular to the magnetic field.
6. BEN emissions are usually observed in the plasma sheet boundary.

The generation mechanism of BEN emissions had not been clarified. Linear theories cannot explain the above natures of BEN emissions because they have very wide frequency range and they are very sudden phenomena with a very short period of duration. Many scientists have proposed various models for generation mechanism of BEN emissions based on the particle distributions in the PSBL region [*e.g.*, *Onsager et al.*, 1990]. Since there exist high-energy ion flows in the PSBL region [*e.g.*, *Frank et al.*, 1976; *DeCoster and Frank*, 1979] and BEN emissions are frequently observed with such high-energy ion flows [*Gurnett et al.*, 1976], BEN have been regarded as being generated via ion beam driven instabilities. They are first studied by a linear instability analysis [*Grabbe and Eastman*, 1984], and have been developed further in several papers such as the ion-ion two stream instability [*e.g.*, *Akimoto and Omidi*, 1986; *Grabbe*, 1987; *Schriver and Ashour-Abdalla*, 1990], the ion beam acoustic instability [*e.g.*,

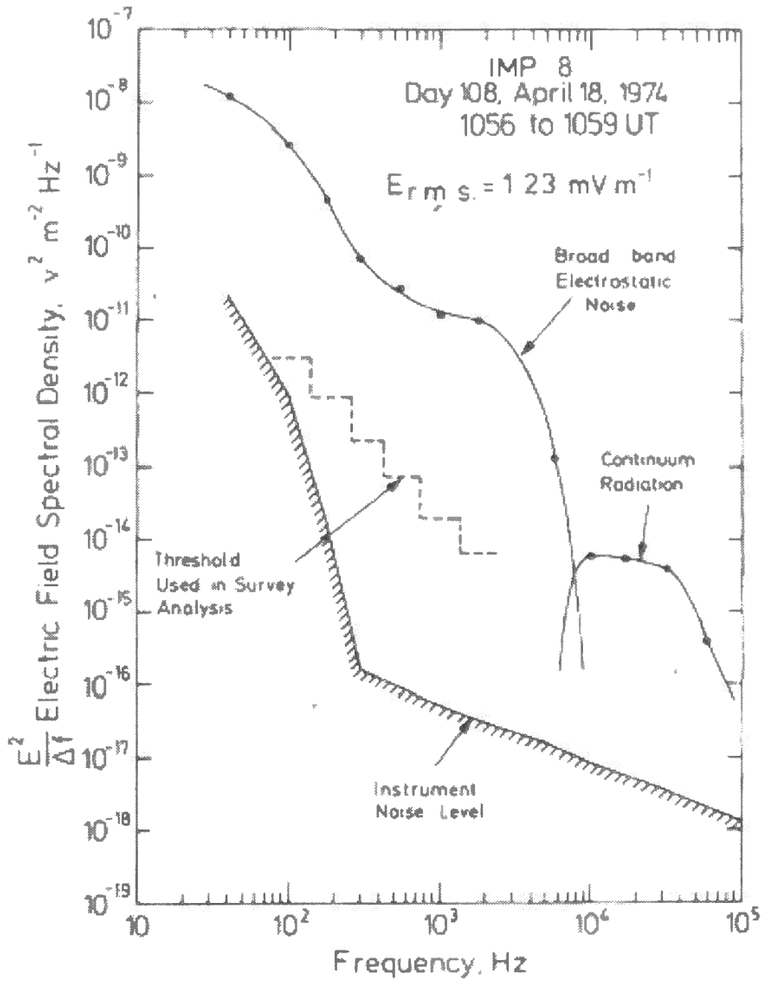

Figure 1.9: Typical frequency spectrum of the broadband electrostatic noise observed by the IMP 8 spacecraft [*after Gurnett et al.*, 1976].

Grabbe and Eastman, 1984 *Dusenbery and Lyons*, 1985; *Omidi*, 1985; *Akimodo and Omidi*, 1986; *Ashour-Abdalla and Okuda*, 1986a, b; *Dusenbery*, 1986; *Grabbe*, 1987; *Burinskaya and Meister*, 1989, 1990], the Bunneman instability [*Grabbe*, 1985, 1989], and their combinations [*Schriver and Ashour-Abdalla*, 1987, 1989]. In addition, *Tsutsui et al.* [1991] considered the ion flow as the plasma bulk flow to provide the Doppler shift, and they attempted to explain the broad frequency characteristics of BEN by the Doppler shift of ion acoustic potential bubbles convecting with the plasma bulk flow. Another proposed generation model was, for example, based on the lower hybrid drift instability (LHDI) [*Huba et al.*, 1978].

On the other hand, *Parks et al.* [1984] demonstrated the relation of BEN emissions and electron beams based on observations by the ISEE-1 spacecraft. Further detailed analysis on the relation of BEN emissions and electron distributions were conducted by *Onsager et al.* [1993]. They showed that BEN emissions can be observed in the electron layer of the outer PSBL without energetic ions. They pointed out that the ion streaming is not essential in the excitation of BEN emissions and BEN emissions have the close relation to the electron dynamics.

The above proposed generation mechanisms are based on destabilized normal mode waves. However, *Nishida et al.* [1985] pointed out that the high frequency component ($f > f_{ce}$) of BEN emissions is not a normal mode. They suggested the possibility that the high frequency component of BEN emissions corresponds to a kind of potential structures.

In spite of the above observational and theoretical efforts, the clear answers to the generation mechanism of BEN emissions had not been obtained. The main difficulty for explaining the excitation mechanism of BEN emissions is originated from the broadness as well as the strength of their spectrum. In order to explain the broadness of the BEN spectra, it is necessary to combine some other instabilities.

1.3 Significance of computer simulations

The space exploration has been achieved by a rapid development of space vehicles and their use for science survey of space environment. In 1960's and 1970's a lot of discoveries of new phenomena were brought from these spacecraft observations. Data analysis-phase followed after the discovery-phase yielding a variety of physical models of space environment and theories for the related plasma processes taking place therein. However, there still remains a large number of problems because of too many possibilities in selecting physical models. Natural phenomena in space plasmas are often highly nonlinear and too complicated for analytic theories which usually rely on linearization or weak nonlinearization, symmetry characteristics, homogeneity or simple inhomogeneity and other simplified assumptions. On the other hand, observations by satellites are still too coarse because measurements are limited in time and especially in space, so that much ambiguity is left. This causes disputes among related theoretical models. To resolve these uncertainties, among various models and theories and to find a hint or clue for understanding the unsolved physics underlying the observed phenomena, computer simulations have been high lighted as a third promising approach to bridge the traditional two approaches, theory and observation, among space researchers from late 1970's.

Owing to the rapid development of computer resources in the last decade, computer simulations become powerful and useful tools to investigate nonlinear plasma phenomena in space. Especially particle simulations which follow the individual nonlinear motions of many particles

in their simulations play a significant role in space physics in their self-consistent fields. The particle simulations become an efficient method in space physics in interpreting highly nonlinear kinetic effects like wave instabilities and associated plasma scattering, diffusion, heating and particle acceleration, so called wave-particle interaction.

Complicated and sometimes overlapping phenomena whose nature generally exhibits can be decomposed into simpler elements of physics in simulations to obtain a clearer physical picture. One of the advantages of the computer simulations is that one can make as detailed diagnostics of plasma and field quantities as one desires. A precise visualization of the time evolution of graphic displays of the results of particle simulations. This could not be realized either by theories nor by satellite observations. Thus particle simulations provide useful data of nonlinear wave-particle interactions which are currently inaccessible to satellite observations nor to theories. One such example is a rapid variation of the particle distribution function in inspiration not only for further theoretical development but also for design of new satellite observations.

1.4 Contribution of the present work

The present paper describes the formation mechanism of Electrostatic Solitary Waves (ESW) via one- and two-dimensional computer simulations. At first, we introduce ESW observations by the Geotail spacecraft and some other satellites in several regions in the Earth's magnetosphere, and show ESW generation model based on these observations and the previous simulations. We performed one- and two-dimensional electrostatic particle simulations of ESW formation, and discuss the generation mechanism of ESW and parametric dependence on the formation and the stability of ESW.

In Chapter 2, we present satellite observations of two types of ESW studied in the present thesis. We show the Geotail observations of ESW in the Earth's magnetotail region and ESW observation by other satellites such as FAST and POLAR in the auroral region. We summarize characteristics of these two types of ESW based on the satellite observations, and present ESW potential model which is assumed by the Geotail/PWI team based on the waveform analyses of the Geotail/WFC observations.

In Chapter 3, we present linear and nonlinear theories related to the generation model of ESW presented in Chapter 2. We consider that ESW are generated through nonlinear evolution of certain kinds of electron beam instabilities. We assume three possible electron beam instabilities to generate ESW in space plasma. Then we examine a linear dispersion analysis on these three electron beam instabilities, and estimate linear effects of the magnitudes of the static magnetic fields and the propagation angles of waves in these instabilities. In addition, we present BGK theory and nonlinear trapping theory which are basic as well as important theories in the ESW formation mechanism.

In Chapter 4, we introduce a newly developed two-dimensional electrostatic particle code kuES2 for the present simulation study. We explain the basic equations, the finite-difference scheme and the superparticle model which are adopted in this simulation code. We also mention to two methods in parallelizing particle codes for parallel computers with multiple processors. In addition, we mention to effects of enhanced thermal fluctuations which are not avoidable in particle simulations. We also present one- and two-dimensional simulation models and common system parameters which are used in simulation runs of ESW performed in the present study.

In Chapter 5, we investigate basic mechanism of ESW formation in one-dimensional system and try to clarify necessary conditions for the formation of stable ESW via one-dimensional computer simulations. At first, we perform one-dimensional electrostatic particle simulations of three typical electron beam instabilities, which are assumed in Chapter 3, without ion dynamics, and confirm our assumption that ESW are formed through nonlinear evolutions of electron beam instabilities. Next, we perform a series of simulations with ion dynamics and estimate effects of ion dynamics on the ESW formation from electron beam instabilities. In this chapter, we perform simulations varying several plasma parameters, and analyze their effects on the formation process and the stability of ESW in the one-dimensional system. We compare these one-dimensional simulation results and the satellite observations of ESW, and estimate possible instabilities which generate ESW in the Earth's PSBL region and in the auroral region.

In Chapter 6, we further investigate detailed mechanisms of the ESW formation from electron beam instabilities in two-dimensional system via two-dimensional computer simulations. On the basis of the one-dimensional simulations studied in Chapter 5, we perform a series of two-dimensional electrostatic particle simulations of the electron bump-on-tail instability as a generation mechanism of the one-dimensional ESW observed in the Earth's PSBL region. In this simulation study, we investigate parametric dependence of the formation mechanism and the spatial structures of ESW in the two-dimensional system, especially the coherency of ESW, on the magnitudes of the ambient magnetic field. Next, we perform two-dimensional simulations of the electron two-stream instability as a generation mechanism of two-dimensional ESW observed in the auroral region. We examine a series of simulations without ion dynamics for different plasma parameters of electrons, and discuss parametric dependences of the time evolutions of the spatial structures of ESW. Then, we perform simulation runs with ion dynamics, and investigate effects of ion dynamics on the formation mechanism of ESW with a two-dimensional structure. We summarize the time evolutions of the one- and two-dimensional ESW from the electron beam instabilities, and conclude the formation mechanisms of ESW in the PSBL region and in the auroral region.

In Chapter 7, we summarize the present study and make conclusions. We also present suggestions of future works for development and extension of the space plasma physics via computer simulations.

Chapter 2

Characteristics of ESW

2.1 Geotail observations of ESW

The Geotail spacecraft [Figure 2.1] was launched on July 24, 1992 at the Kennedy Space Center. The scientific objectives of the Geotail Plasma Wave Instruments (PWI) are to study plasma wave phenomena observed in the Earth's magnetosphere. The Geotail/PWI team observe

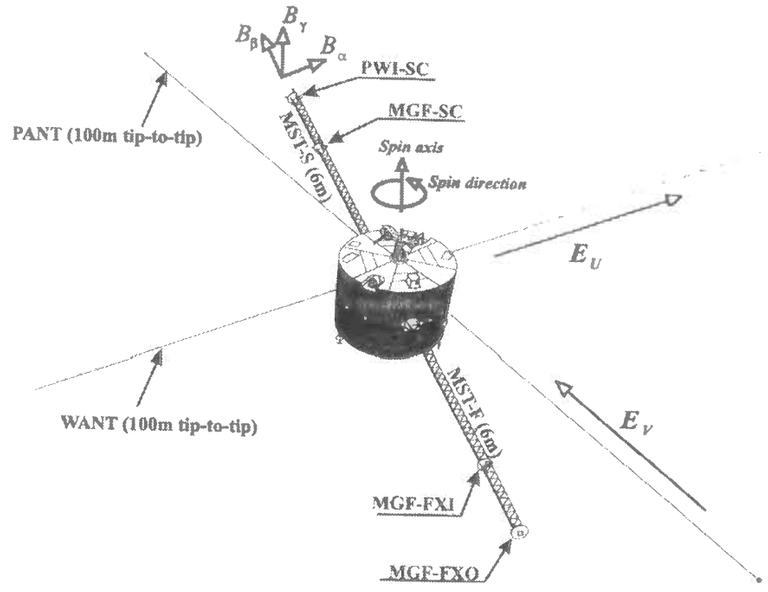

Figure 2.1: Outlook of the Geotail spacecraft [*after Kojima*, 1998].

plasma waves with the following three different sets of receivers on board:

1. Sweep Frequency Analyzer (SFA),
2. Multi Channel Analyzer (MCA) and
3. Wave-Form Capture receiver (WFC).

The SFA and MCA are the standard spectrum receivers with different frequency and time resolutions, while the WFC is a newly designed instrument to receive real waveforms of plasma

waves [*Matsumoto et al.*, 1994a]. The WFC receiver has successfully revealed the waveforms of various electrostatic and electromagnetic emissions. Most of all, the waveforms of BEN emissions have been revealed to have unexpected characteristics.

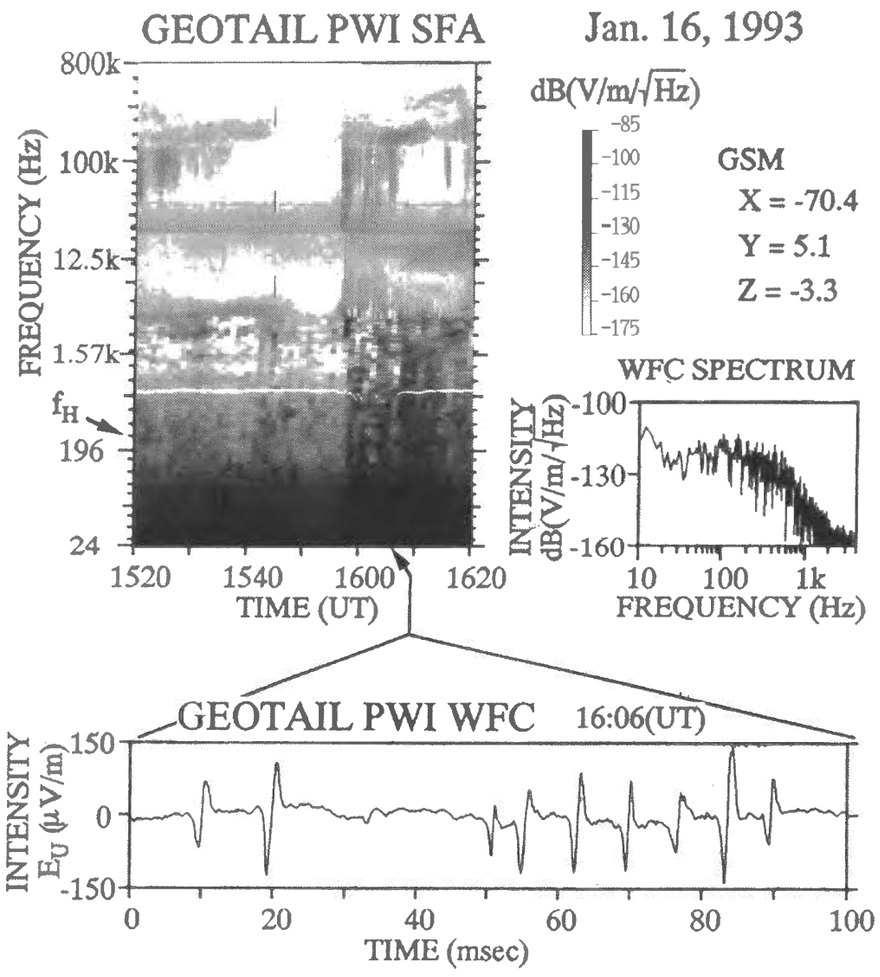

Figure 2.2: Dynamic spectra and waveform of the BEN emission observed by the Geotail spacecraft in the PSBL on Jan. 16, 1993. Left upper panel is the dynamic spectrum obtained from the SFA electric field data. The intensities of waves are indicated by shades with logarithmic scale as shown by the contour bar. The white line in the spectra indicates the local electron cyclotron frequency. Bottom panel is amplitude versus time plot of WFC data, showing the waveform of this BEN emission. Right panel is the spectrum obtained by Fourier transforming of the WFC data.

The Geotail/PWI observed BEN emissions in the Earth's magnetotail region, especially almost always in the PSBL [*Matsumoto et al.*, 1994b]. We present a typical example of the Geotail observation of BEN emissions in the PSBL, at January 16, 1993, in Figure 2.2. The upper panel shows the SFA dynamic spectrum, presenting f-t contour, and the white line

presents the local electron cyclotron frequency. In this diagram, BEN emissions are observed at 15:58~16:25(UT), with frequency range 10Hz~2kHz. The lower diagram is the waveform of this BEN emission at 16:06(UT). This shows that the waveform of BEN emissions are not continuous "noise" but are composed of sequences of impulsive solitary waves, which are called ESW [*Matsumoto et al.*, 1994b]. Since intervals between these adjacent spikes and widths of spikes themselves are random, this emission has a wide frequency range.

Since BEN emissions are frequently observed with a high-energy ion flow [*e.g.*, *Grabbe and Eastman*, 1984; *Schriver and Ashour-Abdalla*, 1990; *Kojima et al.*, 1994], they have been regarded as being generated via ion beam driven instabilities, as noted in Section 1.2. The Geotail/WFC data analysis, however, show the waveforms of ESW change very rapidly, with timescales of 1~50 ms, implying that ESW are related to the electron dynamics rather than those of ions. The amplitudes of electric fields of ESW in the PSBL region are several hundreds μV/m or smaller.

According to the Geotail/WFC data analysis of examining the polarization of the electric fields measured by two antennas, the waveforms of ESW have a spin dependence, which suggests that ESW are propagating in a certain direction. It is revealed that ESW are propagating in the direction almost parallel to the ambient magnetic field [*Matsumoto et al.*, 1994a; *Kojima et al.*, 1997]. Further, *Kojima et al.* [1998] presented a hodogram of electric field components of ESW observed by Geotail on a fixed $E_{\parallel}$-$E_{\perp}$ plane, as shown in Figure 2.3. In this figure, the upper two panels show $E_{\parallel}$ and $E_{\perp}$, and the lower plot is a corresponding $E_{\parallel}$ versus $E_{\perp}$ hodogram. Though a clear solitary wave is shown in the $E_{\parallel}$ plot, no significant wave exist in the $E_{\perp}$ plot. In other words, the polarization of this ESW is completely parallel to the ambient magnetic field. This feature also represents that this ESW has one-dimensional structure uniform in the direction perpendicular to the ambient magnetic field. Since ESW are purely electrostatic emissions, these results suggest that ESW are related to purely electrostatic instabilities along the magnetic field. Since ESW are related to the electron dynamics rather than the ion dynamics, such electrostatic instabilities are thought to be excited by electron beams traveling along the ambient magnetic field.

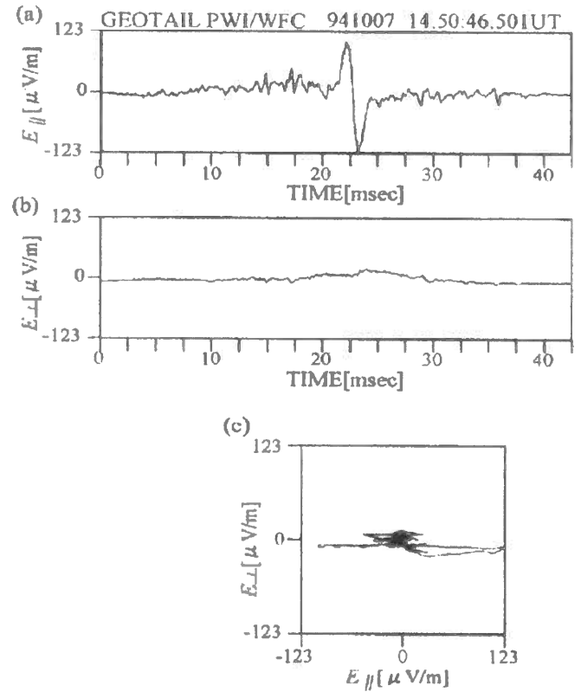

Figure 2.3: ESW waveforms and corresponding hodogram in the $E_{\parallel}$-$E_{\perp}$ plane [*after Kojima et al.*, 1998].

The Low Energy Particle (LEP) instrument on board the Geotail spacecraft [*Mukai et al.*, 1994] can measure three-dimensional velocity distribution functions. *Omura et al.* [1999a] studied waveforms of ESW obtained by the Geotail/WFC data and corresponding electron

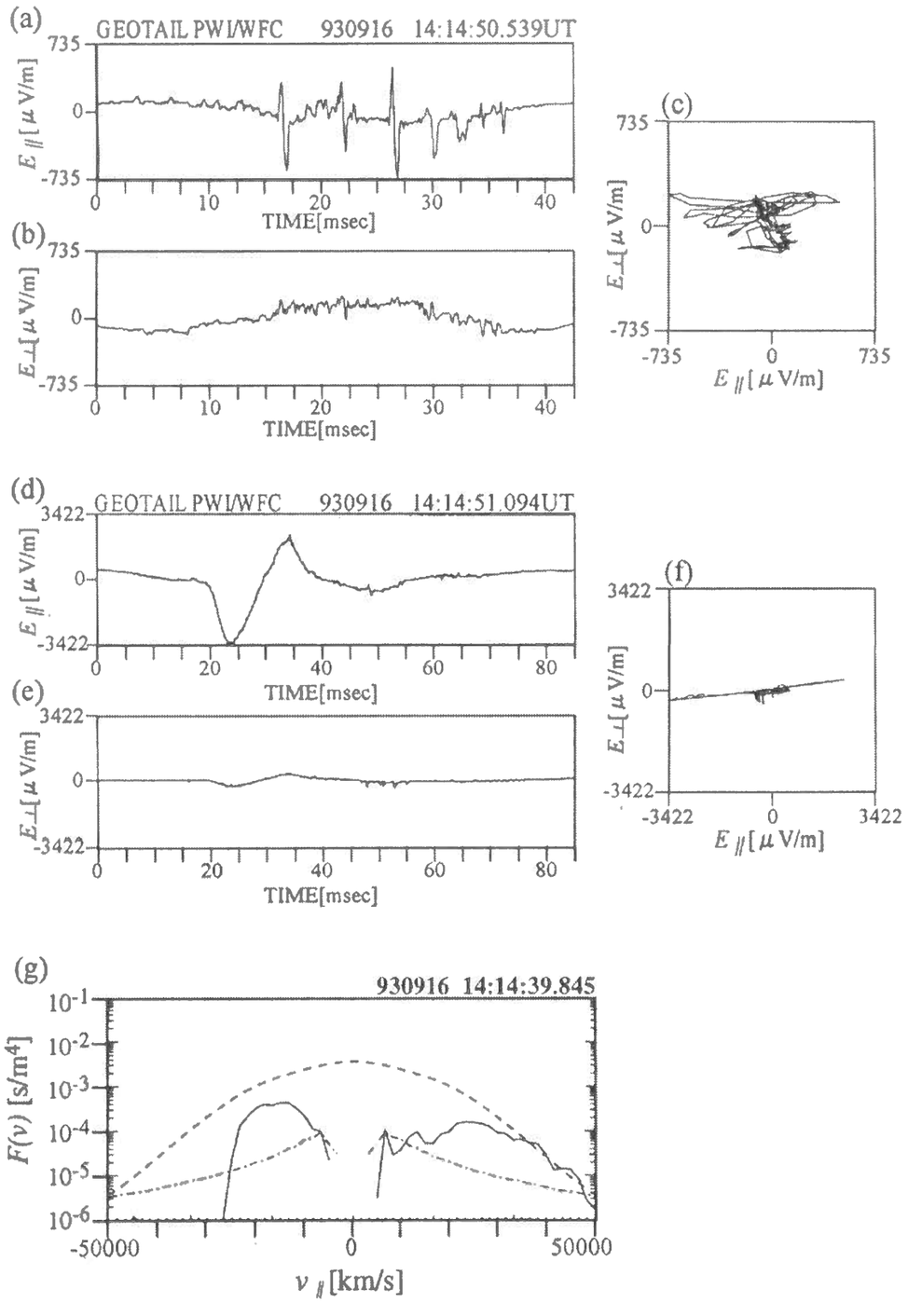

Figure 2.4: Example of electric fields $E_{\parallel}$ and $E_{\perp}$ of ESW (a~f) and corresponding reduced velocity distribution functions of electrons (g) observed by the Geotail spacecraft. Solid line and dashed line correspond to the velocity distribution function of beam electrons and that of bulk electrons, respectively [*after Omura et al.*, 1999a].

velocity distribution functions obtained by the Geotail/LEP data. They found that enhanced fluxes of high-energy electrons flowing along the ambient magnetic field which correspond to a series of ESW in the PSBL of the Earth's magnetotail. This enhanced high-energy electron flux is regarded as the diffused electron beam after saturation of the electron beam instability. There are good correlation between the propagation direction of ESW and the direction of the enhanced high-energy electron flux.

Figure 2.4 shows an example of electric fields $E_{\parallel}$ and $E_{\perp}$ of ESW (a)~(f) and corresponding reduced velocity distribution functions of electrons (g) observed by the Geotail spacecraft in the PSBL region. Some ESW with a short wave length are shown in Figure 2.4(a). These short ESW are revealed to be propagating in the direction parallel to the ambient magnetic field, i.e., the tailward direction. While in Figure 2.4(d), one ESW with a large wave length is shown. This large ESW is propagating in the direction antiparallel to the magnetic field, i.e., the earthward direction. These ESW with different wave lengths are observed during a time period of 8.7 sec, which is a single sampling period of the Geotail/WFC data. On the other hand, two enhanced high-energy electron fluxes in the both parallel and antiparallel direction, i.e., in the tailward and earthward direction, are shown in Figure 2.4(g). The short ESW correspond to the tailward energy flux, and the large ESW corresponds to the earthward energy flux. The good correlation between the propagation directions of ESW and the directions of electron beams is presented in this figure. This correlation indicates that ESW are related to electron beams drifting along the ambient magnetic field, and ESW are drifting with these electron fluxes. This also supports the above assumption that ESW are related to electrostatic instabilities excited by electron beams traveling along the ambient magnetic field.

The characteristics of ESW observed by the Geotail spacecraft are summarized as follows:

1. one-dimensional structure.

2. small amplitude of the electric field.

3. propagating along the ambient magnetic field.

4. related to electron beams drifting along the ambient magnetic field.

Meanwhile, these ESW waveforms mainly contribute to the high frequency component of BEN emissions. Lower frequency part of BEN emissions must be supported by other waves. The polarization of ESW is almost parallel to the ambient magnetic field as noted, on the other hand, the polarization of the lower frequency component of BEN emissions is detected to be almost perpendicular to the ambient magnetic field, as shown in Figure 2.5 [*Kojima*, 1998]. As stated in Section 1.2, *Gurnett et al.* [1976] reported that the electric field orientation of the BEN is almost perpendicular to the ambient magnetic field. This is because they examined the electric field orientation using the frequency averaged spectrum intensities, and we can guess that their obtained electric field orientation is strongly affected by the low frequency component with larger wave intensities and perpendicular polarizations relative to the ambient magnetic field. Unfortunately, we have no clear answer to determine the mode of this low frequency component of BEN emissions.

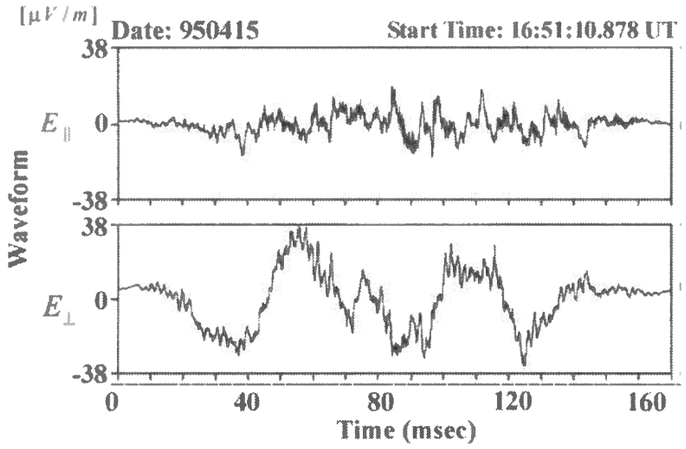

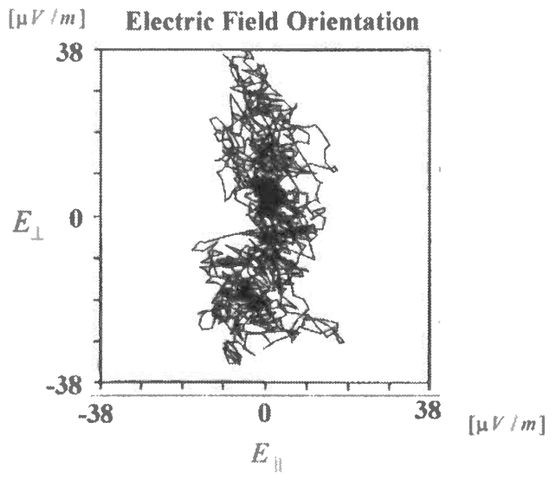

Figure 2.5: Waveforms and electric field orientation of the low frequency component of ESW in the PSBL region [*after Kojima*, 1998].

2.2 ESW observed in the auroral region

Solitary waves similar to ESW observed by Geotail have been also observed by other satellites. Especially in the auroral region, very strong solitary waves have been frequently observed. The initial observation of the solitary waves was reported by *Temerin et al.* [1982]. They found two kinds of solitary structures in the electric field data observed by the S3-3 satellite in the polar magnetosphere at the altitude of 6030 km. They reported to find two kinds of solitary structures in the direction parallel to the ambient magnetic field. Since they are purely electrostatic, these solitary structures correspond to isolated electrostatic potentials. The structures with a net potential drop are referred to as Weak Double Layers (WDL) and those without net potentials as solitary waves (SW). They pointed out that these solitary structures are correlated with upward ion flows and enhanced loss-cone electrons.

More detailed analyses of WDL and SW are conducted by using the observation data of the Viking satellite [*Koskinen et al.*, 1987; *Boström et al.*, 1988]. They observed similar solitary structures associated with density depletions, and showed that the observed solitary structures flow upward along the ambient magnetic field with drift velocities of 5∼50 km/s, and the spatial scale of their potentials is 50∼100 m, which corresponds to about 10 λ_D, where λ_D is the Debye length. They also reported that the observed SW and WDL correspond to negative potentials with amplitudes of 2∼3 V. Further, statistical surveys on these solitary structures are performed using the Viking data [*Koskinen et al.*, 1990; *Mälkki et al.*, 1993, 1994; *Eriksson et al.*, 1997]. They showed that these structures are mostly observed at altitudes between 7000 and 11000 km, and close relations between these solitary structures and upward flowing ions with moderate-energies.

Similar solitary structures have been detected in the lower altitude of the polar region by the Freja satellite [*Dovner et al.*, 1994]. Though waveforms of SW observed by the Freja satellite are very similar to the previous waveforms observed by the S3-3 and the Viking satellites, the characteristics of these solitary structures is completely different from those of ESW observed by the Geotail spacecraft in the Earth's magnetotail region. The solitary structures observed by Freja propagate in the direction perpendicular to the ambient magnetic field with a very slow velocity of 4 km/s.

According to the recent observations, two different satellites observed solitary waves in the polar region. The FAST satellite found solitary waves in burst broadband VLF emissions in the downward current regions of the mid-altitude auroral zone (∼3000 km) [*Ergun et al.*, 1998]. Figure 2.6 shows an example of solitary waves observed by the FAST satellite. In this figure, the left column shows $E_\parallel$ and $E_\perp$, and the right plot is $E_\parallel$ versus $E_\perp$ of the solitary wave. The point in this figure is mono-hump or mono-well structure with a large amplitude in the $E_\perp$ component, which is not found in the waveforms of ESW observed by the Geotail spacecraft. This feature represents that this solitary wave observed by the FAST satellite has two-dimensional structure. This solitary wave has a finite spatial scale in the directions perpendicular as well as parallel to the ambient magnetic field. Since the FAST satellite can measure particle distributions with very high time resolutions, *Ergun et al.* [1998] revealed the modulation of upgoing electron fluxes of ∼100 eV synchronizing with appearance of solitary waves. This modulation is consistent with the result that the estimated positive potential amplitude of solitary waves is about 100 V. They reported that the observed solitary structures propagate upward with a velocity of ∼4500 km/s.

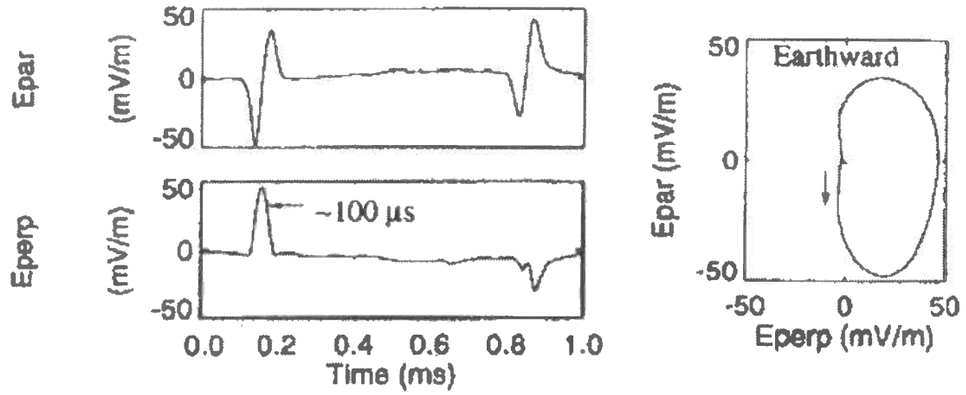

Figure 2.6: Solitary waves observed by the FAST satellite. Right plot is $E_{\parallel}$ versus $E_{\perp}$ of the solitary waves [*after Ergun et al.*, 1998].

The Polar satellite also succeeded in detecting solitary waves in the polar region. [*Mozer et al.*, 1997; *Franz et al.*, 1998]. *Franz et al.* [1998] observed solitary waves shown in Figure 2.7 at radial distances of 2.02 to 8.5 R_E. In this figure, the top panel shows waveforms of the perpendicular electric field component. Waveforms shown in the lower two panels are observed by two mono-pole antennas parallel to the ambient magnetic field at this observation time. We can find that these observed solitary waves also have two-dimensional potential structures. The observed solitary waves correspond to positively charged potentials propagating at velocities of the order of 1000 km/s in the parallel direction relative to the ambient magnetic field. These features are very similar to those of solitary waves observed by the FAST satellite.

The characteristics of solitary waves in the auroral region are summarized as follows:

1. two-dimensional structure.

2. large amplitude of the electric field.

Other features are almost similar to those of ESW observed by the Geotail spacecraft in the PSBL region. Solitary waves have clear two-dimensional structures and large electric fields (even several V/m) in the downward current regions of the mid-altitudes auroral zone observed by the FAST satellite. While in the high altitude polar region observed by the Polar satellite, the amplitude of solitary waves is smaller than that of solitary waves in the auroral zone. In addition, by comparing Figures 2.6 and SW by Polar, we can find that the ratio of parallel and perpendicular electric field $E_{\parallel}/E_{\perp}$ is also smaller. This indicates that solitary wave in the high altitude polar region have larger spatial scale in the perpendicular direction than ESW in the lower altitude.

Since solitary waves were discovered in the auroral region by the S3-3 and the Viking satellites, many theoretical and simulational attempts have been made for explaining their generation mechanism. The candidates for their generation mechanisms are mainly classified in two kinds of waves, the ion acoustic solitons and the ion hole instability. The ion acoustic solitons are proposed as the nonlinear evolutions of beam driven ion acoustic instabilities [*e.g.*,

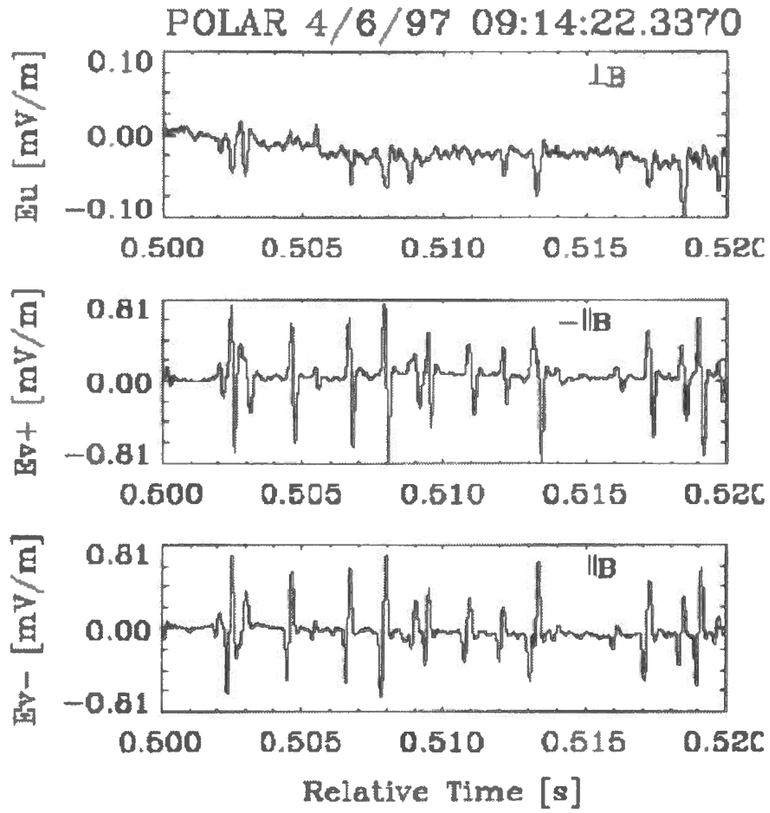

Figure 2.7: Solitary structures observed by the Polar satellite. The E_{U} antenna is roughly perpendicular to the ambient magnetic field, while the $E_{\mathrm{V}+}$ and $E_{\mathrm{V}-}$ antennas are roughly parallel to B_0 [*after Franz et al.*, 1998].

Lotko and Kennel, 1983; *Marchenko and Hudson*, 1995] or the interactions between hot and cold electron components in the presence of a finite ion temperature [*e.g.*, *Berthomier et al.*, 1998]. On the other hand, the quasi-stationary BGK mode is also proposed for generation mechanisms of solitary waves observed by the Viking satellite. The nonlinear evolution to BGK mode is addressed as a phase-space ion hole instability, which is driven by ion-ion two streams or electron currents [*Dupree*, 1982; *Hudson et al.*, 1983]. In these mechanisms, the formation of solitary waves has been successfully confirmed. *Mälkki et al.* [1989] compared observation results from the S3-3/Viking satellites with the results of computer experiments focusing on the above two generation mechanisms. Since the velocities of observed solitary structures are much smaller than those expected by the theory of ion acoustic solitons, they concluded that it seems that the theory of nonlinear ion hole instability is in the best agreement with the observations.

Solitary structures discovered by the S3-3 and the Viking satellite are negatively charged, suggesting ion trapped potentials. Therefore, these theoretical and simulational works are based on ion dynamics. According to recent satellite observations, however, the FAST and the Polar satellites detected positively charged solitary structures in the auroral region, which are similar to ESW observed by the Geotail spacecraft. The generation mechanism of these solitary waves with positively charged potentials are not clarified yet. *Dobouloz et al.* [1991a, 1993] applied the theory of the electron acoustic solitons and showed that it is a plausible generation mechanism to explain solitary structures in the auroral region. They derived soliton solutions of two electron fluids with different temperatures based on the condition in the auroral double layer region. They also tried to explain BEN emissions in the auroral zone by electron acoustic solitons excited due to two different components of electrons. Though this model succeed to explain the wide frequency range of BEN emissions, the growth rate of this electron acoustic instability is very small, and this model cannot explain very strong electric field of solitary waves in the auroral region. Recently, *Tsurutani et al.* [1998] conducted a statistical analysis of broadband plasma waves observed by the Polar satellite. They call these broadband waves as polar cap boundary layer (PCBL) waves, and concluded that these broadband waves are mixture of obliquely propagating electromagnetic whistler mode waves plus electrostatic waves (solitary waves) [*Tsurutani et al.*, 1998; *Lakhina and Tsurutani*, 1999]. This is very similar to the nature of BEN in the PSBL, mixture of ESW and the low frequency component.

Historically, electrostatic solitary structures observed in the auroral region have been termed "Solitary Waves (SW)". These SW have almost the same natures with those of ESW observed by the Geotail spacecraft in the PSBL region, except for the spatial structures and the amplitudes of the electric fields. We regard these "Solitary Waves" in the auroral region as another type of ESW. In the present study, we use the term "ESW" to present both ESW observed in the PSBL region, and SW observed in the auroral region. In other words, we deal with two types of "ESW" in the present study, one is ESW observed by the Geotail spacecraft in the PSBL region of the Earth's magnetotail, the other is ESW observed by the FAST and the Polar satellites in the auroral region.

2.3 ESW potential model

As mentioned in Section 2.1, the Geotail/PWI observed ESW in the PSBL region, and revealed that the waveforms of ESW are composed of sequences of impulsive isolated waves. In this

chapter, we introduced the two different types of ESW observed in the different regions, in the Earth's PSBL region and in the auroral region. Similar solitary waves are also observed in various regions by lots of satellites, i. e., at the Earth's bow shocks by ISEE-1 [*Wygant et al.*, 1987]. Anderson et al. [1982] also reported the very bursty electrostatic waves called "spikes" around the bow shock. They presented only spectrum data, but these "spikes" would have similar impulsive waveforms. The Geotail/PWI further observed ESW at the bow shock transition layer [*Matsumoto et al.*, 1997] and in the distant magnetosheath region [*Kojima et al.*, 1997]. Among these ESW observations, detailed analyses are conducted on those observed in the PSBL region and in the auroral region, as mentioned in the previous two sections. We focus on these two types of ESW, and investigate their generation mechanisms in the present study.

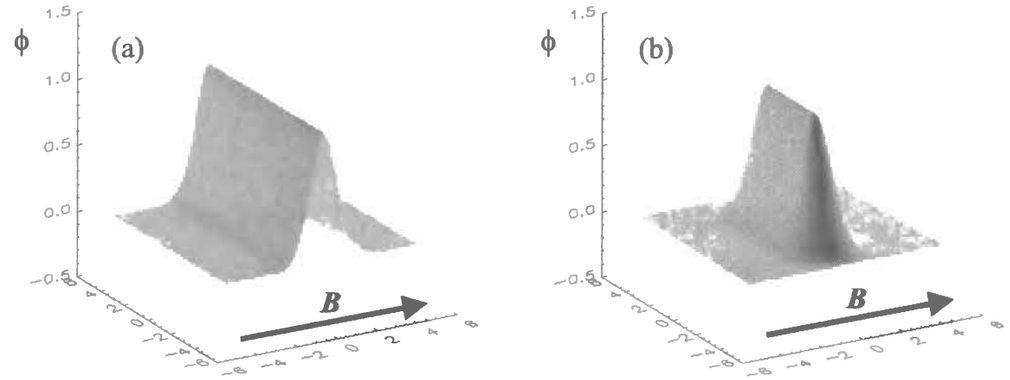

Figure 2.8: Schematic drawings of potential structures of the one- and two-dimensional ESW. (a):one-dimensional ESW observed by the Geotail spacecraft in the Earth's PSBL region; (b):two-dimensional ESW observed by the FAST and Polar satellites in the auroral region.

According to the Geotail/WFC data analyses, the polarization of ESW in the PSBL region is parallel to the ambient magnetic field, as presented in Section 2.1. This indicates that ESW are propagating along the ambient magnetic field. Since ESW are purely electrostatic waves, impulsive waveforms of ESW correspond to sequence of isolated electrostatic potentials. In other words, impulsive waveforms of ESW correspond to a sequence of isolated potentials traveling along the ambient magnetic field passing through the spacecraft. As presented in Figure 2.3, the typical waveform of ESW electric field is only shown in the $E_{\parallel}$ plot. While in the $E_{\perp}$ plot, no significant structure exist. This indicates that the ESW potential have one-dimensional structure uniform in the direction perpendicular to the ambient magnetic field. They look like "trough" as schematically illustrated in Figure 2.8(a).

On the other hand, according to the satellite observations by FAST [*Ergun et al.*, 1998] and Polar [*Franz et al.*, 1998; *Mozer et al.*, 1997], the polarization of ESW in the auroral region is also parallel to the ambient magnetic field, indicating that ESW are propagating along the

magnetic field. The waveforms, however, are different from those of ESW in the PSBL region. As shown in Figures 2.6 and 2.7, the waveform of ESW in the auroral region have mono-hump or mono-well structure with a large amplitude in the $E_\perp$ component, indicating that this ESW has two-dimensional structure. The ESW potentials in the auroral region have isolated two-dimensional structure, which are not only solitary in the parallel direction but also isolated in the direction perpendicular to the ambient magnetic field as schematically illustrated in Figure 2.8(b). The scale length of these waves in the perpendicular direction is reported as the order of local ion gyroradius by the observations of the FAST satellite.

Since November 1994, Geotail was put on the near tail orbits and we have many opportunities to observe the PSBL in the near tail region. According to the recent observations of the Geotail spacecraft, ESW with two-dimensional structures are found in the near tail PSBL [*Kojima*, 1998]. The natures of these two-dimensional ESW are very similar to those of ESW in the auroral region, except for the amplitudes of their electric fields. From the statistical analyses, *Kojima* [1998] concluded that the observation possibilities of the PSBL ESW with two-dimensional structures are much higher in the near tail region $|X_{\rm GSE}| < 100R_E$ than in the distant tail region. This tendency is very important for investigating the generation mechanism and generation source region of ESW in the PSBL.

Chapter 3

Linear and Nonlinear Theories of Electron Beam Instabilities

In the previous chapter, we explained the ESW potential model assumed from Geotail observations. This ESW potential model is that impulsive waveforms of ESW correspond to sequences of spatially isolated potentials traveling along the ambient magnetic field. These potentials can be explained by BGK potentials which are excited by electron beams drifting along the ambient magnetic field. In this chapter, we assume ESW generation model based on linear and nonlinear theories and previous simulation studies, and specify possible electron beam instabilities for ESW generation.

3.1 Electron velocity distribution functions

As stated in Section 2.1, ESW are considered to be related to purely electrostatic instabilities along the magnetic field, and these instabilities are excited by electron beams traveling along the ambient magnetic field. In addition, previous one-dimensional simulation studies by particle code [*e.g.*, *Morse et al.*, 1969] or Vlasov code [*e.g.*, *Berk and Roberts*, 1967; *Berk et al.*, 1970] demonstrated that some kinds of electron beam instabilities excite isolated potentials along the magnetic field. According to these observation and simulation studies, we assumed that isolated potentials of ESW are generated by some kinds of electron beam instabilities along the ambient magnetic field.

During over seven years' observations of the Geotail spacecraft, ESW have almost always been observed when the Geotail spacecraft is traveling in the PSBL region. This suggests that ESW exist almost everywhere in the PSBL region. As mentioned in Section 2.1, since ESW are not locally excited but propagating along the ambient magnetic field, we consider that ESW in the PSBL region can exist very stably, and electrostatic potentials corresponding to ESW are also very stable. Such stable electrostatic potentials are assumed to be Bernstein-Greene-Kruskal (BGK) potentials [*Bernstein et al.*, 1957].

Electron two-stream instability is one of electron beam instabilities along the ambient magnetic field, driven by two counter streaming electron beams. Assuming these two electron groups as beam and background electrons, beam electrons are drifting against background electrons with drift velocity $v_{\rm d}$. To make a problem simple, we assume only one-dimensional motion (only move in x direction) and cold plasma ($T_{\rm e1} = T_{\rm e2} = 0$), the electron dielectric function $\varepsilon(k, \omega)$ is given as

$$\varepsilon(k,\omega) = 1 - \frac{\Pi_{\rm e1}^2}{(\omega - kv_{\rm d}/2)^2} - \frac{\Pi_{\rm e2}^2}{(\omega + kv_{\rm d}/2)^2} \tag{3.1}$$

where Π_{e1} and Π_{e2} are electron plasma frequencies of beam and background electrons, respectively. When this equation has solutions with a positive imaginary part, waves corresponding to those solutions become unstable. This is so-called "electron two-stream instability".

We consider certain kinds of these two-stream instabilities are possible generation mechanisms of ESW, then we treat some variations of these two-stream instabilities as initial electron distribution functions. We assumed three typical electron beam instabilities, "two-stream instability","weak beam instability" and "bump-on-tail instability". The electron velocity distribution functions of these three types of instabilities are shown in Figure 3.1.

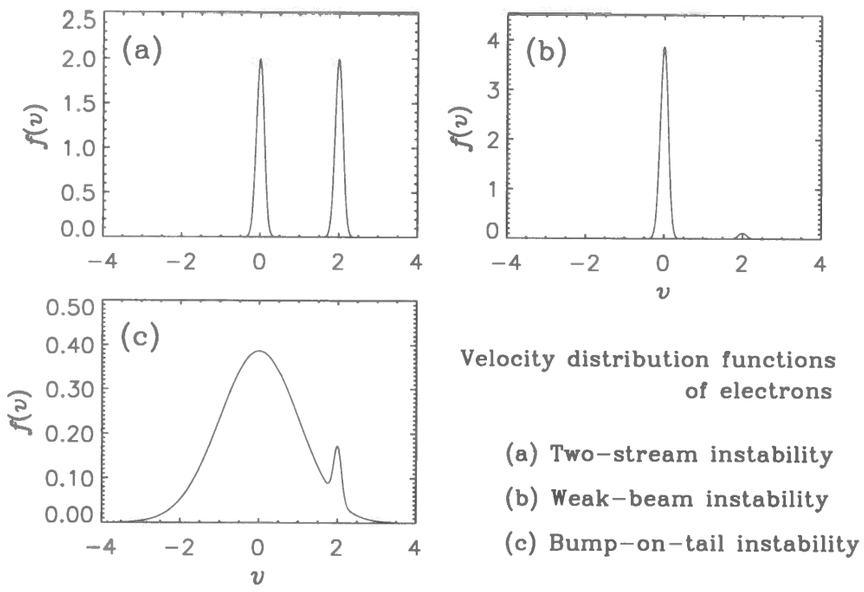

Figure 3.1: Initial electron velocity distribution functions of three types of electron beam instabilities, (a):two-stream instability, (b):weak-beam instability and (c):bump-on-tail instability.

All the electron beam instabilities studied in this thesis are driven by two counter streaming electron beams, an electron beam and background electrons, so-called "two-stream instability". However, we use this term "two-stream instability" as the most typical case of such electron beam instabilities [as shown in Figure 3.1(a)], where two electron beams have equal densities ($n_1 = n_2$) and equal temperatures ($T_{e1} = T_{e2}$), where n_1 and n_2 are densities of beam and background electrons, and T_{e1} and T_{e2} are temperatures of beam and background electrons, respectively. First of all, we assumed this simple two-stream instability formed by two electron beams with the same densities as a possible instability to form ESW. Especially in the auroral region, very strong electron beams are observed, therefore, this assumption is feasible in space plasma. Next, we studied another typical electron beam instability excited by a very weak electron beam, the weak-beam instability [Figure 3.1(b)], and estimated dependence of ESW formation on electron beam densities. These two types of electron beam instabilities

are formed by both very cold electron components, beam and background electrons. In the Earth's magnetotail region, however, ESW are frequently observed in the PSBL region, where the background electrons are always thermalized, as shown in Figure 2.4(g). In addition, strong electron beams as we assumed for the two-stream instability are scarcely observed in this region. Therefore, we assumed another electron beam instability formed by a weak electron beam and a hot background electrons as a possible instability to generate ESW in the PSBL region, This is the bump-on-tail instability, as shown in Figure 3.1(c).

In the two-stream instability, the electron beam density ratio R $(= n_1/(n_1 + n_2))$ is given as $R = 0.5$, while in the weak-beam and the bump-on-tail instability, $R = 0.03$. The weak-beam instability and the bump-on-tail instability are excited by a electron beam with very small density. The difference between the weak-beam and the bump-on-tail instabilities is the temperature of background electrons. Both beam and background electrons are assumed to be cold in the two-stream and the weak-beam instability. While in the bump-on-tail instability, beam electrons are cold but background electrons are hot.

In the present simulations, we assume a relatively cold electron beam as the initial condition. Unfortunately, such cold electron beams cannot be observed because the particle detector has insufficient time resolution in comparison with the diffusion time of electron beams in the electron beam instabilities. What we can observe in the particle measurement are the diffused electron fluxes resulting from the instabilities [*Omura et al.*, 1999a], as shown in Figure 2.4(g) presented in Section 2.1.

3.2 Linear dispersion analysis of electron beam instabilities

Before performing computer simulations, we calculated linear dispersion relations of waves excited from electron beam instabilities studied in the present study. To calculate linear dispersion relations, we use the dispersion solver (KUPDAP: Kyoto University Plasma Dispersion Analysis Package)[*Ueki*, 1987], which have been developed at RASC (Radio Atmospheric Science Center) in Kyoto University. In this analysis, the initial velocity distribution functions of electrons are assumed as those of "two-stream instability", "weak-beam instability" and "bump-on-tail instability". As mentioned in the previous section, these instabilities are considered as source instabilities of ESW generation. In each case, we calculated linear dispersion relations of waves in various propagation angles to the static magnetic field for two different magnitudes of the magnetic fields. The magnitudes of the static magnetic fields have no effect in the one-dimensional simulation system along the magnetic field, and oblique mode waves also cannot exist in such one-dimensional systems. In the two-dimensional simulations, on the other hand, oblique mode waves are excited and suspected to affect the spatial structures of ESW and their formation process. The growth rates of oblique mode waves are considered to be affected by the magnitude of the static magnetic field and the propagation direction to the magnetic field. We estimated dependence of linear growth rates on the propagation directions and the magnitudes of the static magnetic fields. These parametric dependence of linear growth rates can be used to distinguish linear and nonlinear effects in the formation process of ESW.

In this simulation study, magnitudes of the static magnetic fields are defined by ratio of an electron cyclotron frequency and an electron plasma frequency (Ω_e/Π_e). In the PSBL region,

magnitudes of the magnetic fields are relatively small such as $\Omega_e/\Pi_e \sim 0.2$. In the auroral region, on the other hand, magnitudes of the magnetic fields are very strong in comparison with those in the PSBL region, and they depend on the altitudes. We assume the strong and the weak magnetic fields as $\Omega_e/\Pi_e \sim 1.0$ and $\Omega_e/\Pi_e \sim 0.2$ in this study. We examined a linear analysis and performed simulation studies for these strong and weak magnetic fields. In the linear dispersion analysis, propagation angles of waves are taken as 0, 15, 30, 45 degrees to the ambient magnetic field. All the constant plasma parameters used in this analysis are listed in Table 3.1. In this table, R, Ω_e, v_d, v_{t1} and v_{t2} represent the electron beam density, the electron

Run	R	Ω_e	v_d	v_{t1}	v_{t2}
(a)-1	0.50	1.0	2.0	0.1	0.1
(a)-2	0.50	0.2	2.0	0.1	0.1
(b)-1	0.03	1.0	2.0	0.1	0.1
(b)-2	0.03	0.2	2.0	0.1	0.1
(c)-1	0.03	1.0	2.0	0.1	1.0
(c)-2	0.03	0.2	2.0	0.1	1.0

Table 3.1: Plasma parameters in the linear analysis of electron beam instabilities, (a):two-stream instability, (b):weak-beam instability and (c):bump-on-tail instability.

cyclotron frequency, the drift velocity of the electron beam, the thermal velocity of the beam electrons and the thermal velocity of the background electrons, respectively. These parameters are the same with those in simulation studies examined in the following chapters.

3.2.1 Linear dispersions of electron beam instabilities

Figures 3.2, 3.3 and 3.4 present dispersion relations of three types of electron beam instabilities, (a):the two-stream instability, (b):the weak-beam instability and (c):the bump-on-tail instability, respectively. In these figures, we displayed dispersion relations of only unstable waves with positive growth rates in these instabilities. In each figure, the left and the right columns show the cases with a strong magnetic field ($\Omega_e = \Pi_e$) and a weak magnetic field ($\Omega_e = \Pi_e \times 0.2$), and the upper and the lower panels show the real and the imaginary parts of the ω-k diagrams, respectively. In all these figures, the y axis, presenting frequencies, is normalized to the plasma oscillation frequency of electrons which is constant in all the simulation runs as $\Pi_e = 1.0$, and the x axis, presenting wave numbers, is normalized to the Debye length of the background electrons in the bump-on-tail instability [Runs (c)-1,2] ($\lambda_D = v_{t2}/\Pi_e$). The line styles correspond to the propagation directions of waves to the static magnetic field as shown in each figure.

Two-stream instability Figure 3.2 presents the linear dispersion relations of the two-stream instability with two different magnitudes of the static magnetic fields. In the upper panels, presenting the real frequencies of the ω-k diagrams, we can find strong unstable waves. According to the linear theory, the two-stream instability excites Langmuir waves. In this results of the linear dispersion analysis of the two-stream instability, however, we cannot find no Langmuir waves. This is because the two-stream instability studied in the present study is excited by

cold electron beams, and it is too strong to treat by usual linear theories in which only very weak linear waves are assumed, a priori. Therefore, not Langmuir waves but strong beam-mode waves are excited in Figure 3.2. These beam-mode waves are drifting with the electron beam, and the gradient of the parallel propagating wave in the ω-k diagram, which indicates the phase velocity of these beam-mode waves, corresponds to the drift velocity of the electron beam. In this two-stream instabilities, since the most unstable waves with the largest growth rate are excited due to the interaction of two counter streaming electron beams, these beam-mode waves are excited almost in the middle of the two electron beams, and the phase velocity of this wave becomes almost equal to a half of the drift velocity of the electron beam ($v_d/2 \simeq 1.0$). In both cases with a strong and a weak magnetic fields, the most unstable waves with the maximum growth rates are those propagating in the direction parallel to the static magnetic field. In addition, the maximum growth rates themselves are almost same, $\gamma \simeq 0.36 \times \Pi_e$, and they are also found at the same point where $k\lambda_D \simeq 0.6$. There is no significant difference due to the magnitudes of the static magnetic fields on the most unstable waves with the maximum growth rates.

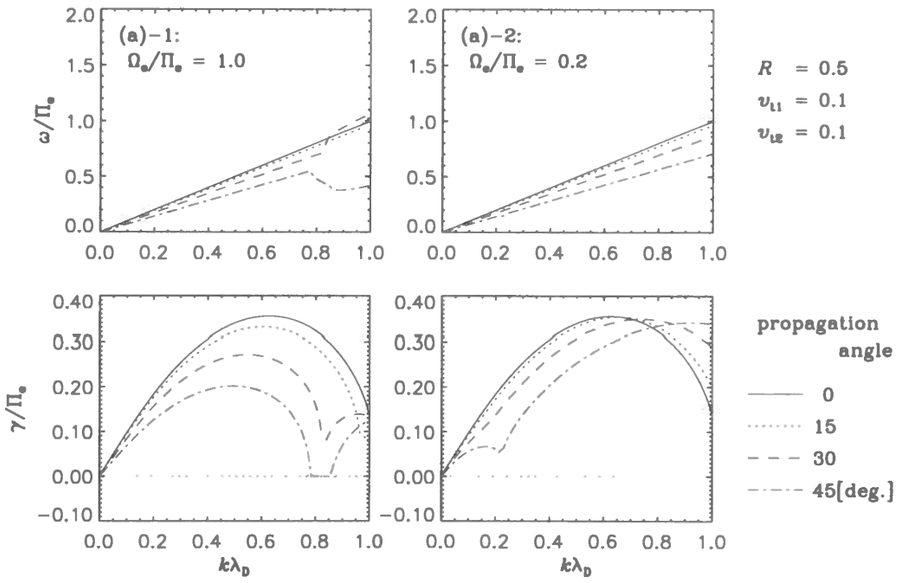

Figure 3.2: Linear dispersion relations of the electron two-stream instabilities with a strong and a weak magnetic fields. The left and right panels show the ω-k diagram of Runs (a)-1 and (a)-2 listed in Table 3.1, respectively.

The growth rates of the oblique mode waves, on the other hand, have obvious dependence on the magnitudes of the static magnetic fields. In the left column, presenting the case with a strong magnetic field [Run (a)-1], the growth rates of the oblique mode waves are smaller and limited in smaller k range in comparison with that of the parallel propagating wave with the maximum growth rate. In the right column, presenting the case with a weak magnetic field

[Run (a)-2], on the other hand, even the oblique mode waves have larger growth rates almost equal to the maximum growth rate of the parallel propagating wave. This indicates that in the electron two-stream instability with a weak magnetic field, the oblique mode waves are strongly excited and wave lengths in the direction perpendicular to the ambient magnetic field are smaller than those in the two-stream instability with a strong magnetic field.

Weak-beam instability Figure 3.3 presents the linear dispersion relations of the electron weak-beam instability with two different magnitudes of the static magnetic fields. As the same with the electron two-stream instability, we can find strong beam-mode waves in the real frequency part of the ω-k diagrams, presented in the upper panels of this figure. The gradient of the parallel propagating wave in the ω-k diagram, indicating the phase velocity of this wave, is about 1.5. This phase velocity is larger than that in the two-stream instability. Though the most unstable wave in the weak-beam instability is excited due to the interaction of the weak electron beam and the background electrons, this beam-mode wave is excited in the weak electron beam, therefore, the phase velocity of this wave becomes close to the drift velocity of the electron beam.

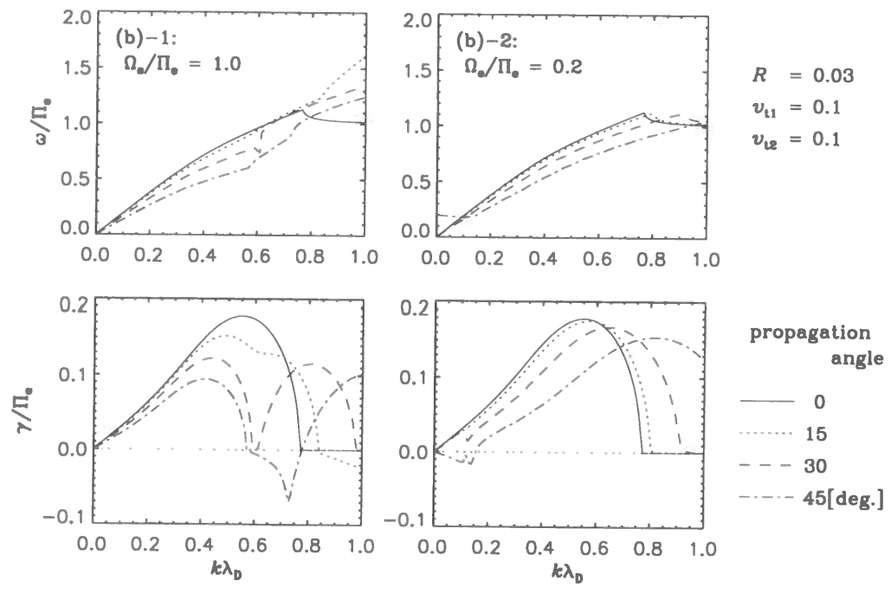

Figure 3.3: Linear dispersion relations of the weak-beam instability with a strong and a weak magnetic fields. The left and right panels show the ω-k diagram of Runs (b)-1 and (b)-2 listed in Table 3.1, respectively.

In the electron weak-beam instability, the most unstable waves with the maximum growth rates are those propagating in the parallel direction to the static magnetic field in both cases with a strong and a weak magnetic fields. The maximum growth rates are almost same in both cases and they are also found at the same point where $k\lambda_D \simeq 0.6$. We cannot find any effects

of the magnitudes of the static magnetic fields on characteristics of the most unstable waves. These results are almost the same with the previous case of the two-stream instability. On the other hand, since the weak-beam instability is weaker instability in comparison with the two-stream instability, the maximum growth rates ($\gamma \simeq 0.18 \times \Pi_e$) in the weak-beam instabilities are smaller than those in the two-stream instabilities.

The growth rates of the oblique mode waves also have dependence on the magnitudes of the static magnetic fields in the weak-beam instability. They show almost the same characteristics with those in the two-stream instability. In the left column, presenting the case with a strong magnetic field [Run (b)-1], the growth rates of the oblique mode waves are smaller and limited in smaller k range. While in the right column, presenting the case with a weak magnetic field [Run (b)-2], though the growth rates of the oblique mode waves are a little smaller than that of the parallel propagating wave with the maximum growth rate, they have still large values and spread in wide k range. As the same with the two-stream instability, this also indicates that the oblique mode waves are strongly excited and wave lengths in the direction perpendicular to the ambient magnetic field are smaller in the weak-beam instability with a weak magnetic field in comparison with those with a strong magnetic field.

Bump-on-tail instability Figure 3.4 presents the linear dispersion relations of the electron bump-on-tail instability with two different magnitudes of the static magnetic fields. Though the bump-on-tail instability is a relatively weak instability, we cannot find linear Langmuir waves but beam-mode waves in the upper panels of this figure, presenting the real frequency part of the ω-k diagrams, which is the same with the previous two instabilities. The gradient of the parallel propagating wave in the ω-k diagram, indicating the phase velocity of this wave, is about 1.7. This phase velocity is larger than that in the weak-beam instability. This can be explained as follows. In the bump-on-tail instabilities, the background electrons are hot and the electron beam is on the high-energy tail of the background electrons. The electron beam interact with only this high-energy tail of the background electrons, then the unstable waves are excited in the electron beam. The phase velocity of this beam-mode wave, therefore, is almost same with the drift velocity of the electron beam.

As the same with the previous two electron beam instabilities, the most unstable waves with the maximum growth rates are those propagating in the direction parallel to the static magnetic field in both cases with a strong and a weak magnetic fields in the bump-on-tail instability. The maximum growth rates are almost same in both cases ($\gamma \simeq 0.07 \times \Pi_e$), and they are also found at the same point where $k\lambda_D \simeq 0.5$. This growth rates are very small in comparison with the previous two electron beam instabilities.

The growth rates of the oblique mode waves have only a little dependence on the magnitudes of the static magnetic fields in this bump-on-tail instability. This dependence, however, is not so critically, and it's characteristics is different from those in the previous two instabilities. In both cases with a strong and a weak magnetic fields, the growth rates of the oblique mode waves are smaller than that of the parallel propagating wave. In the previous two instabilities, the growth rates of the oblique mode waves are larger in the case with a weak magnetic fields in comparison with those in the case with a strong magnetic fields. While in this bump-on-tail instability, the growth rates of the oblique mode waves are smaller in the case with a weak magnetic field [Run (c)-2] than those in the case with a strong magnetic field [Run (c)-1]. This indicates that the oblique mode waves are not excited strongly in the bump-on-tail instability

with a weak magnetic field. In the bump-on-tail instability, however, the difference in the growth rates of the oblique mode waves are small, and these is no significant dependency on the magnitudes of the static magnetic fields.

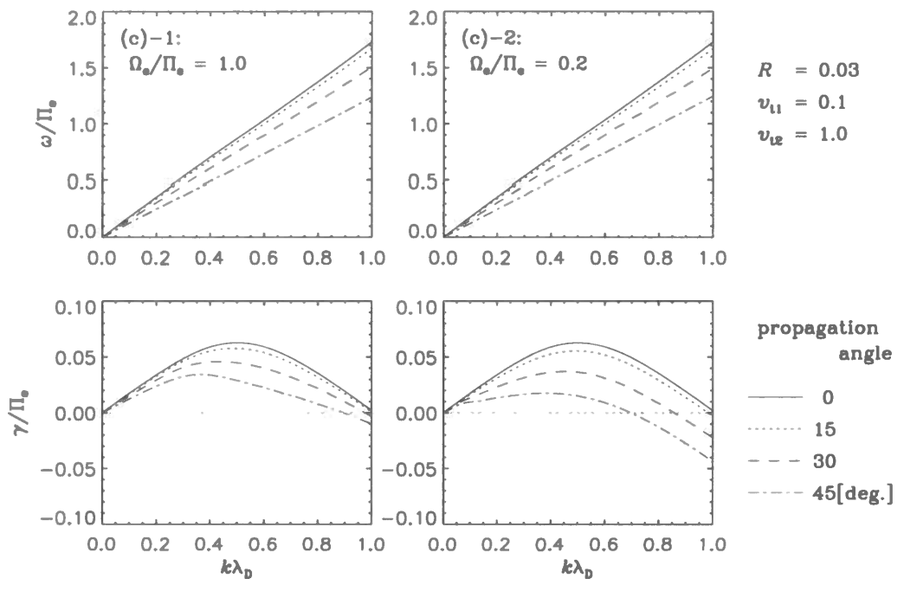

Figure 3.4: Linear dispersion relations of the bump-on-tail instability with a strong and a weak magnetic fields. The left and right panels show the ω-k diagram of Runs (c)-1 and (c)-2 listed in Table 3.1, respectively.

3.2.2 Parametric dependence of linear dispersions

All of the electron beam instabilities analyzed in the present study, the two-stream instability, the weak-beam instability and the bump-on-tail instability, have their maximum growth rates at the waves whose propagation angles are in the direction parallel to the static magnetic field. Their maximum growth rates are almost same in both cases with a strong and a weak magnetic field in all these instabilities. In other words, the maximum growth rates of these electron beam instabilities are independent of the magnitudes of the static magnetic fields. Among these three types of electron beam instabilities, the two-stream instability has the largest growth rate, while the bump-on-tail instability has the smallest growth rate.

There are differences due to the magnitudes of the static magnetic fields especially on the growth rates of the oblique mode waves. In the two-stream instability and the weak-beam instability, the oblique mode waves are excited more strongly in the weak magnetic field than those excited in the strong magnetic field. The growth rates of these oblique mode waves in the weak magnetic field is very large, which are almost equal to the maximum growth rate of the parallel propagating wave. While the growth rates of the oblique mode waves are small

and limited in small k range in the strong magnetic field. In the bump-on-tail instability, on the other hand, the difference due to the magnitudes of the static magnetic fields in the growth rates of the oblique mode waves are small, and their effects are different from those in the other two instabilities as presented in the previous section.

According to the satellite observations, as presented in Chapter 2, the amplitudes of ESWs' electric fields in the PSBL region are very small, suggesting that ESW are generated by weak electron beam instabilities. In terms of the strength of instabilities, the bump-on-tail instability is the most possible instability to generate ESW in this region among these three types of electron beam instabilities. The magnitudes of the ambient magnetic fields are relatively small in the PSBL region, and spatial structures of ESW in this region is estimated to be one-dimensional. This is consistent with the results of the linear dispersion analysis of the bump-on-tail instability with a weak magnetic field. According to the linear analysis, oblique mode waves are not excited so strongly in the bump-on-tail instability with a weak magnetic fields, which suggests that ESW generated by the bump-on-tail instability tend to have one-dimensional structures rather than two-dimensional ones. On the other hand, the amplitudes of ESWs' electric fields are very large in the auroral region, suggesting that ESW are generated by very strong electron beam instability. We expect that the two-stream instability is the most possible instability to generate ESW in this region. In addition, the magnitudes of the ambient magnetic fields are very strong in the auroral region, and spatial structures of ESW in this region is reported to be two-dimensional. This is not consistent with the linear dispersion analysis of the two-stream instability with a strong magnetic fields. In the two-stream instability with a strong magnetic field, oblique mode waves are not excited so strongly in comparison with those with a weak magnetic field.

The linear dispersion theory tells that unstable Langmuir waves are excited by electron beam instability of two counter streaming electron beams. In the dispersion relations of the three types of electron beam instabilities analyzed in the present study, however, we can find no Langmuir waves are excited but the beam-mode waves are excited. This is because even the bump-on-tail instability formed by a 3% electron beam, which is the weakest instability of these three instabilities, is still strong instability, and we cannot treat these instabilities by the usual linear dispersion theories. We examined to calculate dispersion relations of much weaker bump-on-tail instabilities, which are formed by weak electron beams with much smaller densities.

In Figure 3.5, linear dispersion relations of very weak bump-on-tail instabilities are presented. The left column shows the linear dispersion relations of the bump-on-tail instability of a 0.05% density electron beam, and the right column shows those of the bump-on-tail instability of a 0.01% density electron beam. In this figure, the solid and the dashed lines show dispersions of the Langmuir waves in the background electrons and those of the beam electrons, respectively. In the right column, presenting the bump-on-tail instability of a 0.01% electron beam, we can find coupling of the Langmuir wave and the beam electrons. This linear Langmuir wave has a positive linear growth rate. Beam-mode waves with positive growth rates are not found in this dispersion relation. In the left column, presenting the bump-on-tail instability of a 0.05% electron beam, on the other hand, though we can also find coupling of the Langmuir wave and the beam electrons, this linear Langmuir wave has only a negative growth rate. In this figure, we have another line (the dash-dotted line) with positive growth rates. This line presents the dispersion relation of the beam-mode wave with positive growth rates.

This result indicates that all the electron beam instabilities investigated in this simulation study are too strong to treat with the linear dispersion theories. Even the bump-on-tail instability of a 0.05% electron beam is still too strong and excite beam-mode waves not linear Langmuir waves. We confirmed the linear Langmuir wave with a positive growth rates excited in the very weak bump-on-tail instability which is formed by a very weak electron beam of only a 0.01% density ratio, as shown in the right column of Figure 3.5.

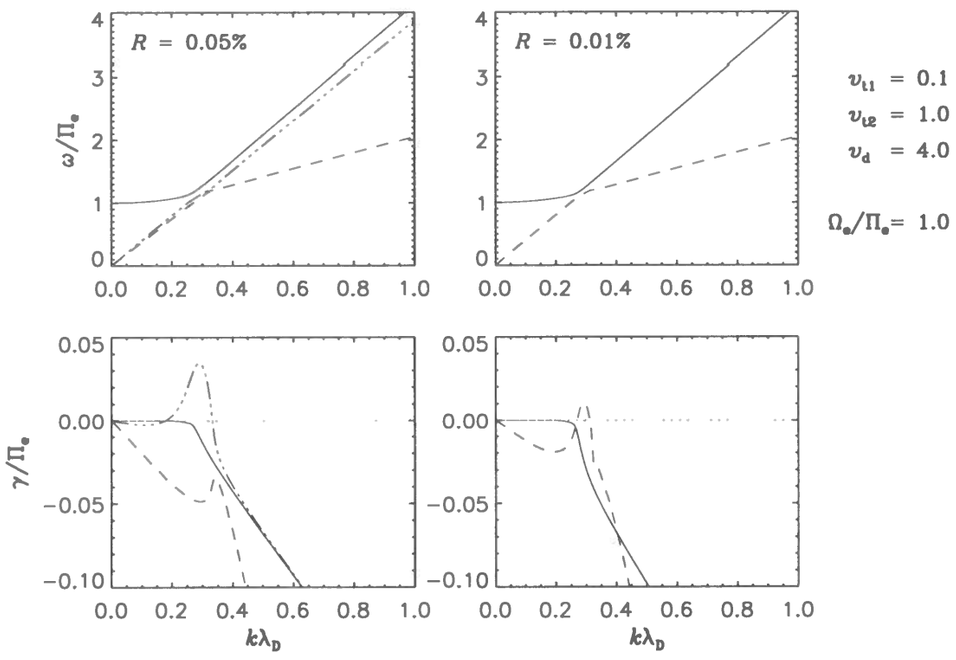

Figure 3.5: Linear dispersion relations of the very weak bump-on-tail instabilities. We can find the linear Langmuir wave with a positive growth rate in the right column. While in the left column, the beam-mode wave has a positive growth rate and that of the Langmuir wave is negative.

3.3 BGK equilibrium

As mentioned in the previous section, ESW potentials are isolated electrostatic potentials, and they are stable under the plasma conditions, for example, in the PSBL. Such electrostatic potentials are assumed to be Bernstein-Greene-Kruskal (BGK) potentials [*Bernstein et al.*, 1957]. BGK potential is an electrostatic potential formed by BGK mode waves, which are stationary waves independent of time. BGK mode waves are solved as stationary solutions of one-dimensional Vlasov equation and Poisson's equation [*Bernstein et al.*, 1958].

One-dimensional Vlasov equation for stationary solutions ($\frac{\partial f}{\partial t} = 0$) is given as

$$v\frac{\partial f_s}{\partial x} - \frac{q_s}{m_s}\frac{\mathrm{d}\phi}{\mathrm{d}v}\frac{\partial f_s}{\partial v} = 0 \tag{3.2}$$

where the subscript s represents the s-th species of particles, and f_s, q_s and m_s are a distribution function in time, space and velocity space, a charge and a mass of the s-th species, respectively. ϕ represents an electrostatic potential in the one-dimensional system. One-dimensional Poisson's equation of one electron and one ion (proton) components is written as

$$\frac{\partial^2\phi}{\partial x^2} = \frac{\mathrm{e}}{\epsilon_0}\left[\int_{-\infty}^{\infty}\mathrm{d}v f_\mathrm{e} - \int_{-\infty}^{\infty}\mathrm{d}v f_\mathrm{i}\right] \tag{3.3}$$

where f_e and f_i represent the distribution functions of electron and ion (proton) components, and e and ϵ_0 represent the electron charge and the electric permittivity, respectively. BGK mode waves satisfy these two equations. These stationary solutions make potential structures called "BGK potentials", as schematically illustrated in Figure 3.6 [*Nicholson*, 1983]. Therefore, BGK potentials are electrostatic potentials, independent of time, and they can exist stably for a long time. Since BGK mode wave is a solution of one-dimensional Vlasov and Poisson's equations, BGK potentials are one-dimensional potentials.

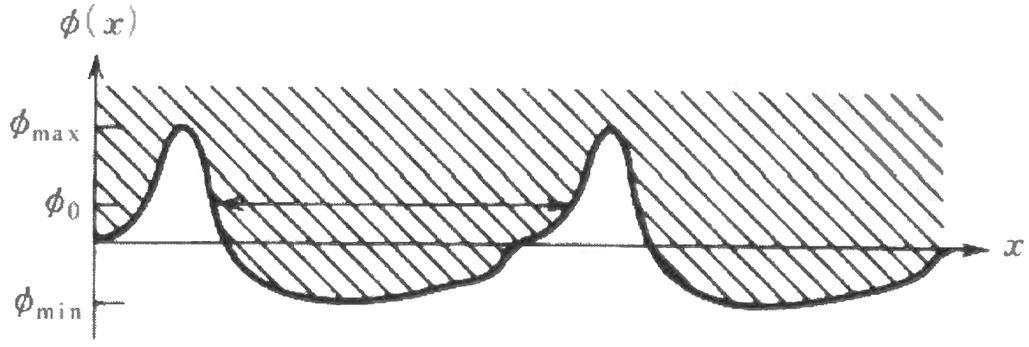

Figure 3.6: Periodic potentials of a BGK mode that contains trapped and untrapped particles [*after Nicholson*, 1983].

According to the previous simulation studies, two counter streaming electrons give rise to the two-stream instability and excite unstable waves. As the time goes on, these waves grow and electrostatic potentials are excited. At the time when energies of waves become comparable to kinetic energies of particles, particles are trapped in these potentials, and waves and particles interact with each other. This interaction transfer energies of waves into those of particles. As a result, growth of unstable waves saturate. This wave-particle interaction modifies velocity distribution of particles, then it manages to keep the present state for a long time. One of these stationary states is BGK mode, and electrostatic potentials formed in this process are BGK potentials. BGK potentials are stable due to this wave-particle interaction.

3.4 Nonlinear trapping theory

In this section, we assumed ESW generation model by electron beam instabilities. We assumed that ESW potentials are BGK potentials which are excited by electron beam instabilities. These BGK potentials are very stable on the balance of stationary electrostatic potentials and trapped and untrapped electrons. Many theoretical works on such nonlinear trapping of particles by coherent electrostatic and electromagnetic waves are examined [*e.g.*, *Karpman et al.*, 1975; *Matsumoto*, 1985].

Assuming a large-amplitude monochromatic electrostatic wave traveling along x axis, pendulum equations of resonant particles in a longitudinal electric field are written as follows:

$$\frac{\mathrm{d}^2\zeta}{\mathrm{d}t^2} + \omega_\mathrm{T}^2 \sin\zeta = 0 \tag{3.4}$$

where $\zeta = kx$ is a phase angle presenting a relative location of the particle in one wavelength, and ω_T is the trapping frequency defined by

$$\omega_\mathrm{T} = \sqrt{\frac{kqE_\mathrm{A}}{m}} \tag{3.5}$$

where E_A, k are the amplitude of the wave and wavenumber, q and m present a mass and a charge of a test particle, respectively. The trapping frequency ω_T physically determines the bounce period of particles trapped in the vicinity of the bottom of the wave potential $\phi(x)$ ($= -\frac{E_\mathrm{A}}{k}\cos\zeta$). By eliminating t, an equation of energy conservation is obtained, which is a form of

$$\frac{1}{2}mv^2 + q\phi(x) = W_0 \tag{3.6}$$

where W_0 is an integration constant which represents a total energy of the particle. This total energy W_0 determines the orbit of the particle in phase space. The phase space orbits for various values of W_0 are illustrated in Figure 3.7 [*Matsumoto*, 1985]. The orbits within the shaded area have a form of the closed loops representing a bounce motion of the trapped particles in the electrostatic wave potential well. The shaded area is often called "trapping region" in the phase space. The separatrix of "trapping" and "untrapping" region is expressed by

$$\frac{1}{2}mv^2 + q\phi(x) = \frac{qE_\mathrm{A}}{k} \tag{3.7}$$

Therefore the speed of the trapped particles is limited by a maximum velocity which is achieved at $\zeta = 2n\pi$ (n: integer) on the separatrix. This maximum velocity is called "trapping velocity" V_T which is expressed as

$$V_\mathrm{T} = \frac{2\omega_\mathrm{T}}{k} \tag{3.8}$$

and the separatrix is expressed in terms of V_T as

$$v^2 = V_\mathrm{T}^2 \cos^2(\zeta/2) \tag{3.9}$$

This equation of the separatrix indicates that those particles with an initial velocity v_0 and an initial phase angle ζ_0 which satisfy

$$v^2 \geq V_\mathrm{T}^2 \cos^2(\zeta_0/2) \tag{3.10}$$

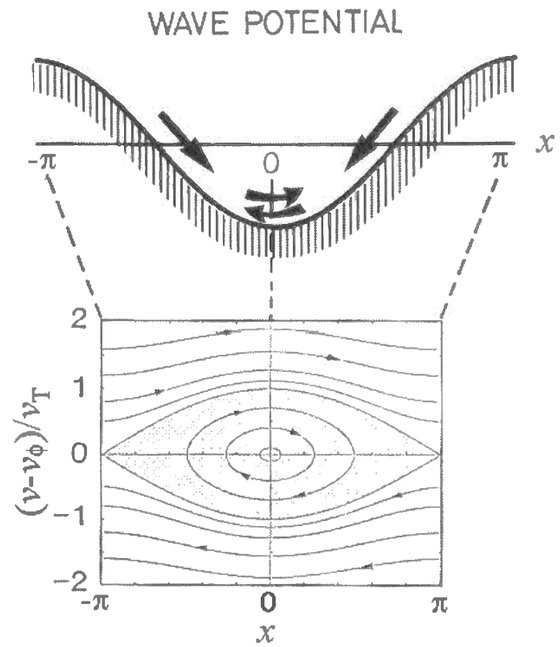

Figure 3.7: Concept of particle trapping in an electrostatic potential [*after Matsumoto*, 1985].

are not trapped by the electrostatic wave potential and travel over this potential well. BGK potential is one of stationary solutions of such electrostatic potentials formed by and balanced with trapped and untrapped particles.

The nonlinear evolution of this wave-particle interaction gives rise to particle trapping by the wave potential and phase mixing in the phase space and associated deformation of velocity distribution function, as schematically illustrated in Figure 3.8 [*Kadomtsev*, 1976]. As shown in this figure, phase mixing occurred within the separatrix in the phase space, form a plateau in the velocity distribution function.

Since the electron beam instabilities studied in this thesis are strong as analyzed in Section 3.2, electrostatic potentials which are excited by these instabilities are thought to grow to large-amplitude enough to trap electrons therein, and the deformation of the velocity distribution function due to phase mixing of trapped particles occurs. In these instabilities, this deformation of the velocity distribution function diminish positive gradients in the velocity distribution functions, stopping the growth of the electron beam instabilities. Due to this saturation process, stable BGK potentials, corresponding to ESW, are formed through nonlinear evolutions of electron beam instabilities.

A theoretical work on the nonlinear trapping of electrons in solitary BGK potentials is performed by *Krasovsky et al.* [1997]. They further investigate theoretically interaction of two BGK potentials, explaining the general tendency to coalescence of BGK potentials [*Krasovsky et al.*, 1999].

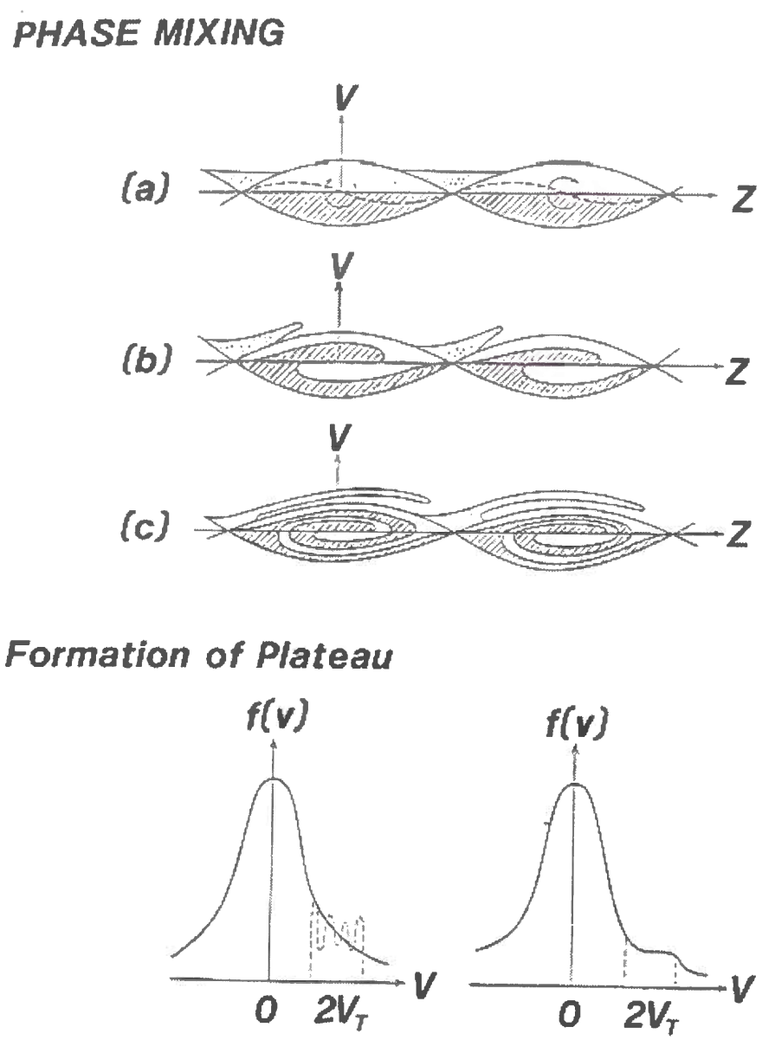

Figure 3.8: Schematic illustration of phase mixing and associated formation of plateau in velocity distribution function [*after Kadomtsev*, 1976].

Chapter 4

Electrostatic Particle Code and Simulation Model for ESW

4.1 Two-dimensional electrostatic particle code

4.1.1 Basic equations

In the present study, since we treat only electrostatic wave-particle interactions in space plasma, basic equations are the equations of motion with no collision terms and Poisson's equation. Assuming a non-relativistic effect, the equations of a particle motion are given by

$$\frac{\mathrm{d}\boldsymbol{r}_s}{\mathrm{d}t} = \boldsymbol{v}_s \tag{4.1}$$

$$\frac{\mathrm{d}\boldsymbol{v}_s}{\mathrm{d}t} = \frac{q_s}{m_s}(\boldsymbol{E} + \boldsymbol{v}_s \times \boldsymbol{B}) \tag{4.2}$$

where the subscript s represents the s-th species of particles and $\boldsymbol{v}_s$, $\boldsymbol{r}_s$, q_s and m_s represent a velocity, a particle position, a charge and a mass of the s-th species, and $\boldsymbol{E}$ and $\boldsymbol{B}$ represent the electric and the magnetic field, respectively. Poisson's equation in the MKSA unit is

$$\nabla \cdot \boldsymbol{E} = \frac{\rho}{\epsilon_0} \tag{4.3}$$

where ϵ_0 represents the electric permittivity, and the quantities ρ represents the charge density. These basic equations are simultaneously solved in a self consistent manner in computer simulations performed in the present study.

4.1.2 Two-dimensional electrostatic particle code (kuES2)

We have a simulation code, called KEMPO (Kyoto university ElectroMagnetic Particle cOde) [*Matsumoto and Omura*, 1984; *Omura*, 1985; *Omura and Matsumoto*, 1993] to investigate nonlinear phenomena in space plasma. This KEMPO code has been developed at RASC in Kyoto University, and we have dedicated much efforts to revise this code for more than two decades. In conjunction with the rapid progress in computer in terms of its speed and working area of memory, KEMPO has become a very powerful and useful tool in investigating nonlinear plasma phenomena in space.

Two-dimensional computer simulations performed in this study, however, still need numerous computer resources, especially working area of memory and CPU time. In addition, we treat only electrostatic wave-particle interactions in the present study. To save computer resources, we developed a new two-dimensional electrostatic particle code named kuES2 (kyoto

university Electro Static 2-dimensional particle code). This simulation code is improved from KEMPO to optimize in investigating electrostatic phenomena in space plasma by one- and two-dimensional particle simulations. In kuES2, we calculate only Poisson's equation in stead of full Maxwell equations to decrease calculation time, and we also decrease necessary memory area for performing simulations. By using this simulation code, we can make quantitative analysis on various electrostatic phenomena in space plasma, especially electrostatic wave-particle interactions.

In kuES2, the position of particles have two-dimensional space, x and y, and the velocity have three-dimensional space, v_x, v_y and v_z. Basic equations stated in the previous subsection are solved with the finite-difference scheme. Non-relativistic equations of motion and Poisson's equation in the difference scheme can be written as follows:

$$\frac{\mathrm{d}\boldsymbol{r}_s(t+\Delta t) - \mathrm{d}\boldsymbol{r}_s(t)}{\Delta t} = \boldsymbol{v}_s \tag{4.4}$$

$$\frac{\mathrm{d}\boldsymbol{v}_s(t+\Delta t) - \mathrm{d}\boldsymbol{v}_s(t)}{\Delta t} = \frac{q_s}{m_s}(\boldsymbol{E} + \boldsymbol{v}_s \times \boldsymbol{B}) \tag{4.5}$$

$$\frac{\mathrm{d}\boldsymbol{E}(x+\Delta r) - \mathrm{d}\boldsymbol{E}(x)}{\Delta r} = \frac{\rho}{\epsilon_0} \tag{4.6}$$

In particle simulations, however, it is impossible to treat a realistic enormous number of plasma particles because of the memory and the CPU time limit of computers. Thus, so-called "superparticle model" is adopted in particle codes. In this superparticle model, a particle is treated as a superparticle with a large charge and a large mass which represents many real particles, retaining the particle nature of plasma. The charge density (ρ) is calculated by using the PIC (Particle-In-Cell) method which distributes the charge of particles to the adjacent grid points (four grid points in the two-dimensional simulation) with an area weighting method.

Normalization by relative system of units is adopted in kuES2, because it is not efficient to treat a physical quantity as it is. Since this code is improved to study mainly stability and equilibrium of plasma phenomena in space, boundary condition is taken to be periodic in kuES2. Of course, we will change the boundary condition of this simulation code, and study effects of the boundary condition by performing computer simulations with other boundary conditions, for example, the free boundary condition.

4.1.3 Parallel coding for particle code

Owing to the recent progress of computer hardwares, we come to be able to perform simulation runs using a lot of computer resources, CPU time and memory space. Making use of the recent computers with multiple processors, we parallelized our simulation code kuES2. We have two merits in parallelizing a simulation code. One is the reduction of computing time, and the other is the magnification of simulation scale owing to the increase of available memories. Especially in particle simulations, the enhanced thermal fluctuations, which are determined by the number of superparticles, sometimes disturb physical phenomena in simulations. We can increase the number of available superparticles in simulation system and suppress the enhanced thermal fluctuations by parallelizing simulation codes. The effects of the enhanced thermal fluctuations in particle simulations are discussed in the next section.

We have two methods to parallelize a particle code, "region dividing method" and "particle dividing method" [*Akiyama et al.*, 1997].

Region dividing method The concept of "Region dividing method" is dividing simulation space as well as particles into the number of processors, as schematically illustrated in Figure 4.1. Each processor calculates time evolutions of field variables of the divided space and motions of the particles therein. This method is widely used in parallelizing MHD simulation codes or so-called hybrid codes. In this region dividing method, though we have to exchange particle data between processors when particles move across the separated regions, we can calculate time evolutions of field variables in each processor without communicating to other processors. In parallelizing a particle code, this method is effective for simulation runs in which the number of particles in each grid is small and the motions of particles are inactive.

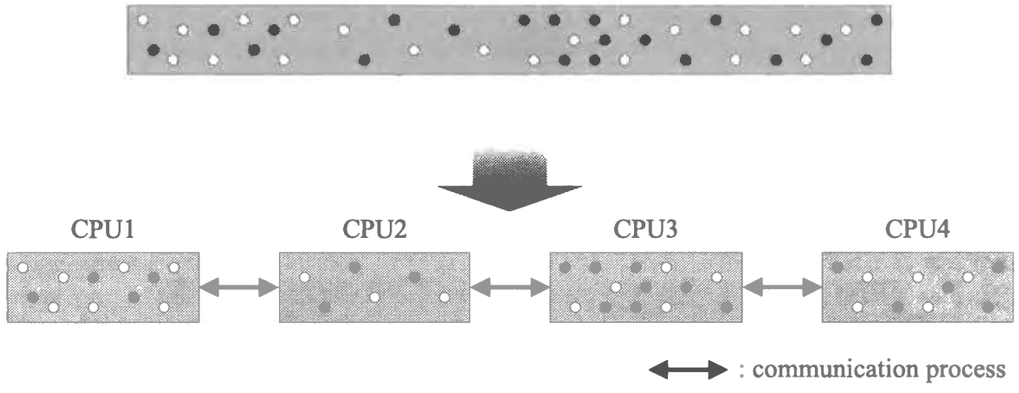

Figure 4.1: Schematic drawing of the region dividing method in parallelizing a particle code. The concept of this method is dividing both space and particles to each processor. Each processor calculates time evolutions of field variables in the divided space and motions of the particles therein.

Liewer et al. [1989] adopted the region dividing method in parallelizing their one- and two-dimensional PIC code (GCPIC). They also proposed another method of dividing simulation space and particles therein dynamically to equalize CPU loads of each processor [*Liewer et al.*, 1989; *Fox et al.*, 1994]. In addition, KEMPO1 (one-dimensional KEMPO) was also parallelized with this method [*Ueda et al.*, 1997]. In simulations performed in the present study, however, we use a large number of superparticles in each grid, and the motions of particles are very active. Therefore, this region dividing method is not effective in the present study. We adopted another method in parallelizing our particle code.

Particle dividing method The concept of "Particle dividing method" is dividing only particles into the number of processors and distributing the divided particles to each processor, as schematically illustrated in Figure 4.2. Each processor calculates motions of the divided particles and field variables in all the simulation space. In this particle dividing method, since the processor in which the motion of each particle is solved is determined at the simulation start time and this relation never change wherever the particle moves to, these is no need to exchange particle data among processors. On the other hand, to calculate time evolutions of field variables, we have to exchange all the field data among all the processors. In parallelizing

a particle code, therefore, this method is very effective for simulation runs with a huge number of particles in each grid. Since simulation runs in the present study need a huge number of superparticles in the simulation system as stated above, we adopted this particle dividing method in parallelizing our particle code kuES2. The particle dividing method is easy to control and very efficient in equalizing CPU loads of each processor.

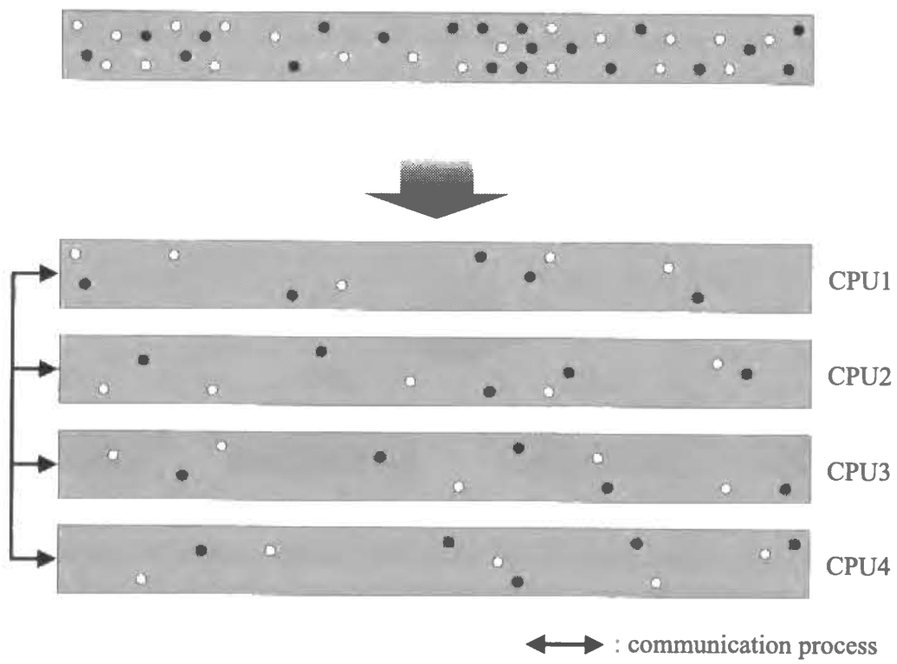

Figure 4.2: Schematic drawing of the particle dividing method in parallelizing a particle code. The concept of this method is dividing only particles to each processor. Each processor calculates motions of the divided particles and time evolutions of field variables in all the simulation space.

In parallelizing a particle code with the particle dividing method, we can divide simulation space as well as particles individually to reduce occupied memory area and calculating time. On the contrary to the region dividing method, the simulation space and the particles are divided individually, and there still need to exchange all the field data among all the processors to calculate time evolutions of the field variables. In simulation runs in the present study, however, almost all the calculation time is used to calculate motions of particles and the calculation time for field data is almost negligible. In addition, the memory area occupied by field data is much smaller than those for particle data in simulation runs with a large number of superparticles in each grid. In a two-dimensional electrostatic particle simulation run with 256 particles in each grid, for example, memory area for field data is only 7% of that for particle data. We have no merit in dividing simulation space in such simulations but have some demerit of increasing communication processes. Therefore, we do not divide simulation space in parallelizing our simulation code.

As stated above, there is no need to exchange particle data in calculating motions of the

divided particles in the particle dividing method. This is because the collisionless plasma is assumed and particles do not interact with each other in kuES2. When we treat plasma phenomena with collisions among simulated particles, we have to exchange particle data among processors and communication processes must increase.

4.2 Enhanced thermal fluctuations in particle code

In the previous section, we mentioned to the "superparticle model" method which is adopted in kuES2. Although this method is indispensable for particle codes, we cannot avoid numerical effects on thermal fluctuations in computer simulations. By using "superparticle model", thermal fluctuations in the simulation system is much enhanced in comparison with those in the real space plasma. Thermal fluctuations are defined by the thermal energy of one plasma particle, given as $\frac{1}{2}m_s v_{ths}^2$. Since one superparticle has much larger mass than one real plasma particle has, one superparticle has much larger thermal energy, and thermal fluctuations are much enhanced in particle code [*Ueda et al.*, 1994]. These enhanced thermal fluctuations are termed "numerical thermal fluctuations", and they give rise to non-physical effects in particle simulations. They sometimes change or extinguish plasma phenomena in particle simulations.

In one-dimensional simulations, effects of the enhanced thermal fluctuations are found as numerical particle diffusion. Especially in the present study, this effect is found as a diffusion of electrostatic potential structure formed by the electron dynamics. Since ions have much larger mass than electrons have ($m_i/m_e = 100$ in the present simulations), this diffusion is mainly due to the enhanced thermal fluctuations of ions. As the same reason, electrons tend to be diffused more than ions, and electrostatic potential structures formed by electrons are easily diffused by thermal fluctuations of ions. In this study, since we are estimating the long time stability of electrostatic potential structures formed by electrons, these enhanced thermal fluctuations sometimes critically affect simulation results. It is possible that this diffusion numerically extinguish spatial potential structures which are stable in the real space plasma with less enhanced thermal fluctuations.

To suppress thermal fluctuations for a long time in particle simulations, the only available method is to use a very large number of superparticles in the simulation system. Since the thermal fluctuations in particle simulations are determined by the thermal energy of one superparticle, the larger number of superparticles is used in simulation system, the more thermal fluctuations are suppressed. This method is easily available, however, it needs very large memory area and computing time.

In two-dimensional simulation runs, on the other hand, effects of the enhanced thermal fluctuations also critically affect during the initial wave growth phase. Since the initial thermal fluctuations become sources of unstable waves, this fluctuation level affects the saturation amplitudes of these waves. Assuming the initial thermal fluctuations are much enhanced, even waves with only small growth rates reach relatively large amplitudes. These weak waves cannot be observed in the real space plasma, because the thermal fluctuations are much more suppressed, and there is no enough time as well as energy for these waves to grow from such a low fluctuation level.

We are going to make some detailed explanation. To make a problem simple, we make one assumption that the saturation energy level of the unstable wave with the maximum growth rate is independent of the initial conditions. In this case, when a certain wave has a constant

growth rate γ, the time period for saturation T_s is given by

$$T_s = \frac{1}{\gamma} \ln \frac{E_s}{E_i} \tag{4.7}$$

where E_s and E_i represent the saturation energy and the initial energy of electric field, respectively. The initial energy of electric field is so-called noise energy level in the simulation system, and it is determined by the initial thermal fluctuations. This equation indicates that the time period for saturation T_s is inversely proportional to the growth rate γ. Now, we assume two unstable waves with different positive growth rates γ_1 and γ_2 ($\gamma_1 > \gamma_2$), and compare energies of these two waves at the saturation time. In this case, wave-1 saturates faster than wave-2 because of the difference of their growth rates. The time period for saturation of wave-1, T_{s1}, is given by Equation 4.7 as

$$T_{s1} = \frac{1}{\gamma_1} \ln \frac{E_s}{E_i} \tag{4.8}$$

When wave-1 becomes saturated, the velocity distribution is modified due to nonlinear wave-particle interactions, then the growth of not only wave-1 but also wave-2 are interrupted. The energy of wave-2 at this time (T_{s1}) is given by

$$\begin{aligned} E_2 &= E_i e^{\gamma_2 T_{s1}} \\ &= E_s^{\gamma_2/\gamma_1} E_i^{1-\gamma_2/\gamma_1} \end{aligned} \tag{4.9}$$

The ratio of the energies of these two waves at T_{s1}, E_2/E_1, is given by

$$\begin{aligned} \frac{E_2}{E_1} &= \frac{1}{E_s} E_s^{\gamma_2/\gamma_1} E_i^{1-\gamma_2/\gamma_1} \\ &= \left(\frac{E_i}{E_s}\right)^{1-\gamma_2/\gamma_1} \end{aligned} \tag{4.10}$$

The point of this equation is that the energy ratio of two waves at the saturation time E_2/E_1 depends on the initial thermal fluctuations E_i. The energy of the weaker wave at the saturation time becomes larger, when the thermal fluctuations are enhanced.

Figure 4.3 presents one sample case of this effect of the initial thermal fluctuations. This figure shows time histories of E field energies of waves with different growth rates in different initial thermal fluctuations. In this figure, it is obvious that E field saturation energies of weaker waves, E_{2s_1} and E_{2s_2}, depend on the initial thermal fluctuation levels, E_{i1} and E_{i2}. The E field saturation energy of the weaker wave in the large initial thermal fluctuations E_{2s_2} is much higher than that in the small initial thermal fluctuations E_{2s_1}.

This effect of the initial thermal fluctuations indicates that even waves with small growth rates will be excited to have relatively larger amplitudes in particle simulations, where the thermal fluctuations are numerically enhanced in comparison with those in the real space plasma. According to the linear dispersion analysis in Section 3.2, oblique mode waves are estimated to be excited with different growth rates in the different directions to the ambient magnetic field in this two-dimensional simulation study. Due to the enhanced thermal fluctuations, even oblique mode waves with smaller growth rates than that of the parallel propagating wave will be excited up to have relatively large amplitudes. It is possible that these enhanced oblique mode

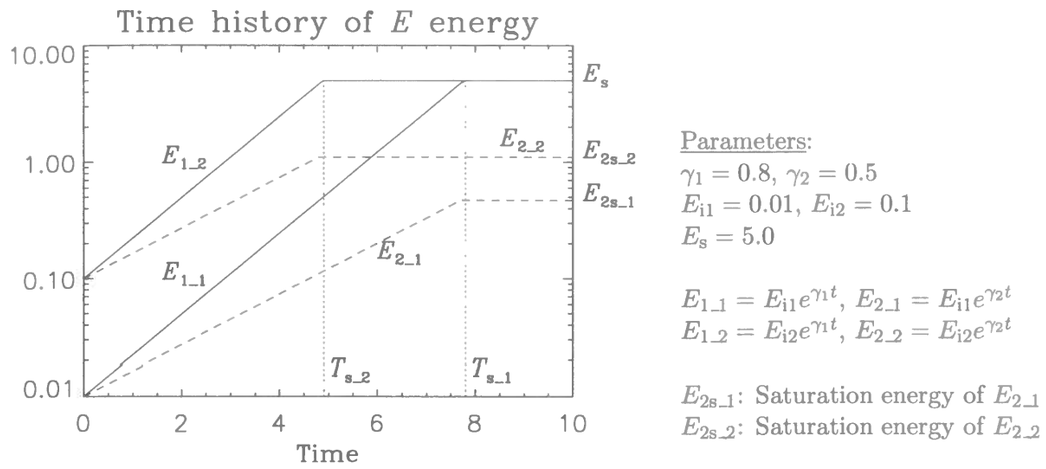

Figure 4.3: Time histories of E field energies of waves with different growth rates. Solid and dotted lines indicate that E field energies of waves with larger and smaller growth rates, respectively. This figure represents effects of the initial thermal fluctuations on the saturation levels of waves.

waves affects critically and sometimes change simulation results in these two-dimensional simulations. We will discuss these effects of the enhanced thermal fluctuations in two-dimensional simulations in Section 6.4.5.

We can apply two possible methods to suppress these initial thermal fluctuations in particle simulations. One is to use much larger number of superparticles in the simulation system. This method is very easy to apply but needs very large computer resources, as mentioned above. The other is so-called "quiet start" method [e.g., *Okuda*, 1984]. In this method, the phase space is loaded as uniformly as possible which has interesting characteristics. For a spatially uniform Maxwellian in the one-dimensional system, for example, quiet start can be obtained by loading superparticles uniformly in x and repeating the velocities used to represent a Maxwellian velocity distribution at one location in x for all the values of different x. In this way, an uniform phase space is maintained and there would be no random noise associated with the initial loading. If a plasma is intrinsically unstable with respect to plasma instabilities, the initial noise associated with machine round-offs will grow to a large amplitude until limited by nonlinear effects. We apply this quiet start method in our particle code kuES2, and use this method to make uniform distributions of particles in simulation systems in two-dimensional particle simulations studied in Chapter 6. It is noted that this quiet start method is useful to suppress the initial thermal fluctuations, but it cannot suppress the enhanced thermal fluctuations throughout the simulation time. To suppress the enhanced thermal fluctuations throughout the simulation time, the only available method is increasing the number of superparticles, as mentioned above in this section.

4.3 Simulation model for ESW

In the present study, we performed one- and two-dimensional computer simulations. The basic parameters for all the simulation runs are listed in Table 4.1. Other parameters depending on

1D computer simulations

Grid spacing	Δr	=	0.20
Time step	Δt	=	0.05
Number of grid points	n_x	=	1024
Total electron plasma frequency	Π_e	=	1.00
Ion plasma frequency	Π_i	=	0.10
Ion to electron mass ratio	m_i/m_e	=	100

2D computer simulations

Grid spacing	Δr	=	1.00
Time step	Δt	=	0.10
Number of grid points	$n_x \times n_y$	=	64×64 128×128
Total electron plasma frequency	Π_e	=	1.00
Ion plasma frequency	Π_i	=	0.10
Ion to electron mass ratio	m_i/m_e	=	100

Table 4.1: Basic simulation parameters in all the computer simulations performed in the present study. These parameters are used in one- and two-dimensional computer simulation runs, respectively.

the initial conditions of each run are presented and explained in each chapter.

We assume two components of electrons, beam and background electrons, and one component of ions in the simulation system. The electron beam is drifting against the background electrons with a drift velocity v_d, and the ions are drifting with v_{di}.

Initial distribution functions As the initial condition, all the particles, electrons and ions, have drifting maxwellian velocity distribution functions given by

$$f_s(v) = \frac{n_s}{\sqrt{2\pi} v_{ts}} \exp\left(-\frac{(v - v_{ds})^2}{2v_{ts}^2}\right) \tag{4.11}$$

where the subscripts $s = 1$, 2, and i represent the two electrons and the ion, and n_s and v_{ts} represent the density and the thermal velocity of each species, respectively. In the present study, we regard the second electrons as background electrons, i.e., $v_{d2} = 0.0$. As mentioned in Section 3.1, three typical electron beam instabilities, "two-stream instability", "weak-beam instability" and "bump-on-tail instability", are studied as the initial electron beam instabilities. The velocity distribution functions of electrons of these initial instabilities are already presented in Figure 3.1.

Since we assume only one ion component, the ion density is equal to the total density of electrons ($n_i = n_1 + n_2$). The total density is kept constant for all simulation runs, which is specified by the total electron plasma frequency defined as

$$\Pi_e \equiv \sqrt{\frac{(n_1 + n_2)e^2}{m_e \epsilon_0}} \tag{4.12}$$

Assuming $\Pi_e = 1.0$, frequencies are normalized to the total plasma frequency in this study. The time t is also scaled according to the electron plasma oscillation period T_{pe}.

Simulation parameters We performed simulation runs varying the following parameters, electron beam density ratio R, temperature of background electrons T_2, temperature of ions T_i and drift velocity of ions v_{di} in one-dimensional computer simulations. We studied generation mechanism of ESW and estimated necessary conditions for stable ESW formation in the one-dimensional system. On the other hand, in two-dimensional computer simulations, we performed simulation runs of the two types of electron beam instabilities, the bump-on-tail instability and the two-stream instability. In the two-dimensional simulations of the bump-on-tail instability, we varied only one parameter, the magnitude of the ambient magnetic field $\boldsymbol{B}_0$. In these simulations, we mainly analyze spatial structures of ESW and detailed mechanism of ESW formation. While in the two-dimensional simulations of the two-stream instability, we performed two series of simulation runs with and without ion dynamics. We performed simulation runs without ion dynamics varying two parameters, the magnitude of the ambient magnetic field $\boldsymbol{B}_0$ and temperature of electrons T_e. We studied parametric dependence of ESW formation and the spatial structures of ESW in the two-dimensional system. Then, we performed simulation runs including ion dynamics and investigated effects of ion dynamics on the stability and the time evolution of the spatial structures of ESW.

Simulation system In one-dimensional computer simulations, the simulation system is purely one-dimensional taken along the x axis with a periodic boundary. Since we study electron beam instabilities along the ambient magnetic field, the magnetic field, the drift velocities of electron and ion beams are also taken along the x axis as schematically illustrated in Figure 4.4. As the initial condition, an electron beam is drifting against background electrons with a drift velocity v_d and ions are flowing with an ion drift velocity v_{di}.

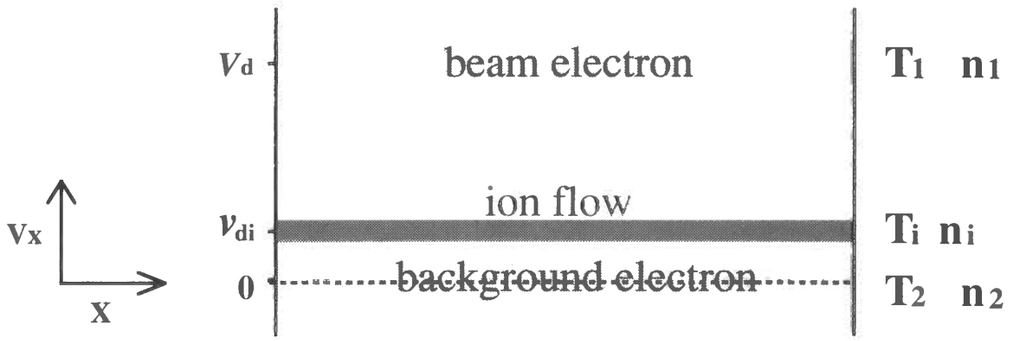

Figure 4.4: Simulation model of electron beam instability in one-dimensional system drawn in x-v_x phase diagram.

In two-dimensional computer simulations, the simulation system is taken in the x-y plane with both periodic boundaries. The ambient magnetic field is taken along the x axis and an electron beam is drifting with a drift velocity v_d along the magnetic field. This initial condition is schematically illustrated in Figure 4.5. This figure schematically presents the initial condition

of electrons in the two-dimensional system. Ions are placed uniformly in all over the simulation system as a background component.

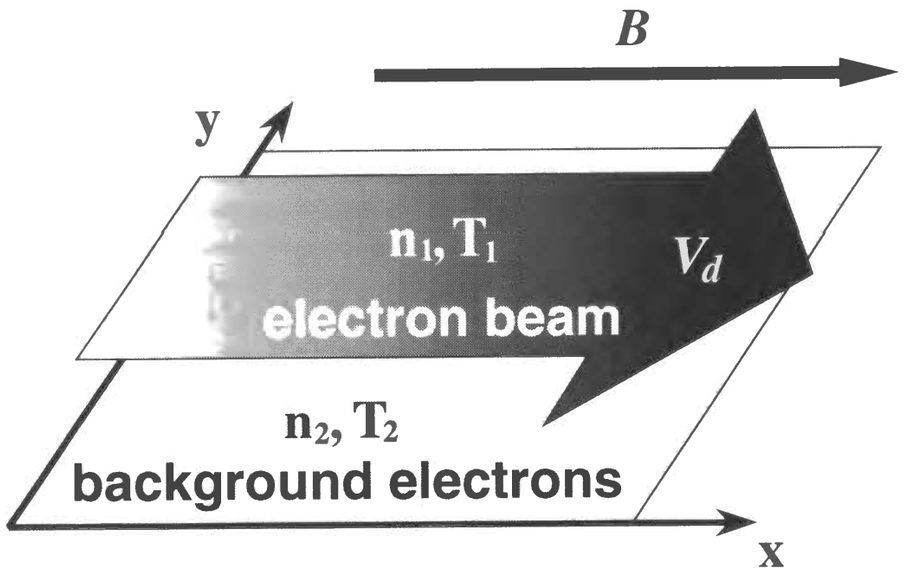

Figure 4.5: Simulation model of electron beam instability in two-dimensional system.

Chapter 5

One-dimensional Simulation Study of ESW

In this chapter, we perform one-dimensional electrostatic particle simulations of several electron beam instabilities for various plasma parameters. Then, we present results of one-dimensional simulation runs and discuss parametric dependence on the formation mechanism and the stability of ESW in the one-dimensional system [*Omura et al.*, 1994, 1996]. In this one-dimensional simulation study, we performed simulation runs of three types of electron beam instabilities, the two-stream instability, the weak-beam instability and the bump-on-tail instability. These instabilities are expected as possible generation mechanisms of ESW, as presented in Section 3.1.

It is noted that we use the term "potential structure" to express quasi-stationary spatial structures of potentials in the present study. This term does not indicate net potential drops found in auroral double layers.

5.1 One-dimensional particle simulations

5.1.1 Model and parameters

In one-dimensional simulations, the simulation system is taken along the x axis as mentioned in Section 4.3. The magnetic field, the drift velocities of electron and ion beams are assumed along the x axis. Since we only take into account the electrostatic field E_x and velocities of particles along the ambient magnetic field, the dynamics of electrons and ions are not affected by the magnetic field.

In this one-dimensional simulation study, we performed simulation runs of three electron beam instabilities, the two-stream instability, the weak-beam instability and the bump-on-tail instability. At first, we performed simulation runs of these electron beam instabilities without ion dynamics. Next, we performed simulation runs including ion dynamics varying temperature of ions T_i and drift velocity of ions v_di. Temperatures are defined by thermal velocities of particles in computer simulations, so that we use thermal velocities as parameters changing temperatures of particles. We have four simulation parameters, electron beam density R, thermal velocity of background electrons $v_{\mathrm{t}2}$, thermal velocity of ions v_ti and drift velocity of ions v_di. Velocities are normalized to the thermal velocity of the background electrons in the simulation runs of the bump-on-tail instability. In all the one-dimensional simulation runs in this thesis, the drift velocity of the electron beam v_d is kept constant as 2.0. Velocities and lengths are scaled by v_d and $v_\mathrm{d}/\Pi_\mathrm{e}$, respectively.

We will present ten results of one-dimensional simulation runs. The varied parameters for different simulation runs are listed in Table 5.1. Three typical electron beam instabilities are expressed by the electron beam density R and the thermal velocity of the background electrons

Run	R	$v_{\rm di}$	$v_{\rm t1}$	$v_{\rm t2}$	$v_{\rm ti}$
Run A	0.50	—	0.1	0.1	—
Run B	0.03	—	0.1	0.1	—
Run C	0.03	—	0.1	1.0	—
Run D	0.50	0.0	0.1	0.1	0.1
Run E	0.50	0.0	0.1	0.1	1.0
Run F	0.03	0.0	0.1	1.0	0.1
Run G	0.03	0.0	0.1	1.0	1.0
Run H	0.50	1.0	0.1	0.1	1.0
Run I	0.03	1.5	0.1	1.0	0.1
Run J	0.03	1.5	0.1	1.0	1.0

Table 5.1: Plasma parameters in one-dimensional computer simulations, parameters of beam and background electrons [Runs A∼C] and those of beam and background electrons and ions [Runs D∼J] in each simulation run.

$v_{\rm t2}$. Electron beam density R and thermal velocity of the background electrons $v_{\rm t2}$ are decided as follows; $R = 0.5$ and $v_{\rm t2} = 0.1$ in simulation runs of the two-stream instability [Runs A, D, E, H], $R = 0.03$ and $v_{\rm t2} = 0.1$ in those of the weak-beam instability [Run B], $R = 0.03$ and $v_{\rm t2} = 1.0$ in those of the bump-on-tail instability [Runs C, F, G, I, J]. In this table, Run A∼C are simulation runs without the ion dynamics, the rest Runs D∼J are those including the ion dynamics. Other common parameters are listed in Table 4.1 in Section 4.3.

The number of superparticles used for simulation runs is about 1,000,000 for electrons and 8,000,000 for ions. It is noted that we need to use a large number of superparticles to avoid numerical particle diffusion due to the enhanced thermal fluctuations, as mentioned in Section 4.2. Especially to analyze the stability of ESW for a long time period, it is very important to suppress the enhanced thermal fluctuations.

5.1.2 Time evolutions of ESW formation

To analyze time evolutions of one-dimensional simulations, we show x-v_x phase diagram of electrons at different times. In Figure 5.1(a), we present a sample of x-v_x phase diagram of electrons and corresponding E_x and potential plots. We can confirm that a vortex of electrons in x-v_x phase diagram corresponds a spiky waveform of E_x and a positive potential structure. In the present study, this x-v_x phase diagram plot is very useful to analyze potential structures as well as electron distributions.

At first, we performed three simulation runs, the simulation run of the two-stream instability [Run A], the run of the weak-beam instability [Run B] and the run of the bump-on-tail instability [Run C]. In these three simulation runs, the dynamics of ions is neglected. Ions are distributed uniformly and they are fixed as particles with infinite mass in the simulation system.

Two-stream instability First of all, we performed an one-dimensional electrostatic particle simulation of the electron two-stream instability. The initial distribution functions of electrons

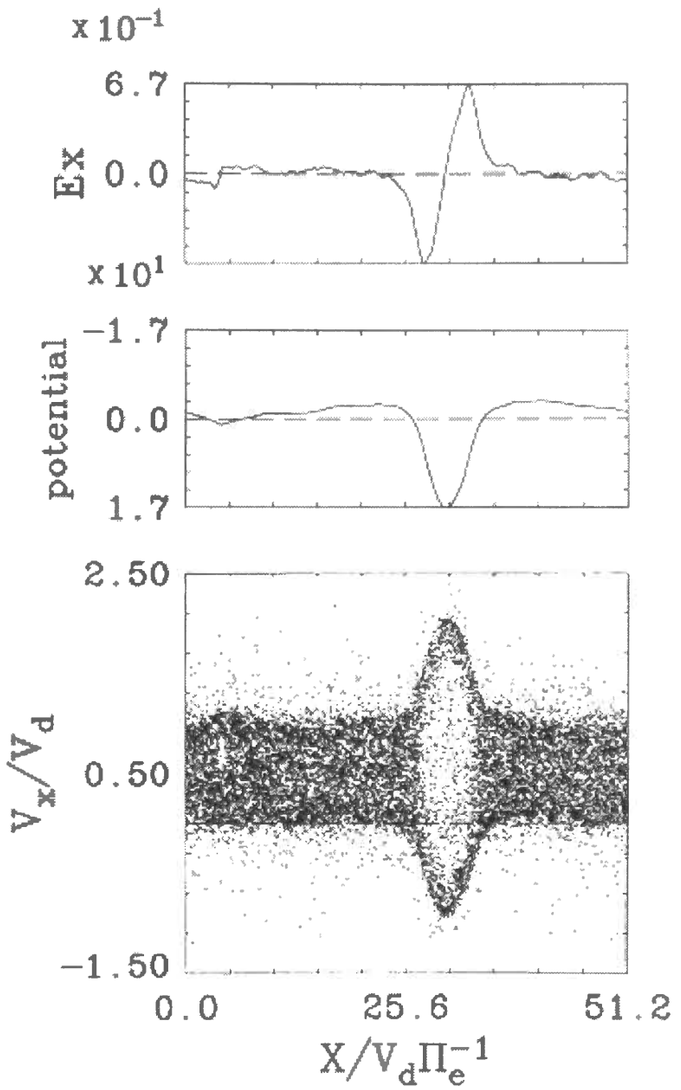

Figure 5.1: Example of x-v_x phase diagram of electrons and corresponding E_x and potential plots in the one-dimensional system.

in this simulation is shown in Figure 3.1(a), and simulation parameters are listed in Run A of Table 5.1.

Figure 5.2 presents x-v_x phase diagrams (left panels) and corresponding distribution functions of electrons $f(v_x)$ (right panels) at different times. In this figure, x and v_x are scaled by $v_\mathrm{d}/\Pi_\mathrm{e}$ and v_d, respectively. In the left column, we can find that one vortex is formed in the bottom figure. As mentioned above, this vortex corresponds an electrostatic potential formed by electrons.

In this simulation run, time evolution of potentials is as follows. At first, the initial electron two-stream instability is excited, then many vortices are formed as shown at $t = 4.08 \times T_\mathrm{pe}$ in Figure 5.2. Since these vortices have different drift velocities, they coalesce with each other and grow larger, finally one large vortex is formed, as shown at $t = 40.74 \times T_\mathrm{pe}$ in this figure. This vortex corresponds an electrostatic potential, as presented in Figure 5.1. This electrostatic potential formed after coalescence process is very stable, and this is a BGK potential which corresponds to ESW. This BGK potential is drifting with almost a half of the drift velocity of the initial electron beam ($v_\mathrm{ESW} \simeq v_\mathrm{d}/2$), which is consistent with the phase velocity of the beam-mode waves expected in Section 3.2.

In the right column of Figure 5.2, the distribution functions of electrons $f(v_x)$ at different times are presented. We can see that both cold beam and background electrons are thermalized by the initial instability. Through this thermalization process, electrons become to have thermal velocities almost a half of the drift velocity of the initial electron beam $v_\mathrm{d}/2$. In the final state ($t = 130 \times T_\mathrm{pe}$), electrons form a flat top distribution. This is because the gap in the velocity space is filled due to Landau damping, forming a plateau between the initial two electron beams. In addition, we can see a flat high-energy tail in this distribution function. This high-energy tail is formed by electrons which are accelerated by to large velocities the BGK potential.

Weak-beam instability Next, we performed a simulation of the electron weak-beam instability with a very small electron beam density $R = 0.03$. The initial distribution function of electrons in this simulation is shown in Figure 3.1(b), and simulation parameters are listed in Run B of Table 5.1.

In Figure 5.3, we present x-v_x phase diagrams and corresponding electron velocity distribution functions at different times in this simulation of the weak-beam instability. The left column shows x-v_x phase diagrams. As we found in Figure 5.2, a strong electron beam instability is excited, then many electrostatic potentials are formed in the initial phase ($t = 16.30 \times T_\mathrm{pe}$). These potentials, however, do not grow and they are diffused in time. In the final state ($t = 130.35 \times T_\mathrm{pe}$), electrons are thermalized at all, and there exists no significant potential structure in the simulation system.

The right column in Figure 5.3 shows that the beam electrons spread over the velocity space, forming a plateau over the velocity range between the drift velocities of the electron beam and the background electrons. While the background electrons are not much affected by this diffusion process. The electron beam is diffused gradually filling the gap in the velocity space between the electron beam and the background electrons. As is well known, this process is described by the quasi-linear theory [*e.g.*, *Nicholson*, 1983]. Langmuir waves with smaller phase velocities are subsequently excited due to Landau damping, till positive gradients in the velocity distribution function are extinguished.

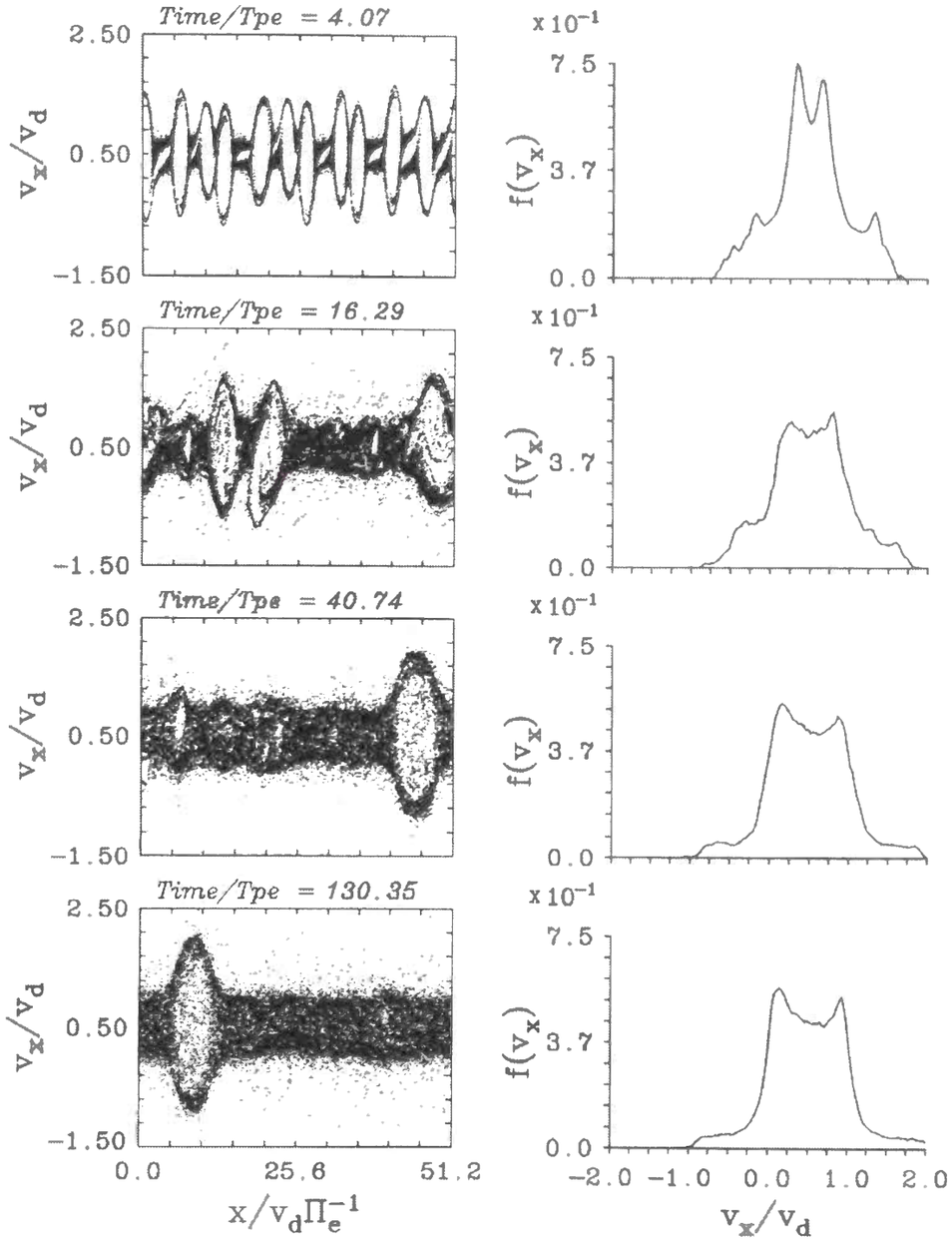

Figure 5.2: Time evolution of the two-stream instability [Run A in Table 5.1]. Left and right columns present the x-v_x phase diagrams of electrons and the corresponding electron velocity distribution functions $f(v_x)$ at $t = 4$, 16, 40, $130 \times T_\mathrm{pe}$, respectively.

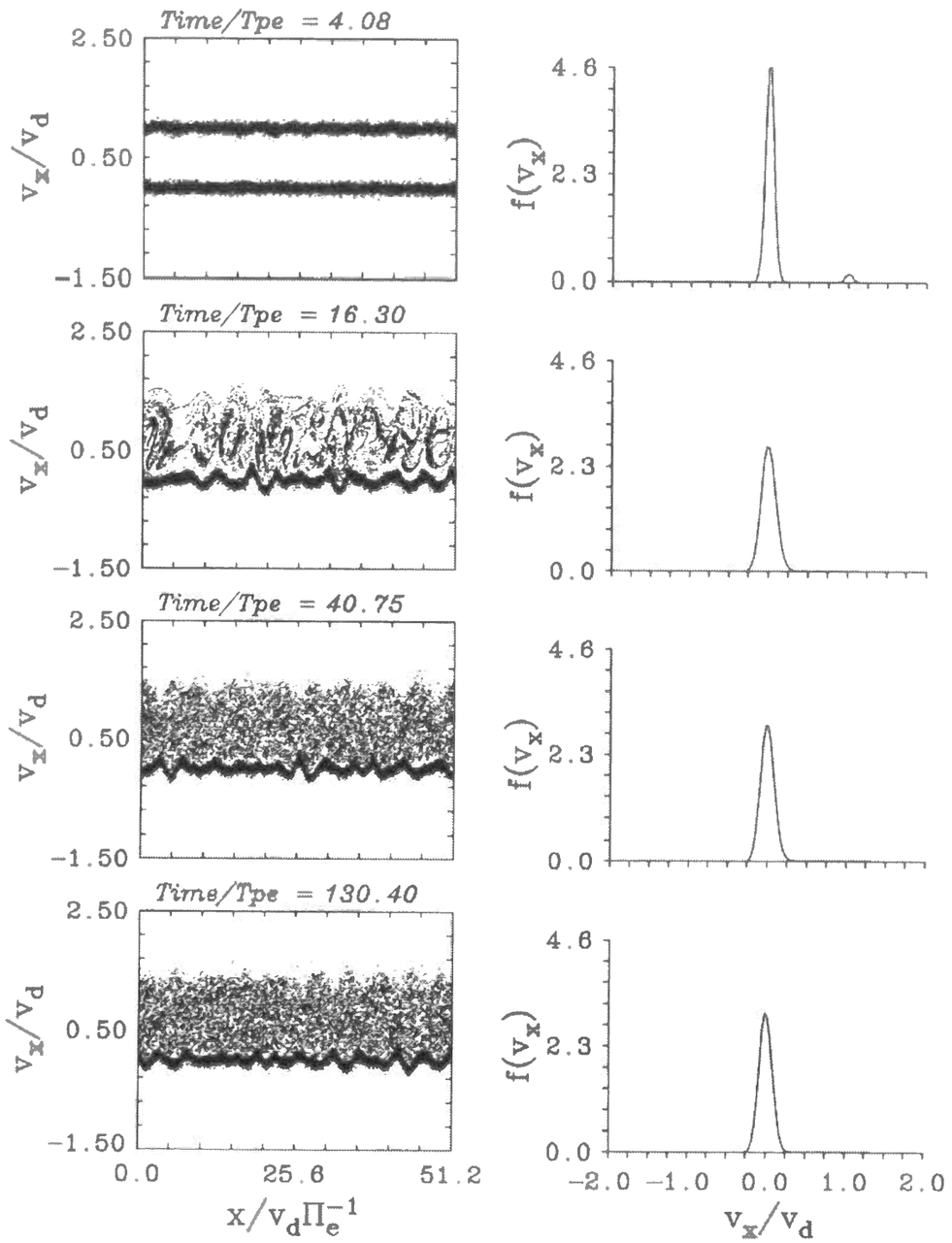

Figure 5.3: Time evolution of the weak-beam instability [Run B in Table 5.1]. Left and right columns present the x-v_x phase diagrams of electrons and the corresponding electron velocity distribution functions $f(v_x)$ at t = 4, 16, 40, 130$\times T_{\rm pe}$, respectively.

Bump-on-tail instability In Section 3.1, we assumed the bump-on-tail instability as a possible instability to form ESW in the Earth's magnetotail region. We performed a simulation run of the bump-on-tail instability with parameters listed in Run C of Table 5.1. The initial distribution function of electrons in this simulation is shown in Figure 3.1(c).

In Figure 5.4, x-v_x phase diagrams and corresponding velocity distribution functions at different times are presented. In the left column, many vortices are excited by the initial electron bump-on-tail instability in the initial phase ($t = 16.30 \times T_{\rm pe}$). They coalesce with each other forming larger vortices, then isolated vortices are formed in the final state ($t = 130.40 \times T_{\rm pe}$). These isolated vortices correspond to spatially isolated potentials, and these potentials are very stable BGK potentials. This time evolution of potentials are almost the same with that in the simulation run of the two-stream instability [Run A]. In comparison with the two-stream instability, the bump-on-tail instability is a weak instability, and localized in phase space. Therefore, the vortices formed from this instability spread over small range in phase space, and the corresponding BGK potentials have only a small amplitude.

In this case, the positive gradient of the velocity distribution yields positive growth rates due to Landau damping, then the gap of the initial velocity distribution function between the electron beam and the background electrons is filled forming a plateau as presented in the right column of Figure 5.4. Contrary to the previous weak-beam instability, since the positive gradient is localized at a small bump on the high-energy tail of the background electrons, this positive gradient is extinguished in instance, and no further instability is excited. Therefore, potentials excited by the initial instability exist stably in this case, they coalesce with each other, forming isolated BGK potentials. This process of stopping instability is the most important mechanism to form ESW from the bump-on-tail instability.

Figure 5.5 show E_x and corresponding potentials in the final state of the simulation time ($t = 130.40 \times T_{\rm pe}$) in Runs A$\sim$C. Panels (a)$\sim$(c) correspond to Runs A$\sim$C, respectively. We can confirm a clear ESW and a corresponding electrostatic potential in Figure 5.5(a), presenting the results of the two-stream instability. While in Figure 5.5(c), presenting the results of the bump-on-tail instability. some spiky electric fields and corresponding potentials are found. In the simulation run of the bump-on-tail instability [Run C], though it is obvious that stable potentials are formed in the final state, which are shown in the bottom panel of Figure 5.4, the electric fields are contain much noise and clear ESW are hard to be found. This is because the amplitudes of ESW formed from the bump-on-tail instability are very small in comparison with the amplitudes of ESW formed from the two-stream instability. As mentioned above, the bump-on-tail instability is a relatively weak instability in comparison with the two-stream instability. In addition, the growth of this instability saturates in instance, because the positive gradient in the velocity distribution function diminish as soon as the nonlinear trapping occurs. Because of these reasons, ESW with only small electric fields are formed in the bump-on-tail instability. In the real space plasma, however, since the thermal fluctuation is much suppressed, the electric field of ESW contain much less noise, clear ESW are expected to be formed from the electron bump-on-tail instability.

In Figure 5.5(b), presenting the results of the weak-beam instability, on the other hand, not ESW but a quasi-monochromatic wave is observed. This wave is the nonlinearly modulated Langmuir wave. This modulation in amplitudes of the Langmuir wave is explained as the density modulation in space due to the nonlinear beam-mode waves [*Akimoto et al.*, 1996]. As presented in Section 3.2, the electron weak-beam instability excite not linear Langmuir waves

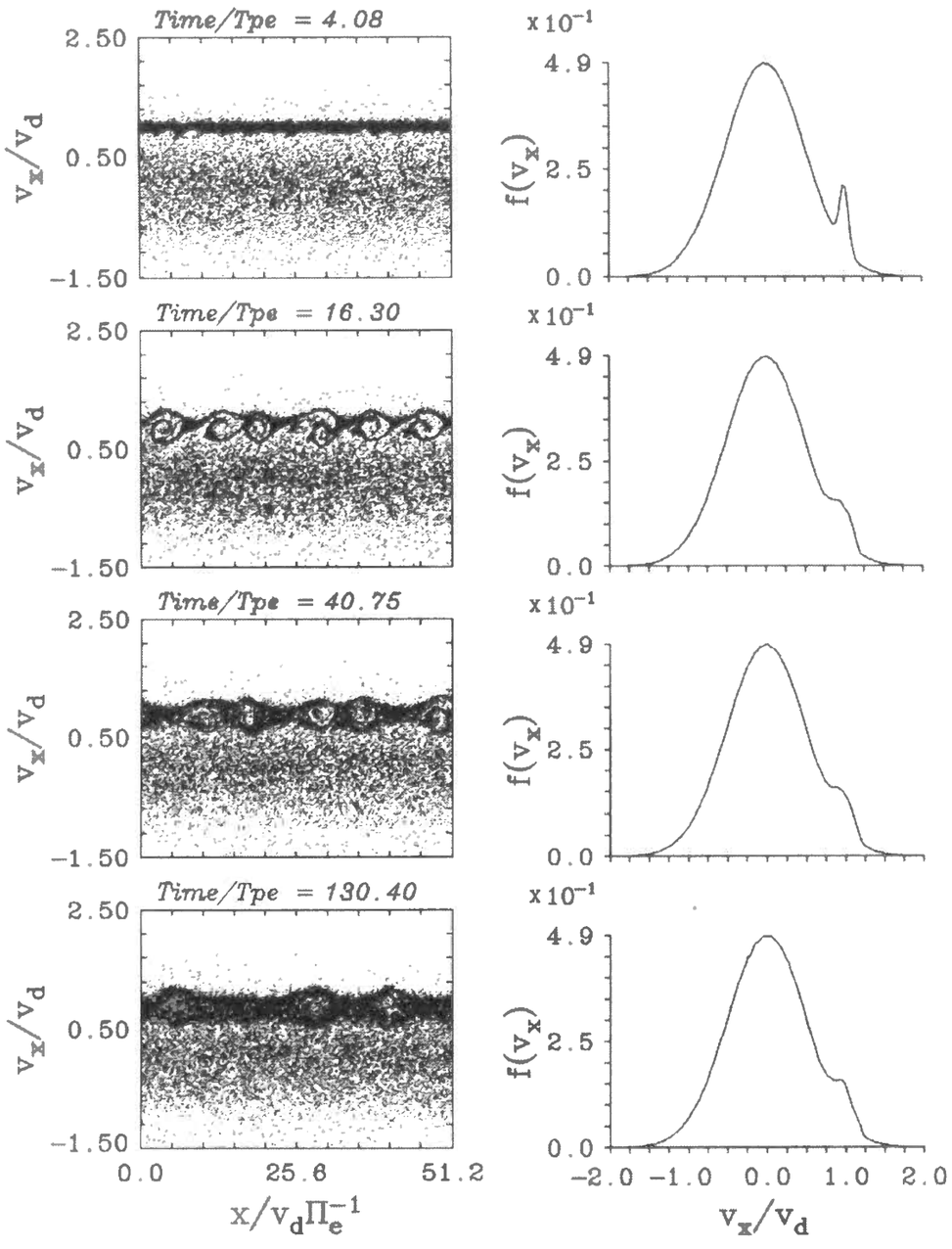

Figure 5.4: Time evolution of the bump-on-tail instability [Run C in Table 5.1]. Left and right columns present the x-v_x phase diagrams of electrons and the corresponding electron velocity distribution functions $f(v_x)$ at t = 4, 16, 40, 130×$T_{\rm pe}$, respectively.

but nonlinear beam-mode waves. In a long time evolution, however, linear Langmuir waves are excited by the background electrons. Since the nonlinear beam-mode waves correspond to the density modulations in space, Langmuir waves excited by the background electrons are spatially modulated by the nonlinear beam-mode waves.

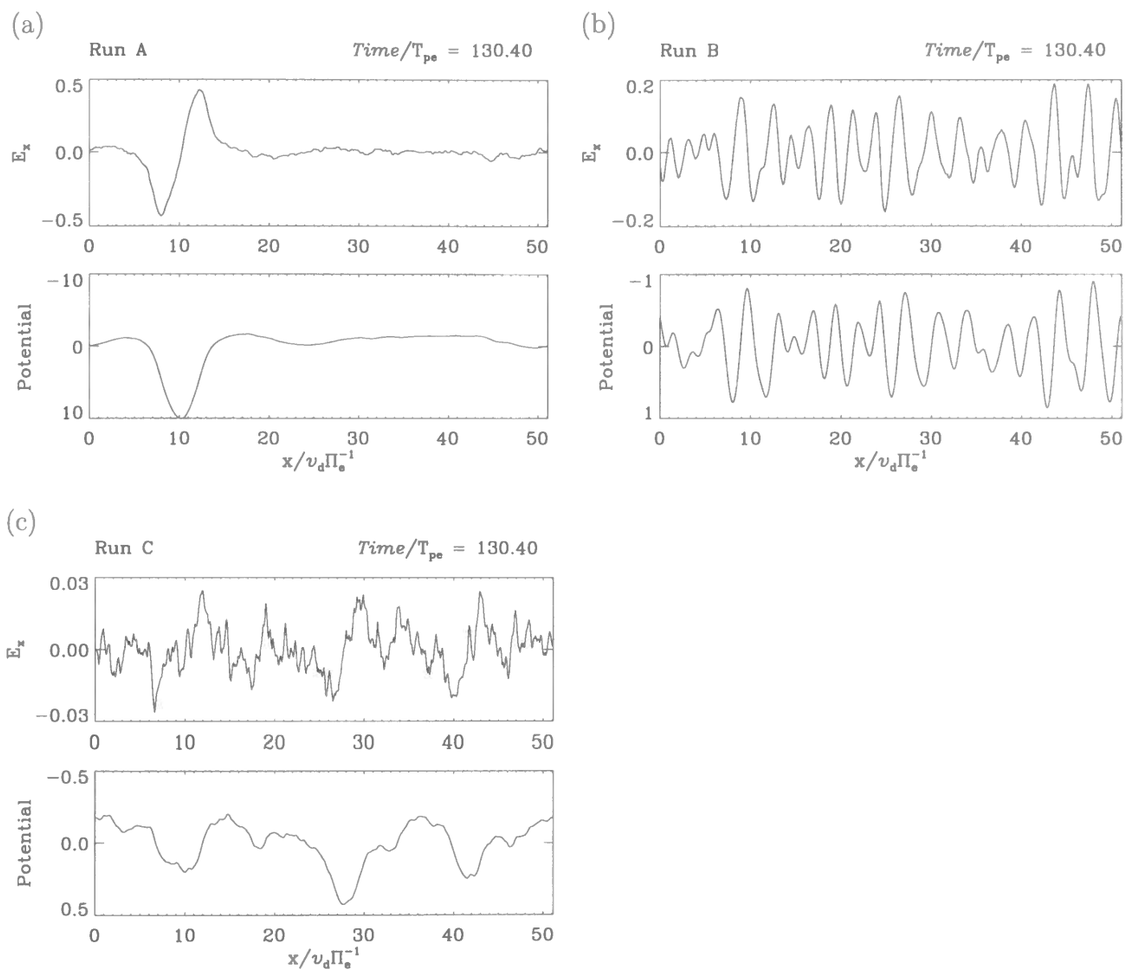

Figure 5.5: E_x and potential plots of three simulation runs in the final state of the simulation time. Panels (a)∼(c) show E_x (upper panel) and potential (lower panel) in (a):the two-stream instability, (b):the weak-beam instability and (c):the bump-on-tail instability, respectively [Runs A∼C in Table 5.1].

Time history of energies

Figure 5.6 represents time histories of E_x energy densities in simulation Runs A∼C. These E_x field energy densities are normalized to the thermal energy density of the background electrons in the bump-on-tail instability (nmv_{t2}^2).

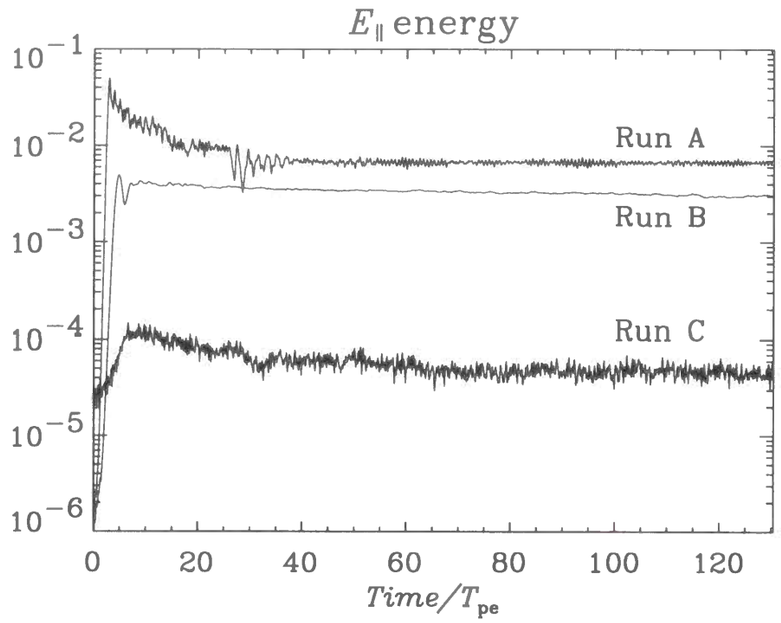

Figure 5.6: Time histories of E_x energy densities in simulation runs [Runs A∼C in Table 5.1].

In this figure, the saturation level of the bump-on-tail instability [Run C] is much smaller than those of the other two instabilities. This is because the growth rate of the bump-on-tail instability is smaller than those of the other two instabilities as well as the growth of the instability stops in instance, as explained above.

The time histories of the electric field energies in the runs of the two-stream instability [Run A] and the bump-on-tail instability [Run C] show quasi-stepwise changes after the initial instability saturate. This quasi-stepwise changes represent the merging of two adjacent ESW. When two adjacent ESW coalesce with each other, the phase mixing process occurs and the energy of potentials is transferred to the thermal energies of particles trapped therein. Through this coalescence process, the parallel electric field energy, in other words the potential energy, decrease in the two-stream and the bump-on-tail instabilities. This decrease of the electric field energy stops, when all the ESW coalesce with each other and only one ESW remains in the simulation system.

In the weak-beam instability [Run B], on the other hand, the electric field energy do not decrease after the initial instability saturate. It keeps almost a constant value throughout the whole simulation time. In the simulation run of the weak-beam instability, stable Langmuir waves are excited and exist stably for a long time. No significant change occurs in this simulation.

Spectrum analysis

Next, we present ω-k diagrams of E_x in simulation runs of these three types of electron beam instability [Runs A∼C] in Figure 5.7. These spectra are obtained by Fourier transforming E_x

in space and time. In this figure, frequencies (ω) are normalized by the electron plasma frequency (Π_e), and wavenumbers (k) are normalized to the Debye length (λ_D) of the thermalized electrons. Figure 5.7(a)∼(c) show the spectra of E_x in simulation runs of the two-stream instability [Run A], the weak-beam instability [Run B] and the bump-on-tail instability [Run C], respectively.

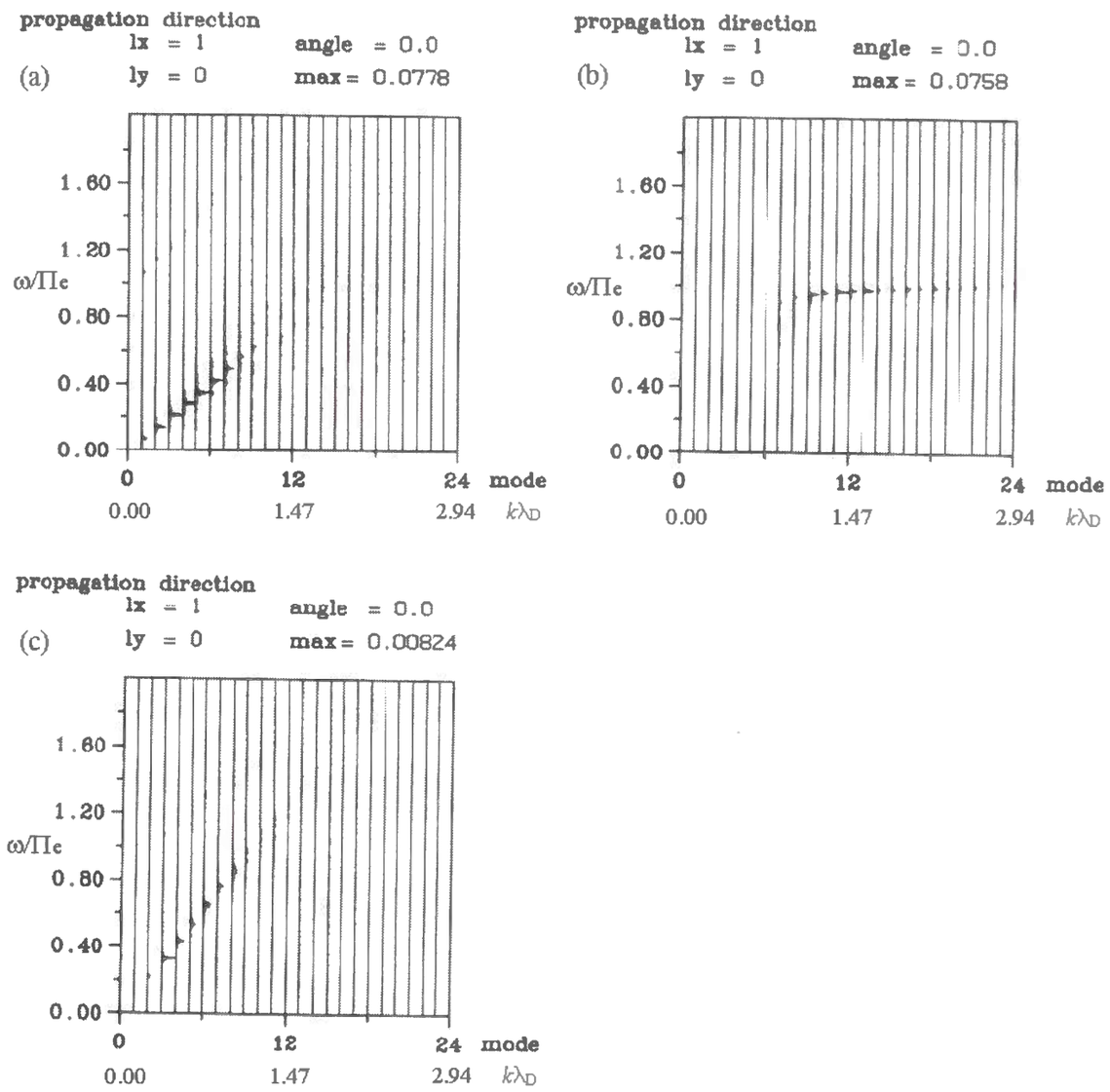

Figure 5.7: The ω-k diagrams of E_x in three simulation runs. Panel (a)∼(c) show the ω-k diagrams of (a):the two-stream instability, (b):the weak-beam instability and (c):the bump-on-tail instability, respectively [Runs A∼C in Table 5.1].

In the two-stream instability, shown in Figure 5.7(a), we can find a strong distinctive wave with a broadband spectra in lower frequency range below Π_e. This wave corresponds to the

potential of ESW drifting against the rest frame of the simulation system as shown in left bottom of Figure 5.2, and its gradient indicates the drift velocity of this potential $v_{\rm ESW} \simeq v_{\rm d}/2$. This broadband spectra corresponds to those of ESW, and this proves the broadband spectra of ESW are generated by drifting electrostatic potentials. We can find other two weak waves propagating forward and backward whose cut off frequency is electron plasma frequency ($\Pi_{\rm e}$). These are Langmuir waves which are normally excited due to linear theory in the thermalized electrons.

In the weak-beam instability, clear Langmuir waves are excited as found in Figure 5.7(b). Though the dispersion of these Langmuir waves is a little modified by the electron beam, it is almost same with the linear dispersion, and they have frequencies close to the plasma frequency $\Pi_{\rm e} = 1.0$. This is because the nonlinear trapping occurs only for the beam electrons, and the background electrons which support Langmuir waves are not involved in this nonlinear trapping dynamics. The weak-beam instability only modify the velocity distribution of the weak beam electrons, while that of the background electrons is not modified. Therefore, characteristics of the linear dispersions remain through out the simulation time, and Langmuir waves supported by the background electrons are also stable in all the simulation time.

In the bump-on-tail instability as shown in Figure 5.7(c), the BGK potentials give a broadband spectra as found in the two-stream instability. The gradient of this spectra also indicates the drift velocity of this potential. Since the potentials of ESW are formed mainly by the beam electrons, its drift velocity $v_{\rm ESW}$ is almost same with, in detail a little smaller than, the drift velocity of the initial electron beam $v_{\rm d}$ ($v_{\rm ESW} \simeq v_{\rm d}$). Since this drift velocity of ESW is higher than that in the two-stream instability, the broadband spectra of ESW from the bump-on-tail instability spread much larger than that of ESW from the two-stream instability. The spectra of the ESW extend clearly up to the plasma frequency in the bump-on-tail instability.

Parametric dependence

We performed and analyzed simulation runs without ion dynamics of three typical electron beam instabilities, the two-stream instability, the weak-beam instability and the bump-on-tail instability. Among these three instabilities, we confirmed ESW formation from the two-stream and the bump-on-tail instabilities.

To estimate dependence of ESW formation on electron beam density, we performed a series of simulations with varying electron beam density $R = n_1/(n_1+n_2)$. In this series of simulations, we changed electron beam density from 0.03 to 0.5 ($R = 0.03 \sim 0.5$), and confirmed a necessary condition of electron beam density for ESW formation that the electron beam density R must be larger than 0.3 ($R \geq 0.3$) to form stable ESW from the two-stream instability [*Omura et al.*, 1994]. When R is relatively small, such electron beam instabilities are termed "weak-beam instability". In other words, ESW are formed from the two-stream instability, but are not formed from the weak-beam instability. The two-stream and the weak-beam instabilities are distinguished by the electron beam density R, and the boundary between these two electron beam instabilities is $R \simeq 0.3$.

Next, we performed a series of simulations of the electron bump-on-tail instability with varying drift velocity of electron beam $v_{\rm d}$, and estimate dependence of ESW formation from the bump-on-tail instability on this parameter. We performed three simulation runs with different drift velocities of electron beam $v_{\rm d} = 0.5, 1.0, 1.5$. In the case of $v_{\rm d} = 1.5$, time evolution of potentials are almost same with that in the simulation Run C, and stable BGK potentials are

formed. While in other cases of $v_{\rm d} = 0.5$ and 1.0, since the initial bump-on-tail instability is too weak, no significant potential structure is formed. ESW formation from the bump-on-tail instability depends on the growth rates of the initial instability, while the drift velocity of electron beam itself have no physical importance on ESW formation from the bump-on-tail instability.

5.1.3 Effects of ion dynamics on ESW stability

The one-dimensional simulation runs without ion dynamics demonstrated that ESW can be formed from the two types of electron beam instabilities, the two-stream instability and the bump-on-tail instability. Next, we performed electrostatic particle simulations of these two electron beam instabilities including ion dynamics, then estimated effects of the ion dynamics on the formation process of ESW in the one-dimensional system. The mass ratio of ions $m_{\rm i}/m_{\rm e}$ is assumed as 100 in the following simulation runs. Among several parameters of ions, we investigated effects of the ion temperature $T_{\rm i}$ and the drift velocity of ions $v_{\rm di}$ against the background electrons in the present study.

Dependence on ion temperature

At first, we studied effects of the ion temperature on the formation process of ESW by performing simulation runs with cold and hot ions. In these simulation runs, the cold ions have the thermal velocity $v_{\rm ti} = 0.1$, while the hot ions have $v_{\rm ti} = 2.0$. As shown in the previous simulations, electrons are thermalized in instance by the initial instability, so that the ion temperature is much smaller than the electron temperature ($T_{\rm i}/T_{\rm e} \ll 1$) in the simulation run with cold ions. while in the case with hot ions, the ion temperature is almost same of larger than the electron temperature ($T_{\rm i}/T_{\rm e} \geq 1$). These ions are located as background ions without a drift velocity ($v_{\rm di} = 0$).

Two-stream instability First, we performed two simulation runs of the electron two-stream instability with cold and hot ions, respectively. As presented in the previous simulation run without ion dynamics, electrons are thermalized by the initial instability in the simulation runs of the two-stream instability. The thermalized electrons have a large thermal velocity almost equal to a half of the drift velocity of the electron beam ($v_{\rm d}/2 = 1.0$). In this case, the temperature of the cold ions is almost 1/100 of the thermalized electrons ($T_{\rm i}/T_{\rm e} \simeq 0.01$). While the temperature of the hot ions is almost 4 times as large as that of the thermalized electrons ($T_{\rm i}/T_{\rm e} \simeq 4$). Simulation parameters in these runs are listed in Runs D and E of Table 5.1, respectively.

In Figure 5.8, x-v_x phase diagrams and velocity distribution functions of electrons in the simulation run with cold ions [Run D] are presented. Left and right columns present the x-v_x phase diagram of both electrons and ions and the corresponding electron velocity distribution function $f(v_x)$, respectively.

In the left column, we can see electrostatic potentials are diffused in time, and there exists no significant potential structure in the final state. Though the final state is very similar to that in the previous run of the weak-beam instability [Run B], electrostatic potentials excited by the initial instability are stable for a while, they grow and coalesce with each other. These

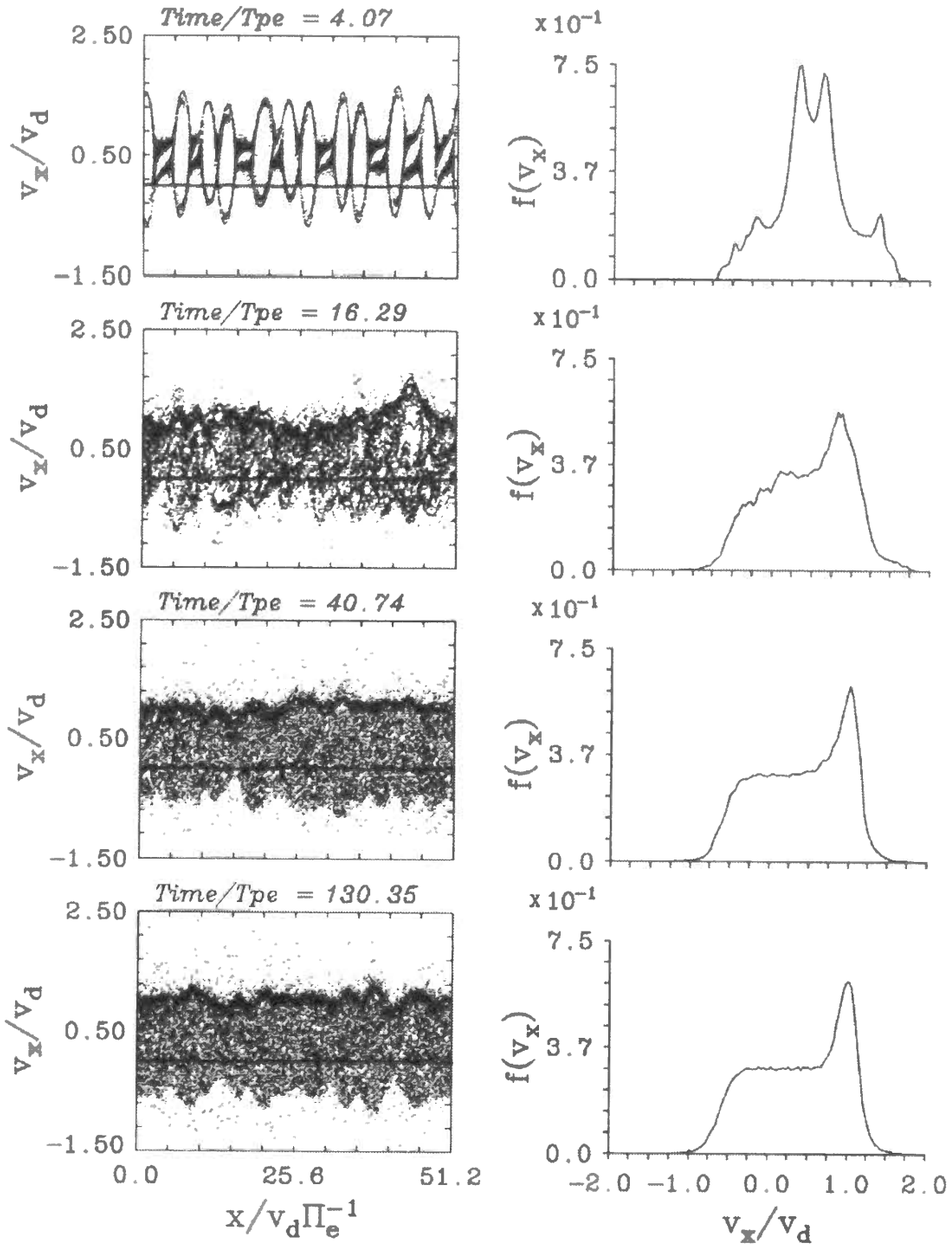

Figure 5.8: Time evolution of the two-stream instability with cold background ions [Run D in Table 5.1]. Left and right columns present the x-v_x phase diagrams and the corresponding electron velocity distribution functions $f(v_x)$ at t = 4, 16, 40, 130×$T_{\rm pe}$, respectively.

potentials, however, are diffused completely. This diffusion is, of course, occurred due to the ion dynamics.

In Figure 5.9, presenting the ω-k diagram of the E_x component, there exist strong waves around the ion plasma frequency ($\Pi_{\rm i}/\Pi_{\rm e} = 0.1$). They are revealed to be ion acoustic waves. These ion acoustic waves are most strongly excited at $k\lambda_{\rm D} \simeq 1.2$. This can be explained as follows. According to the linear theory analyzed in Section 3.2, the two-stream instability excite beam-mode waves, and they have the maximum growth rate at $k_{\rm b}\lambda_{\rm D} \simeq 0.6$, as shown in the left panels of Figure 3.2. These beam-mode waves decay to ion acoustic waves with a twice k number, i.e., $2k_{\rm b}\lambda_{\rm D} \simeq 1.2$.

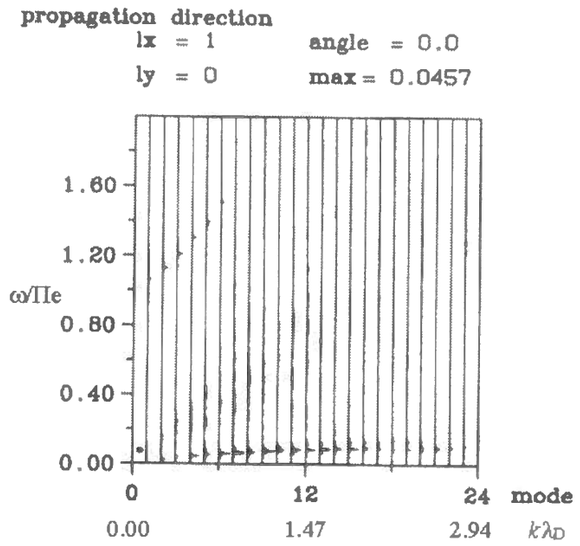

Figure 5.9: The ω-k diagrams of E_x in the simulation run of the two-stream instability with cold ions [Run D in Table 5.1].

This ion acoustic waves diffuse and thermalize electrons with almost same kinetic energies. In this simulation, since ions are placed as a background component without a drift velocity ($v_{\rm di} = 0$), electrons are diffused, forming a plateau at $v_x \simeq 0$ in the velocity distribution function, as shown in the right column of Figure 5.8. In this simulation run of the two-stream instability with cold ions, though the initial two-stream instability excite electrostatic potentials, they decay to ion acoustic waves, and ESW cannot be formed.

In the simulation run of the electron two-stream instability with hot ions, on the other hand, we confirmed the formation of ESW. As found in the left column of Figure 5.10, clear ESW are formed in spite of the existence of ions. On the contrary to the previous simulation [Run D], the electrostatic potentials do not decay to ion acoustic waves.

Figure 5.11 presents the ω-k diagram of E_x in this simulation. We can find no existence of ion acoustic waves in this figure. This is because ion acoustic waves are strongly damped due to the Landau damping, when the ion temperature is higher than the electron temperature ($T_{\rm i}/T_{\rm e} \geq 1$). As mentioned above, the temperature of ions is about four times of that of electrons which are thermalized by the initial two-stream instability ($T_{\rm i}/T_{\rm e} \simeq 4$). Therefore,

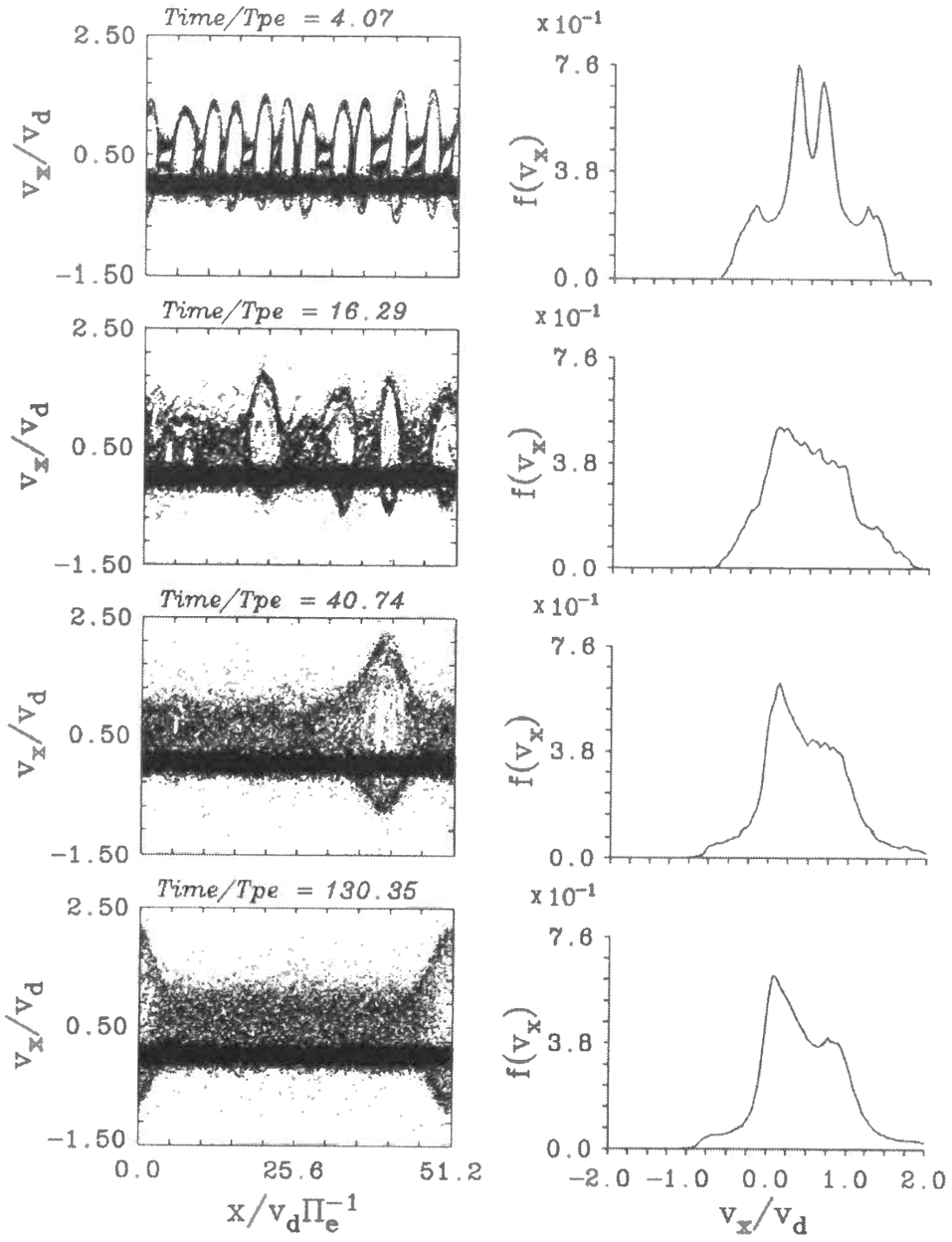

Figure 5.10: Time evolution of the two-stream instability with hot background ions [Run E in Table 5.1]. Left and right columns present the x-v_x phase diagrams and the corresponding electron velocity distribution functions $f(v_x)$ at t = 4, 16, 40, 130×T_{pe}, respectively.

ion acoustic waves are strongly damped due to the Landau damping in this simulation run of the two-stream instability with hot ions [Run E]. On the other hand, since the temperature of ions are much smaller than that of thermalized electrons ($T_i/T_e \simeq 0.01$), the Landau damping do not occur in the simulation run with cold ions [Run D]. In this case, ion acoustic waves are excited without damping, then electrostatic potentials decay to ion acoustic waves.

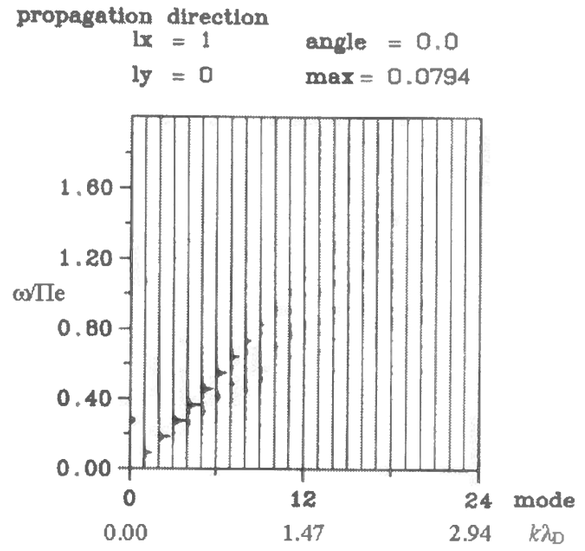

Figure 5.11: The ω-k diagrams of E_x in the simulation run of the two-stream instability with hot ions [Run E in Table 5.1].

In the right column of Figure 5.10, where the velocity distribution function of electrons are presented, we can see a flat high-energy tail in the distribution function, as shown in the simulation run of the two-stream instability neglecting ion dynamics [Run A]. In that simulation without ion dynamics, the velocity distribution function of electrons is almost symmetry, on the other hand, the velocity distribution function of electrons is asymmetrically diffused in this simulation including ion dynamics [Run E]. This asymmetry is due to the diffusion by kinetic motion of ions. Since ions have much larger mass than electrons have, $m_i/m_e = 100$ in this simulation study, kinetic energy of ions are much larger than that of electrons, and electrons are easily diffused by kinetic motion of ions.

Bump-on-tail instability Next, we performed two simulation runs of the electron bump-on-tail instability with cold and hot ions, respectively. In these simulations, the temperature of cold ions is 1/100 as large as that of the background electrons ($T_i/T_e = 0.01$), while the temperature of hot ions is 4 times of the background electrons ($T_i/T_e = 4$). Simulation parameters in these runs are listed in Run F and G of Table 5.1, respectively.

Figure 5.12 shows x-v_x phase diagrams and corresponding velocity distribution functions of electrons at different times in simulation of the bump-on-tail instability with cold ions [Run F]. In the left column of this figure, we can find the formation of ESW in spite of the existence of cold ions. Many potentials are excited by the initial bump-on-tail instability, they grow and

coalesce with each other, forming stable potentials in the final state. This time evolution of electrostatic potentials is almost the same with that in the simulation run without ion dynamics [Run C]. There cannot be found any significant difference due to ion dynamics.

Since nonlinear wave-particle interaction occurs only with the beam electrons in the bump-on-tail instability, ESW are drifting with a velocity which is almost the same with that of the electron beam ($v_{\rm ESW} \simeq v_{\rm d}$). According to the linear dispersion relations analyzed in Section 3.2, on the other hand, the ion acoustic waves are excited around $k\lambda_{\rm D} \simeq 1.0$. Since their frequencies are almost equal to the ion plasma frequency $\Pi_{\rm e}$, as shown in Figure 5.9, the phase velocity of the ion acoustic waves is about 0.2, so that $v_{\phi \rm IAW} \simeq 0.1 \times v_{\rm d}$. Therefore, the difference between these velocities, $v_{\rm ESW}$ and $v_{\phi \rm IAW}$, is much larger than the velocity range of the vortices of the ESW potentials. It is impossible to make nonlinear wave-particle interaction between the ESW potentials and the ion acoustic waves. This is the reason why the electrostatic potentials are not lead to decay to ion acoustic waves, even with cold ions. While in the two-stream instability, since the vortices of ESW potentials are very large, these ESW potentials interact with and decay to the ion acoustic waves.

In the right column of Figure 5.12, though the velocity distribution functions of electrons are a little diffused by the kinetic motions of ions, they are not essentially different from those in the simulation run without ion dynamics [Run C]. This indicates that the background electrons are a little diffused by ion acoustic waves, while the beam electrons which support ESW are scarcely affected. Therefore, ESW can exist stably in spite of the existence of cold ions.

Figure 5.13(a) presents the ω-k diagram in this simulation run. There exist ion acoustic waves as well as Langmuir waves and ESW. In comparison with the two-stream instability with cold ions [Run D], ion acoustic waves are too weak to find in this ω-k diagram. It is just an amplitude of linear waves. This is because the decay of the electrostatic potentials to the ion acoustic waves is not occurred in this simulation. Dispersions of other waves are almost the same with those in the simulation run of the bump-on-tail instability without ion dynamics [Run C]. In this simulation run of the bump-on-tail instability with cold ions, ESW can exist stably with ion acoustic waves.

We performed another simulation run of the electron bump-on-tail instability with hot ions, as listed in Run G of Table 5.1. In this simulation run, we can also find the formation of ESW. Since the temperature of ions is higher than that of electrons, ion acoustic waves are damped due to the Landau damping. There is no significant difference due to the ion dynamics in the ω-k diagram presented in Figure 5.13(b).

Dependence on drift velocity of ions

As a next step, we investigated effects of drift velocities of ions on the formation process of ESW from electron beam instabilities. We performed a series of simulation runs of the two-stream instability and the bump-on-tail instability with different drift velocities of ions. Since we confirmed that the temperature of ions must be hot for ESW formation from the two-stream instability in the previous part of this subsection, we assume hot ions in simulations of the two-stream instability. While in the bump-on-tail instability, we performed two sequences of simulation runs with cold and hot ions, respectively.

Two-stream instability First, we performed simulation runs of the electron two-stream instability varying drift velocities of ions, $v_{\rm di} = 0.0 \sim 0.5 \times v_{\rm d}$. Among these simulation runs,

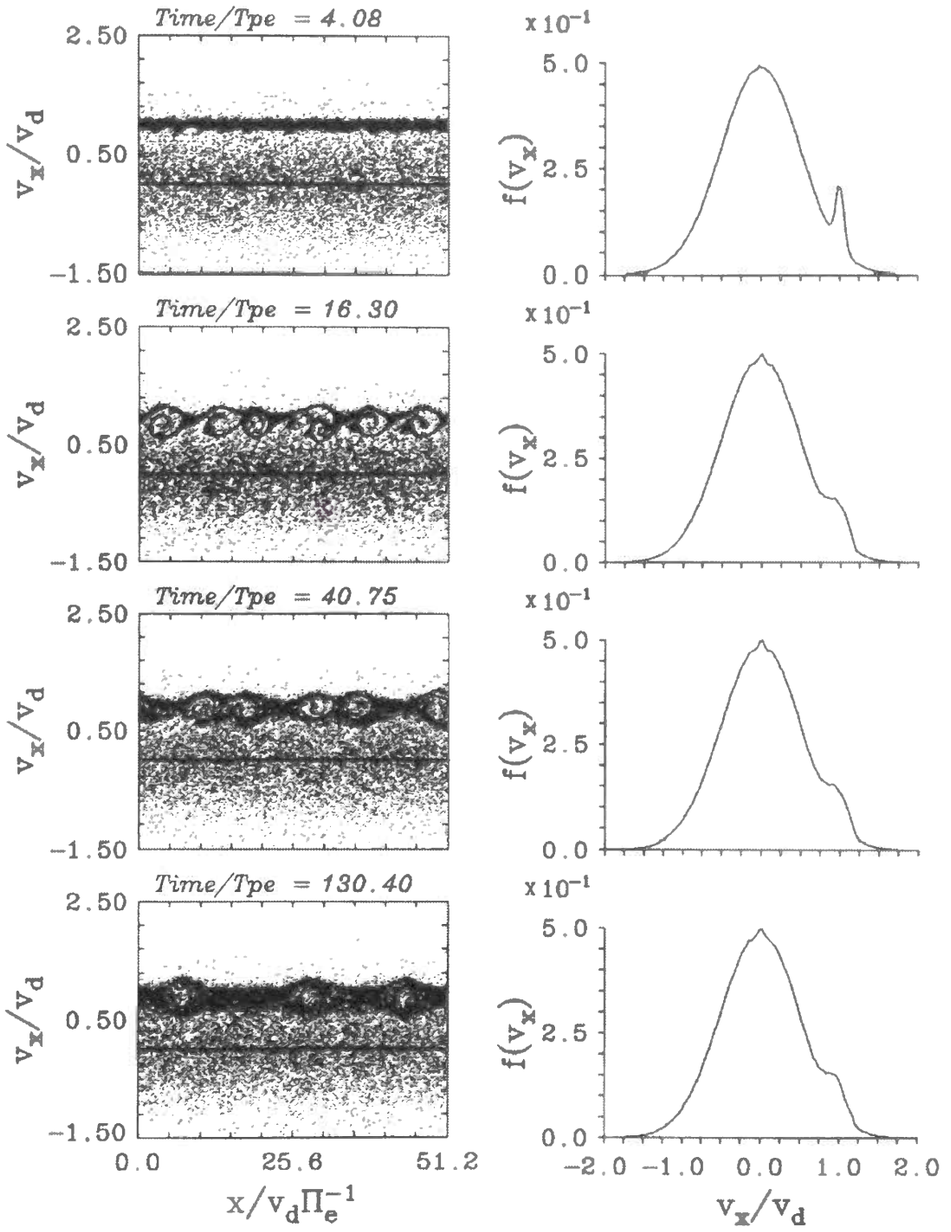

Figure 5.12: Time evolution of the bump-on-tail instability with cold background ions [Run F in Table 5.1]. Left and right columns present the x-v_x phase diagrams and the corresponding electron velocity distribution functions $f(v_x)$ at t = 4, 16, 40, 130$\times T_{\rm pe}$, respectively.

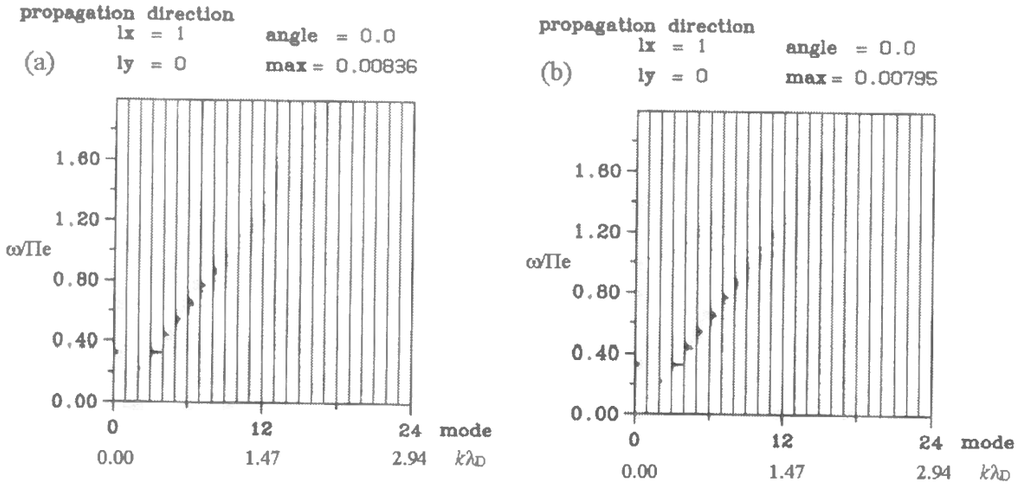

Figure 5.13: The ω-k diagrams of E_x in the simulation run of the bump-on-tail instability with ion dynamics. Left and right panels show the ω-k diagrams of (a):the bump-on-tail instability with cold ions (b):the bump-on-tail instability with hot ions, respectively [Runs F and G in Table 5.1].

we present and explain the results of the simulation run of $v_{\rm di} = 0.5 \times v_{\rm d}$. Parameters used in this simulation are listed in Run H of Table 5.1. In this simulation, the drift velocity of ions is nearly equal to the drift velocity of ESW formed from the two-stream instability ($v_{\rm di} \simeq v_{\rm ESW}$).

Figure 5.14 presents x-v_x phase diagrams and corresponding velocity distribution functions of electrons in this simulation. In the left column, we can find that ESW are once formed, then they are diffused in time.

Since the drift velocity of ions is almost same with that of ESW in this simulation, ions are drifting with ESW, and ions are trapped between ESW potentials. As confirmed in the previous section, these ESW potentials are formed through nonlinear evolution of electrons, and they are balanced with electrons. In this simulation with ion dynamics, however, since ion has much larger mass than electron, the kinetic motion of ions are not negligible for ESW potentials which are balancing with electrons. In addition, since ions have relatively large temperature to suppress ion acoustic waves, the kinetic motion of ions are larger. Therefore, the kinetic motion of these trapped ions diffuse ESW potentials and disturb the balance between ESW potentials and electrons. Due to this diffusion process, ESW are diffused and electrons are thermalized in time. While in the simulation run with no drift velocity of ions ($v_{\rm di} = 0$) [Run E], ions have a large relative drift velocity against ESW, and they have sufficiently large kinetic energy against energy of ESW potentials. Therefore, they are not trapped in BGK potentials. ESW are not diffused by kinetic motion of ions, and exist stably for a long time.

This simulation result indicates that the drift velocity of ions is one of the critical parameters for the ESW formation from the two-stream instability. In other words, it is necessary for ESW formation from the two-stream instability that ESW have a sufficient relative velocity against ions.

In the left column of Figure 5.14, though ESW are almost diffused, we can find small two

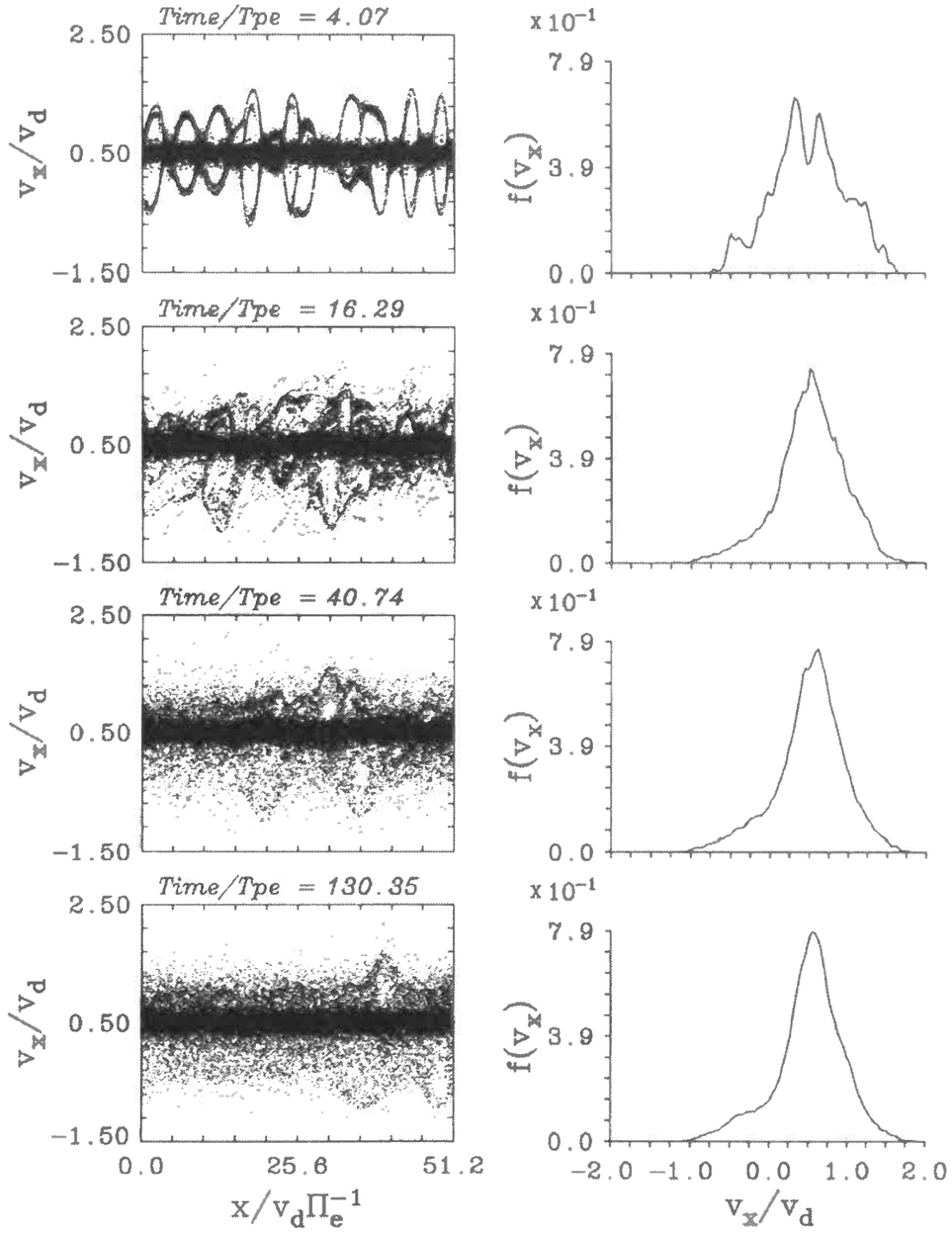

Figure 5.14: Time evolution of the bump-on-tail instability with drifting cold ions [Run H in Table 5.1]. The drift velocity of the ions is almost equal to that of ESW. Left and right columns present the x-v_x phase diagrams and the corresponding electron velocity distribution functions $f(v_x)$ at t = 4, 16, 40, 130$\times T_{\rm pe}$, respectively.

potentials are still remain after the diffusion due to the kinetic motion of ions. Since the ESW potentials formed from the two-stream instability are very large in velocity space, potential components with large relative velocities against ions are not diffused by the ion dynamics and exist stably.

This diffusion process due to the kinetic motions of ions also affects the drift velocity of ESW. During the formation process of ESW, electrostatic potentials coalesce with each other, forming stable potentials of ESW. During this coalescence of potentials, ions disturb potentials drifting with almost the same velocity of themselves. ESW are formed by the rest potentials which have large relative velocities against ions. ESW formed by such potentials come to have large velocities against ions.

Bump-on-tail instability Next, we performed simulation runs of the electron bump-on-tail instability varying drift velocities of ions. We performed two sequences of simulation runs for different temperatures of ions, with cold and hot ions. The ion drift velocity is assumed as $v_{\rm di} = 0.0 \sim 1.0 \times v_{\rm d}$. As mentioned in the previous subsection, ESW have a drift velocity which is a little decreased from that of the initial electron beam $v_{\rm ESW} \simeq v_{\rm d}$ in the bump-on-tail instability. Therefore, ions are drifting with ESW in the case of $v_{\rm di} = 0.75 \times v_{\rm d}$. In this thesis, we present the simulation results of this case, with cold and hot ions, respectively.

At first, we present simulation results of the electron bump-on-tail instability with cold ions which are drifting with a velocity of $v_{\rm di} = 0.75 \times v_{\rm d}$. Simulation parameters are listed in Run I of Table 5.1. The x-v_x phase diagrams and the velocity distribution functions of electrons at different times in this simulation are presented in Figure 5.15.

In the left column of this figure, we can find that ESW are diffused and electrons are thermalized in time. In the final state, almost all the ESW are diffused, and there exists no significant potential structure. The electron velocity distribution functions are asymmetry diffused, forming a plateau, as shown in the right column of this figure. These are very similar to those in Run D. This diffusion is due to ion acoustic waves whose phase velocity is nearly equal to the drift velocity of ESW.

Contrary to the simulation Run F, since the drift velocity of ESW and the phase velocity of ion acoustic waves are almost equal ($v_{\rm ESW} \simeq v_{\phi \rm IAW}$) in this simulation, the nonlinear wave-particle interaction occurs between the electrons which are supporting ESW and ion acoustic waves. The energy of ESW potentials decay into ion acoustic waves, and then ESW are diffused in time.

Next, we present simulation results of the electron bump-on-tail instability with hot ions which are drifting with a velocity of $v_{\rm di} = 0.75 \times v_{\rm d}$. Simulation parameters are listed in Run J of Table 5.1. The x-v_x phase diagrams and the velocity distribution functions of electrons at different times in this simulation are presented in Figure 5.16.

In the left column, we can also find that ESW are diffused and electrons are thermalized in time, and there exists no significant potential structure in the final state. Though this simulation result is similar to that of the previous simulation [Run I], some differences can be seen in the velocity distribution functions of electrons presented in the right column.

In the previous simulation [Run I], both beam and background electrons are diffused by ion acoustic waves and make a relatively wide plateau in the velocity distribution function, as shown in the right column of Figure 5.15. While in this simulation [Run J], only the bump of the electron beam is diffused, and the velocity distribution functions are not very different

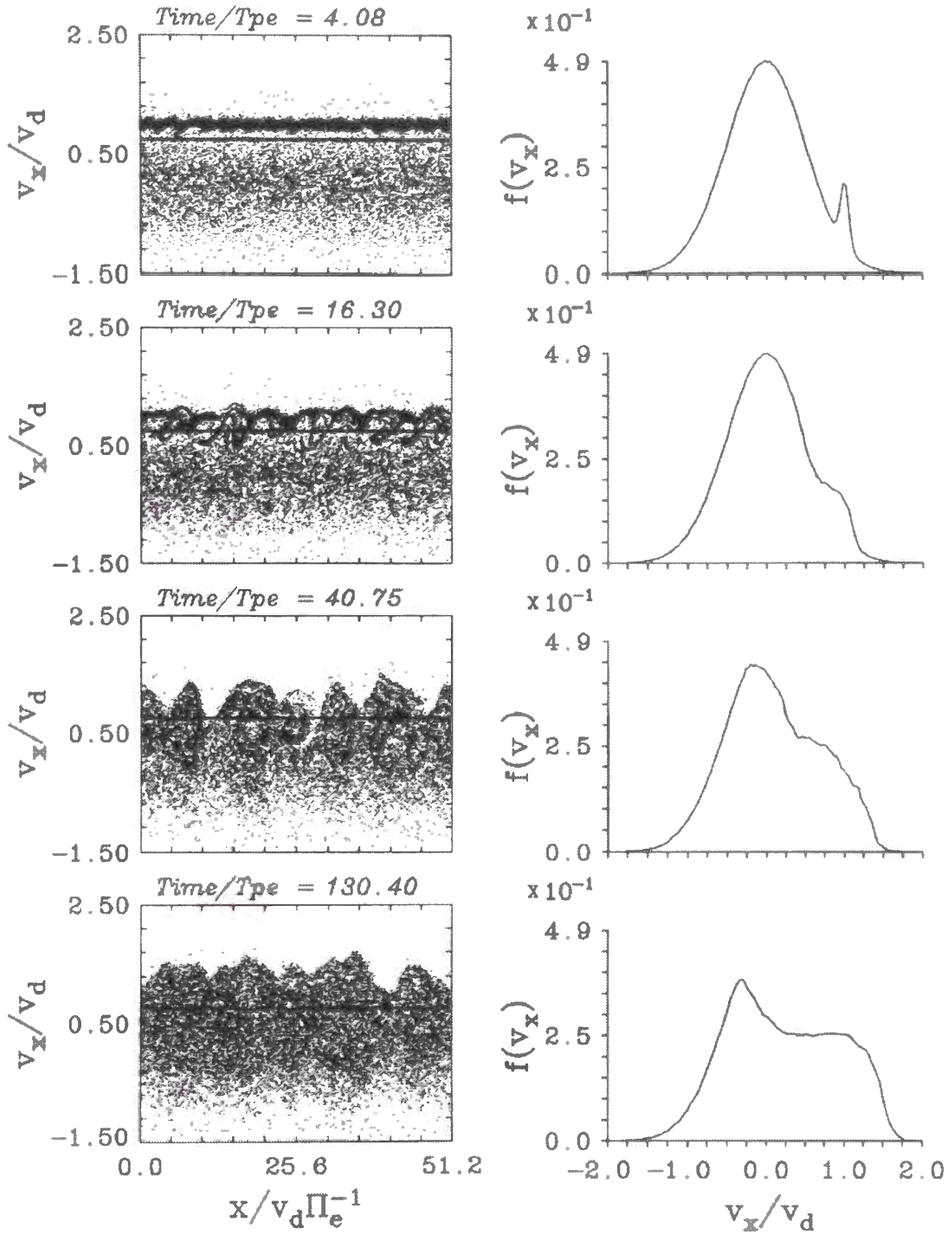

Figure 5.15: Time evolution of the bump-on-tail instability with drifting cold ions [Run I in Table 5.1]. The drift velocity of the ions is almost equal to that of ESW. Left and right columns present the x-v_x phase diagrams and the corresponding electron velocity distribution functions $f(v_x)$ at t = 4, 16, 40, 130$\times T_{\rm pe}$, respectively.

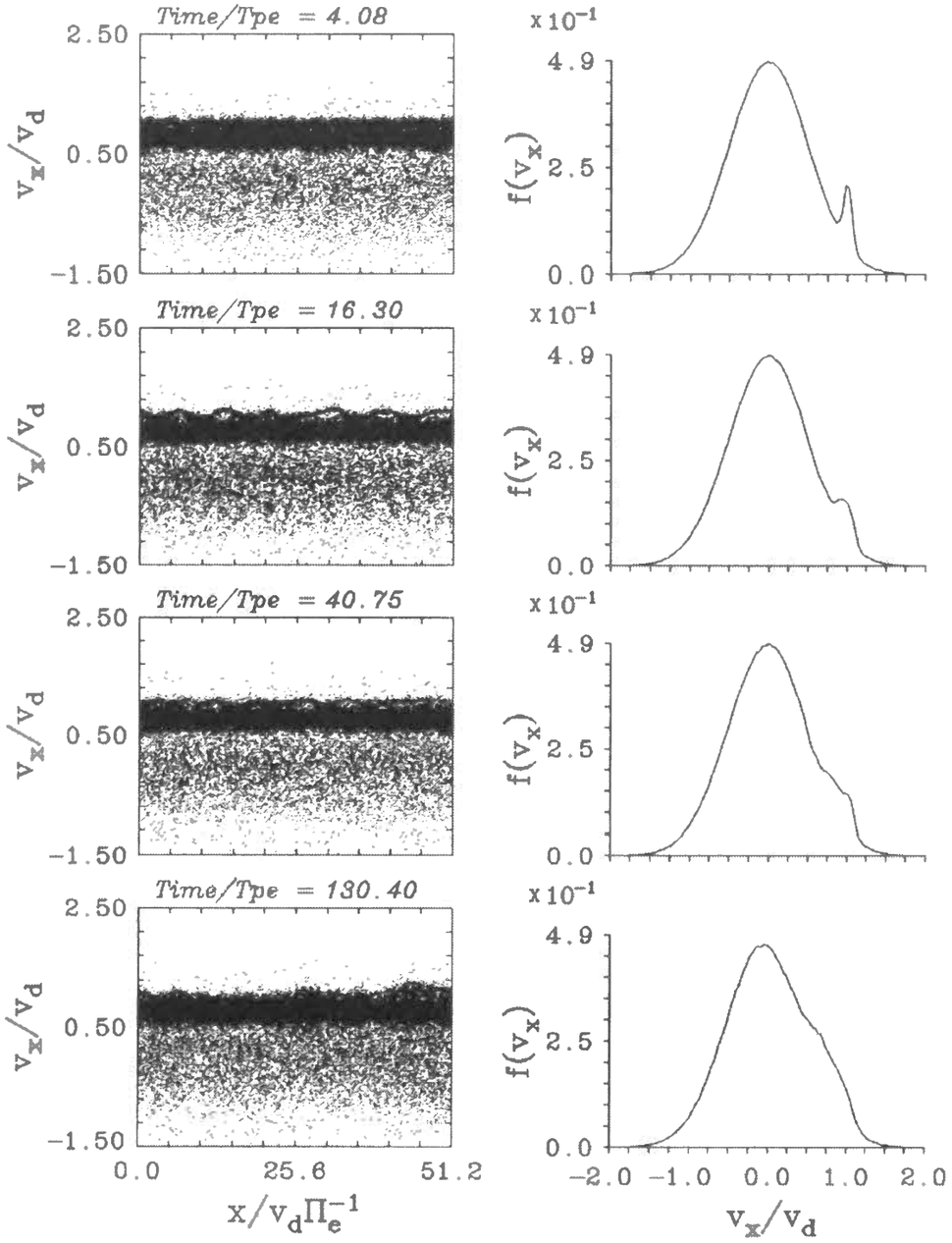

Figure 5.16: Time evolution of the bump-on-tail instability with drifting cold ions [Run J in Table 5.1]. The drift velocity of the ions is almost equal to that of ESW. Left and right columns present the x-v_x phase diagrams and the corresponding electron velocity distribution functions $f(v_x)$ at t = 4, 16, 40, 130×T_{pe}, respectively.

from that in the simulation of the bump-on-tail instability without ion dynamics [Run C]. This diffusion is caused by the kinetic motion of ions, which is also found in Figure 5.14, presenting the results of Run H. In this simulation [Run J], since the drift velocity of ESW are almost equal to that of ion flow ($v_{ESW} \simeq v_{di}$), the kinetic motion of ions affect and diffuse the beam electrons and ESW potentials formed by these electrons.

The results of these two simulation runs indicate that the ion drift velocity is one of the critical parameters for the formation of ESW from the bump-on-tail instability with both cold and hot ions. In other words, it is necessary for the formation of ESW from the bump-on-tail instability that ESW have a sufficient relative velocity against ions irrespective of ion temperature.

5.2 Summary and discussion

In this one-dimensional simulation study, we confirmed the formation of ESW from certain types of electron beam instabilities, and clarified several necessary conditions to form stable ESW in the one-dimensional system. According to these simulation results and satellite observations, we can estimate possible electron beam instabilities which generate ESW in the PSBL region and in the auroral region.

5.2.1 Summary of one-dimensional simulations

In one-dimensional computer simulations, we confirmed the formation of BGK potentials through nonlinear evolutions of electron beam instabilities. These BGK potentials are considered as electrostatic potentials of ESW. In this one-dimensional simulation study, we performed electrostatic particle simulations of three typical electron beam instabilities, the two-stream instability, the weak-beam instability and the bump-on-tail instability. Among these instabilities, we confirmed that ESW are formed from the two-stream instability and the bump-on-tail instability, and they are very stable in the one-dimensional simulation system.

There are some differences between ESW generated from the two-stream instability and those generated from the bump-on-tail instability. One of these difference is in amplitudes of ESW electric fields, as shown in Figure 5.5. Since the two-stream instability is very strong instability, this instability grows to interact with almost all electrons. Therefore, ESW generated from the two-stream instability have very large electric fields. While ESW generated from the bump-on-tail instability have only small electric fields. This is because the growth rate of the bump-on-tail instability is not so large, and this instability does not grow to interact with many electrons. Since the positive gradient is diffused in instance, forming a plateau in the velocity distribution functions of electrons, the bump-on-tail instability interact with only beam electrons, and stops growing without interacting with background electrons. Therefore, ESW generated from the bump-on-tail instability have only a small electric field.

Another difference is in amplitudes of vortices in velocity phase space, which is clearly shown in x-v_x phase diagrams in each simulation, Figures 5.2 and 5.4. These vortices are formed by electrons trapped in ESW potentials. Since the amplitude of a vortex is related to that of the electric field of the corresponding potential, it is natural that the amplitudes of vortices formed from the two-stream instability is much larger than those formed from the bump-on-tail instability. This difference, however, critically affects the stability of ESW which mainly

depends on several parameters of ions.

Parametric dependence

As a next step, we performed simulation runs of the two-stream instability and the bump-on-tail instability including ion dynamics, and estimated effects of several parameters of ions on the formation and the stability of ESW.

Two-stream instability In simulation runs of the electron two-stream instability, the dynamics of ions plays an important role on the formation and the stability of ESW. One of these effects of ion dynamics is that the ion temperature affects critically the formation of ESW. This is because, the electrostatic potentials decay to ion acoustic waves, when the temperature of ions is much smaller than that of electrons ($T_\mathrm{i}/T_\mathrm{e} \ll 1$). In this case, the two-stream instability excite clear electrostatic potentials in the initial state. These potentials, however, decay to ion acoustic waves, then they diffused and thermalized before they coalesce with each other forming stable ESW. While in the case when the temperature of ions are larger than that of electrons ($T_i/T_e \geq 1$), ion acoustic waves are dumped due to the Landau dumping. Electrostatic potential excited by the initial two-stream instability coalesce with each other forming stable ESW. Another effect of ion dynamics is that the drift velocity of ions affects the stability of ESW. In the case of $v_\mathrm{di} \simeq v_\mathrm{ESW}$, ions are trapped in potential structure formed by electrons. Since a fluctuation of an ion is very larger than that of an electron, the kinetic motion of the trapped ions easily diffuse electrostatic potentials formed by the initial electron two-stream instability. Stable ESW cannot be formed in this case of $v_\mathrm{di} \simeq v_\mathrm{ESW}$. The necessary conditions for the formation of ESW from the two-stream instability in one-dimensional system are listed as follows:

- electron beam density : $R \geq 0.3$
- ion temperature : $T_\mathrm{i} \geq T_\mathrm{e}$
- ion drift velocity : $|v_\mathrm{di} - v_\mathrm{ESW}| \gg 0$

where T_e is the temperature of electrons being thermalized by the initial two-stream instability.

Bump-on-tail instability In simulation runs of the electron bump-on-tail instability, on the other hand, the dynamics of ions have little effects on the formation as well as the stability of ESW. It is noted that ESW formed from the bump-on-tail instability can exist stably even in the existence of ion acoustic waves, when ESW have a sufficiently large relative velocity against the ions. Since ESW have a much smaller amplitude, and they are drifting with a large relative velocity against the phase velocity of ion acoustic waves, the ion acoustic waves cannot interact with the electrons which is supporting ESW structure. The ion acoustic waves have only a small amplitude, and the wave dispersion remains linear characteristics. The only necessary condition for the formation of ESW from the bump-on-tail instability in the one-dimensional system is given as follows:

- ion drift velocity : $|v_\mathrm{di} - v_\mathrm{ESW}| \gg 0$

These results of the one-dimensional simulations including ion dynamics indicate that ESW generated from the bump-on-tail instability are more stable than those generated from the two-stream instability. Though ESW generated from the bump-on-tail instability have only small electric fields, they are very stable even in the existence of ion acoustic waves.

Enhanced thermal fluctuations

As stated in Section 4.2, thermal fluctuations are numerically enhanced in particle simulations. In the one-dimensional simulations of the present study, effects of this enhanced thermal fluctuations are found as numerical thermalization and diffusion of stable BGK potentials by kinetic motion of superparticles. We performed simulation runs with ion dynamics in Section 5.1.3, and often observed that BGK potentials are diffused by the kinetic motion of ions, as shown in Runs E, G, H and J. These diffusion are thought to occur in much longer time scale in the real space plasma where the thermal fluctuations are much suppressed.

5.2.2 Comparison with satellite observations

ESW observed in the PSBL region According to the Geotail observations presented in Section 2.1, one of the characteristics of ESW observed in the Earth's PSBL region is the small amplitude of their electric fields. This small electric field indicates that ESW are generated by very weak electron beam instabilities in that region. The one-dimensional simulations demonstrated that the very weak electron beam (about 3% density in the present study) can excite stable ESW in the case of the bump-on-tail instability. In the electron velocity distribution function of the bump-on-tail instability, warm background electrons are assumed, which is consistent with the plasma signature in the PSBL region. The one-dimensional simulations with ion dynamics confirmed that ESW formed by the bump-on-tail instability are very stable and hard to affected by the ion dynamics. These ESW exist stably for a long time. This is also consistent with our assumption that ESW are very stable and they are observed almost always in the PSBL region. Judging from these results of the one-dimensional particle simulations and the Geotail observations, we can conclude that the electron bump-on-tail instability is the most suitable instability as the generation mechanism of ESW in the PSBL region [*Matsumoto et al.*, 1999].

In the present study, we assumed an electron beam with a 3% density as the weak electron beam. This 3% density beam, however, still too strong in comparison with the electron beam fluxes observed in the PSBL region. According to the Geotail/LEP observations [*Omura et al.*, 1999a], the observed electron flows corresponding to ESW have only 0.1% density or smaller. To execute quantitative comparison between the simulation results and the observations, we must perform simulations with much weaker electron beams. Unfortunately, the small amplitude ESW excited by a weak electron beam instability, such as the bump-on-tail instability, are tend to be diffused by the enhanced thermal fluctuations in particle simulations. It it very difficult to perform accurate particle simulations with such a weak electron beam. This is one of our future works of the present study.

ESW observed in the auroral region Contrary to the PSBL ESW observed by the Geotail spacecraft, the electric fields of ESW in the auroral region have a very large amplitude, as presented in Section 2.2. These strong ESW correspond to solitary structure of large electrostatic potentials which affect almost all the electrons. The one-dimensional simulations demonstrated that such large potentials are formed by the electron two-stream instability, trapping or

interacting with almost all the electrons.

According to the observations of the FAST and the Polar satellites, ESW have two-dimensional structures in the auroral region. It is reported by the FAST observations that the scale length of ESW in the direction perpendicular to the ambient magnetic field is the order of the local ion gyroradius [*Ergun et al.*, 1998], suggesting effects of the ion dynamics. In the one-dimensional simulations, ESW excited by the two-stream instability have very large amplitudes, they interact with ions and tend to be affected by ion dynamics. This is also consistent with the above observational results. Therefore, we can conclude that the electron two-stream instability is the most suitable instability as the generation mechanism of ESW in the auroral region.

In the one-dimensional simulations, of course, we cannot confirm spatial structures of ESW, which is the most significant difference between ESW in the PSBL region and those in the auroral region. We will investigate the spatial structures of ESW via two-dimensional computer simulations in the next chapter.

Chapter 6

Two-dimensional Simulation Study of ESW

6.1 Introduction

In the previous chapter, we performed the one-dimensional computer simulations of three electron beam instabilities as possible generation models of ESW, the two-stream instability, the weak-beam instability and the bump-on-tail instability. In this one-dimensional simulation study, we mainly investigated parametric dependence of the formation and the stability of ESW. We performed simulation runs of these electron beam instabilities for different plasma parameters, and estimated parametric dependence on these parameters, especially parameters of ions, the temperature $T_{\rm i}$ and the drift velocity $v_{\rm di}$.

As stated in Section 2.3, we deal with two types of ESW potentials with different spatial structures in the present study. In the one-dimensional simulations taken along the ambient magnetic field, one-dimensional structures which are uniform in the direction perpendicular to the simulation system are assumed a priori, and one cannot study spatial structures of ESW and their formation mechanism in the direction perpendicular to the simulation system. In this chapter, we performed a series of electrostatic particle simulations in the two-dimensional system.

The linear dispersion analysis in Section 3.2 demonstrated that in all the electron beam instabilities studied in this thesis, the most unstable waves with the maximum growth rates are beam-mode waves propagating in the direction parallel to the ambient magnetic field. In one-dimensional systems taken along the magnetic fields, since waves cannot propagate except along the simulation system, waves are only excited propagating in the direction parallel to the ambient magnetic field, which are the beam-mode waves with the maximum growth rates. Therefore, we can observe the detailed nonlinear evolutions of these most unstable beam-mode waves in one-dimensional simulations, and confirmed the formations of stable BGK potentials. While in two-dimensional simulations, oblique mode waves will be excited. According to the linear dispersion analysis, growth rates of oblique mode waves are different due to the initial electron beam instabilities, and they depend on the magnitudes of the static magnetic fields and the propagation angles to the magnetic fields. The amplitudes or the growth rates of these oblique mode waves are expected to affect the spatial structures of ESW in the two-dimensional system. Such effects of oblique mode waves also cannot be observed in one-dimensional simulations.

6.1.1 Spatial structures of ESW

As mentioned in Chapter 2, there are two types of ESW reported by satellite observations. One is observed in the magnetotail PSBL region by the Geotail spacecraft. This type of ESW has

the one-dimensional spatial structure, coherent in the direction perpendicular to the ambient magnetic field, and its electric fields is very small, about a few hundreds μV/m or smaller. This one-dimensional structure of ESW corresponds to one-dimensional electrostatic potential uniform in the perpendicular direction, as shown in Figure 2.8(a). The other is observed in the auroral region as reported by the FAST and the Polar satellites. These ESW have large amplitudes (even several V/m), and their spatial structure is two-dimensional, corresponding to two-dimensional potentials as shown in Figure 2.8(b).

6.1.2 Plasma parameters in simulation study

In the previous chapter, the one-dimensional computer simulations demonstrated that ESW can be generated by two types of electron beam instabilities, the two-stream instability and the bump-on-tail instability. We compared results of the one-dimensional simulations and observations by the Geotail and other spacecrafts, and concluded that among these three electron beam instabilities, the bump-on-tail instability is the most suitable instability as the generation model of ESW in the PSBL region, and the two-stream instability is the most suitable instability as the generation model of ESW in the auroral region. On the basis of these conclusions, we performed a series of two-dimensional electrostatic particle simulations.

In the following Section 6.2, we studied the formation mechanism of ESW in the PSBL region via two-dimensional electrostatic particle simulations. On the basis of the one-dimensional computer simulation results, we performed a series of two-dimensional simulations of the bump-on-tail instability as the possible generation model of ESW in this region. Since the one-dimensional simulation study in the previous chapter also demonstrated that ESW formed by the bump-on-tail instability are not critically affected by ion dynamics, we neglected ion dynamics in these two-dimensional simulations. In this simulation study, we studied time evolution of spatial structures of ESW potentials in the two-dimensional system. In addition, we have a new simulation parameter in the two-dimensional system, i.e., the magnitude of the ambient magnetic field B_0, which has no effect in the one-dimensional system taken along the magnetic field. In these simulations, we varied only this parameter, the magnitude of the ambient magnetic field, and investigated its effects on the formation process and the stability of ESW in the two-dimensional system.

In Section 6.3, we studied the formation mechanism of ESW and its dependence on several plasma parameters in the auroral region via two-dimensional electrostatic particle simulations. We performed two-dimensional simulations of the two-stream instabilities on the basis of the one-dimensional computer simulation results. At first, we performed a series of two-dimensional simulations of the two-stream instability without ion dynamics. In this series of simulations, we varied several parameters of electrons and investigated time evolutions of the spatial structures of ESW potentials and their dependence on varied parameters of electrons. Next, we performed two-dimensional simulations of the electron two-stream instabilities with ion dynamics. The one-dimensional simulations demonstrated that the two-stream instability excite large electrostatic potentials and they interact with ions and tend to be affected by ion dynamics. Since the parametric dependence of the formation and the stability of ESW on ion dynamics are already studied via one-dimensional particle simulations in the previous chapter, we investigated effects of ion dynamics on the spatial structures of ESW, especially in the direction perpendicular to the ambient magnetic field.

Total electron plasma frequency	Π_e	=	1.0
Density ratio of electron beam	R	=	0.03
Drift velocity of electron beam	v_d	=	2.0
Thermal velocity of beam electrons	v_{t1}	=	0.1
Thermal velocity of background electrons	v_{t2}	=	1.0

Table 6.1: Common plasma parameters of electrons in all the two-dimensional simulations of the bump-on-tail instability.

6.2 Two-dimensional particle simulations of ESW in the PSBL region

6.2.1 Models and Parameters

In this section, we performed a series of two-dimensional electrostatic particle simulations of the bump-on-tail instability with different parameters [*Miyake et al.*, 1998]. In these simulations, the simulation system is taken in the x-y plane with 64×64 grid points. The ambient magnetic field is taken along the x axis and an electron beam is drifting along the magnetic field, as schematically illustrated in Figure 4.5. As mentioned above, ion dynamics is not included in this series of simulations. Ions are distributed uniformly and fixed as neutralizing particles with infinite mass in all over the simulation system. Common plasma parameters in these simulations of the bump-on-tail instability are listed in Table 6.1. By assuming $\Pi_e = 1.0$ and $v_{t2} = 1.0$, we can regard that frequencies and velocities are normalized to Π_e and v_{t2}, respectively. Lengths are also normalized to the Debye length of the background electrons λ_D $(= v_{t2}/\Pi_e)$. Since frequencies are normalized to the plasma oscillation frequency of the electrons Π_e, times are scaled by the plasma oscillation period of the electrons $T_{pe} = 2\pi/\Pi_e$. The total simulation period in these simulation runs is $130 \times T_{pe}$.

The magnitude of the ambient magnetic field is the only parameter that is varied in this series of simulations. In our simulations, the magnitude of the magnetic field is defined by the ratio of the electron cyclotron frequency to the electron plasma frequency Ω_e/Π_e. Since the total electron plasma frequency Π_e is kept constant for all the simulation runs as shown in Table 6.1, the electron cyclotron frequency directly represents the magnitude of the ambient magnetic field. We performed three simulation runs of the electron bump-on-tail instability for different magnitudes of the ambient magnetic fields ($\Omega_e/\Pi_e = 1.0 \sim 0.2$), and investigated its effects on the formation process and the stability of ESW in the two-dimensional system.

We use 1,048,576 superparticles for the beam electrons and 33,554,432 particles for the background electrons in the present simulation runs of the bump-on-tail instability. In other words, we use 256 particles par a grid point for the beam electrons, and 8,192 particles par a grid points for the background electrons. The number of superparticles for the beam electrons is 3% of that for all the electrons. This is because we have to satisfy $m_1 = m_2$ in order to perform simulation runs correctly for a long time, where m_1 and m_2 are a mass of a superparticle for the beam and the background electrons, respectively. When $m_1 = m_2$ is not satisfied, these two electrons are treated as different species, with a different mass and charge, and energy exchange occurs in a long time evolution. Such energy exchange in same species (electron in this case) is a numerical

Run	Ω_e/Π_e	N_p
Run A	1.0	34,603,008
Run B	0.4	34,603,008
Run C	0.2	34,603,008
Run D	0.4	8,650,752

Table 6.2: Plasma parameters varied for different simulation runs of the the bump-on-tail instability.

phenomena, which never occurs in the real space plasma. Especially in the present study, we investigate the long time stability of ESW by performing particle simulations, it is important to satisfy the above condition $m_1 = m_2$. The one-dimensional simulations demonstrated that the bump-on-tail instability is relatively weak instability. Therefore, electrostatic potentials excited by the bump-on-tail instability have only small amplitudes and tend to be diffused by the enhanced thermal fluctuations (noted in Section 4.2). In the two-dimensional simulations, effects of the oblique mode waves, which also discussed in Section 4.2, also cannot be negligible. It is noted that we need to use as a large number of superparticles as possible to suppress such numerical effects due to the enhanced thermal fluctuations. This is another reason why we neglected ion dynamics in the two-dimensional simulations of the bump-on-tail instability. The two-dimensional particle simulations with ion dynamics of weak instabilities, such as the bump-on-tail instability, require much larger computer resources, memory and calculation time.

Plasma parameters varied for different simulation runs are listed in Table 6.2. N_p is the number of superparticles in the simulation system. In this table, Runs A$\sim$C correspond the series of two-dimensional simulations of the bump-on-tail instability for different magnitudes of the ambient magnetic fields. Run D is another simulation run with a less number of superparticles. We performed this simulation run to confirm the above suspected effects of the enhanced thermal fluctuations. All the simulation parameters in Run D are the same with those in Run B, except for the number of superparticles in the simulation system.

We applied the quiet start method in the two-dimensional simulations to suppress initial noise due to the distribution of particles, which is mentioned in Section 4.2. To realize this quiet start method, we use "bit reverse" scheme to make uniform distributions in the simulation systems. It is necessary for using this bit reverse scheme that the number of particles is the n-th power of 2. This is because the number of superparticles is the n-th power of 2 in two-dimensional simulations in the present study.

6.2.2 Time evolutions of ESW formation

We performed two-dimensional electrostatic particles simulations of the electron bump-on-tail instability as the possible generation model of the one-dimensional ESW observed in the Earth's PSBL region. We performed a series of simulation runs with different magnitudes of the ambient magnetic fields listed as Runs A, B and C in Table 6.2 and estimated effects of the magnitude of the ambient magnetic field.

Spatial profile of potentials The results of these simulation runs are shown in Figures 6.1$\sim$6.3. These figures represent spatial profiles of electrostatic potentials at different times,

$t = 32.59, 65.19, 130.37 \times T_{pe}$. Figures 6.1, 6.2 and 6.3 show results of Runs A, B and C, respectively. In these figures, potential values are scaled by the thermal energy density of background electrons (nmv_{t2}^2/q) and lengths are scaled by the Debye length of background electrons (v_{t2}/Π_e). The bottom panels show the final states in these simulation runs ($t = 130 \times T_{pe}$).

For the case with a strong magnetic field $\Omega_e/\Pi_e = 1.0$ [Run A], presented in Figure 6.1, sinusoidal potentials are excited through the initial bump-on-tail instability. They grow and coalesce with each other along the ambient magnetic field as observed in the previous one-dimensional simulations, forming larger potentials, and in the final state at $t = 130 \times T_{pe}$, a solitary potential is formed. This potential is almost uniform in the direction perpendicular to the ambient magnetic field. In this simulation, electrostatic potentials are not coherent in the perpendicular direction during the initial instability phase. After the coalescence process, however, we find formation of a single potential trough aligned in the perpendicular direction. This one-dimensional potential exists stably for a long time as a BGK potential.

For the case with a relatively weak magnetic field $\Omega_e/\Pi_e = 0.4$ [Run B], we can also confirm the formation of two clear ESW potentials in the final state as presented in Figure 6.2. In this case, potentials at the initial saturation phase (at the end of the wave growth) are more coherent in the perpendicular direction than those in Run A with a strong magnetic field. This difference is due to the effect of the finite Larmor radius of the background electrons, which is given by $r_L = v_{t2}/\Omega_e$. We will discuss these effects in Section 6.4.

On the other hand, for the case with a much weaker magnetic field $\Omega_e/\Pi_e = 0.2$ [Run C], we cannot find the formation of ESW potentials, as presented in Figure 6.3. In this case, the electrostatic potentials are diffused gradually, and there remains no significant potential structure in the final state. Potentials are almost coherent in the perpendicular direction even at the initial saturation phase because of the effects of the finite Larmor radius, as the same with Run B. These one-dimensional potentials, however, are diffused as time goes on. This diffusion is due to the enhanced thermal fluctuations, which is not a physical phenomena. We will mention this effect of the enhanced thermal fluctuations in Section 6.4.5.

Among these three simulations of the bump-on-tail instability with different magnitudes of the ambient magnetic fields, we can find the formation of clear potential structures in the final state of Runs A and B, simulation runs with a strong and a relatively weak magnetic fields. These potentials are uniform in the direction perpendicular to the ambient magnetic field, and look like "troughs". Such one-dimensional potentials are consistent with the one-dimensional ESW potential model in the PSBL region, as presented in Section 2.3.

Time history of energies In Figure 6.4, we show time histories of the energy densities of the electric field in the parallel direction $E_\parallel$, the perpendicular thermal energy of beam electrons $v_{t1\perp}$ and the electric field in the perpendicular direction $E_\perp$ in these simulation Runs A$\sim$C. Three lines in all the three panels correspond to Runs A, B and C, respectively. All energy densities are scaled by the thermal energy density of the background electrons nmv_{t2}^2. In Figure 6.4(a), the growth rates of $E_\parallel$ energy for all the three runs are almost same during the initial wave growth. This is consistent with the linear theory as analyzed in Section 3.2, giving the same maximum growth rate for the different magnitudes of the ambient magnetic fields. However, we can find effect of the magnitude of the ambient magnetic field on the saturation levels of $E_\parallel$ energy. The larger magnetic field gives a larger saturation level. There are two

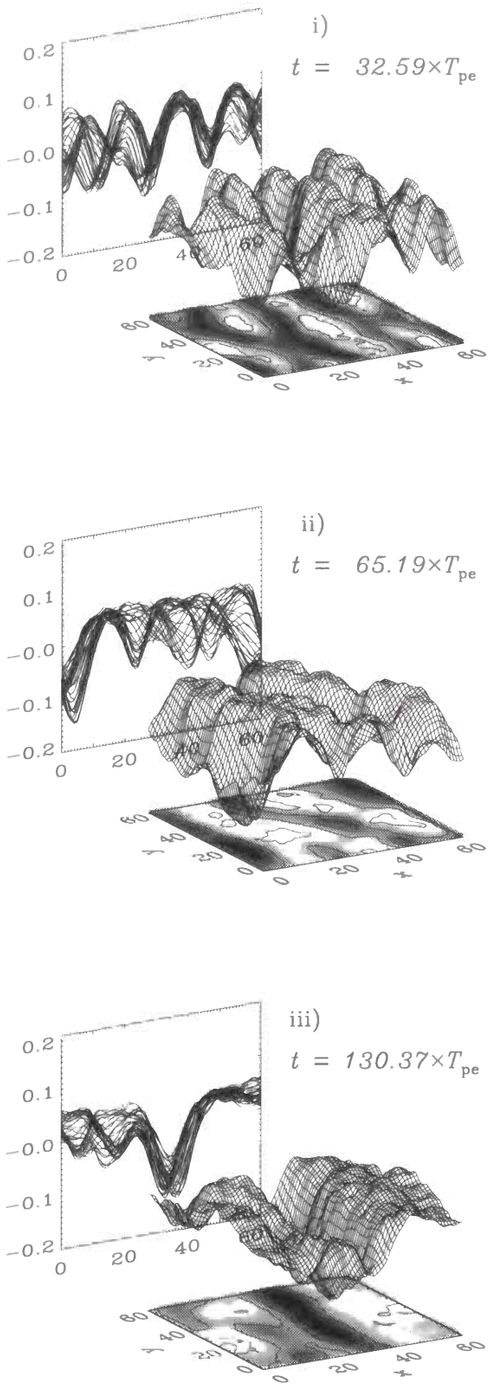

Figure 6.1: Spatial profiles of potentials at different times, $t = 32.59,\ 65.19,\ 130.37 \times T_{pe}$, in Run A of Table 6.2, simulation run with a strong magnetic field ($\Omega_e/\Pi_e = 1.0$). The ambient magnetic field is taken along the x axis.

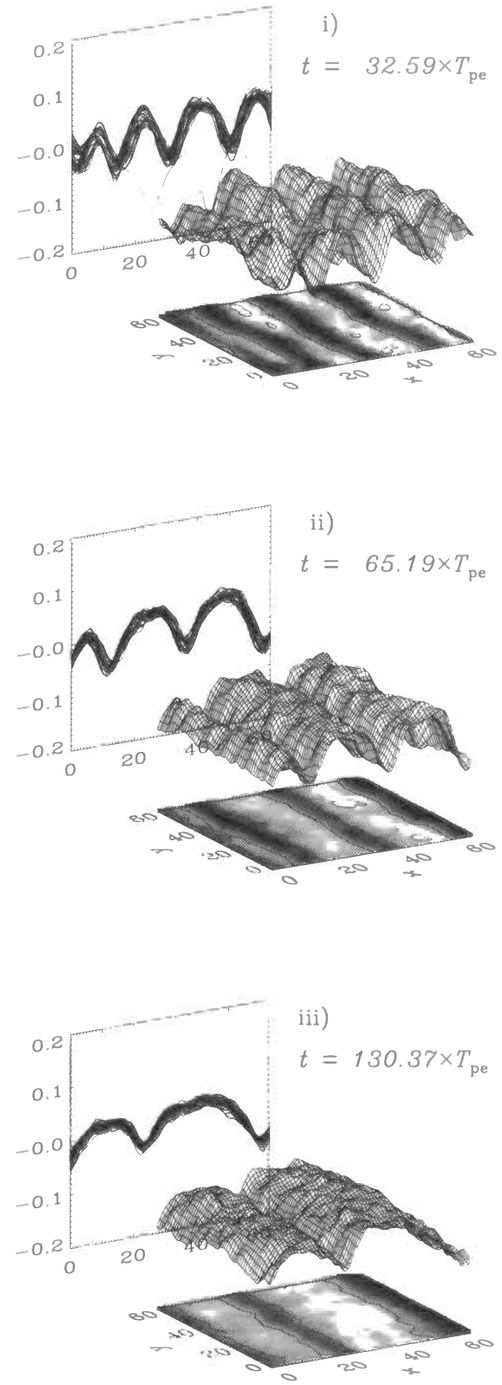

Figure 6.2: Spatial profiles of potentials at different times, $t = 32.59,\ 65.19,\ 130.37 \times T_{pe}$, in Run B of Table 6.2, simulation run with a relatively weak magnetic field ($\Omega_e/\Pi_e = 0.4$).

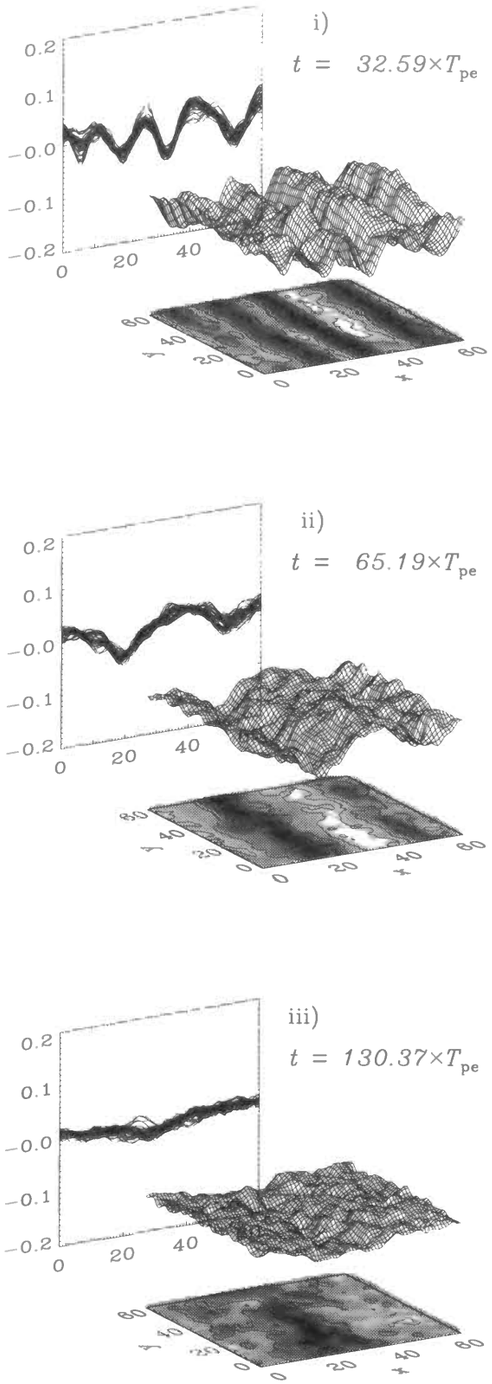

Figure 6.3: Spatial profiles of potentials at different times, $t = 32.59, 65.19, 130.37 \times T_{pe}$, in Run C of Table 6.2, simulation run with a weak magnetic field ($\Omega_e/\Pi_e = 0.2$).

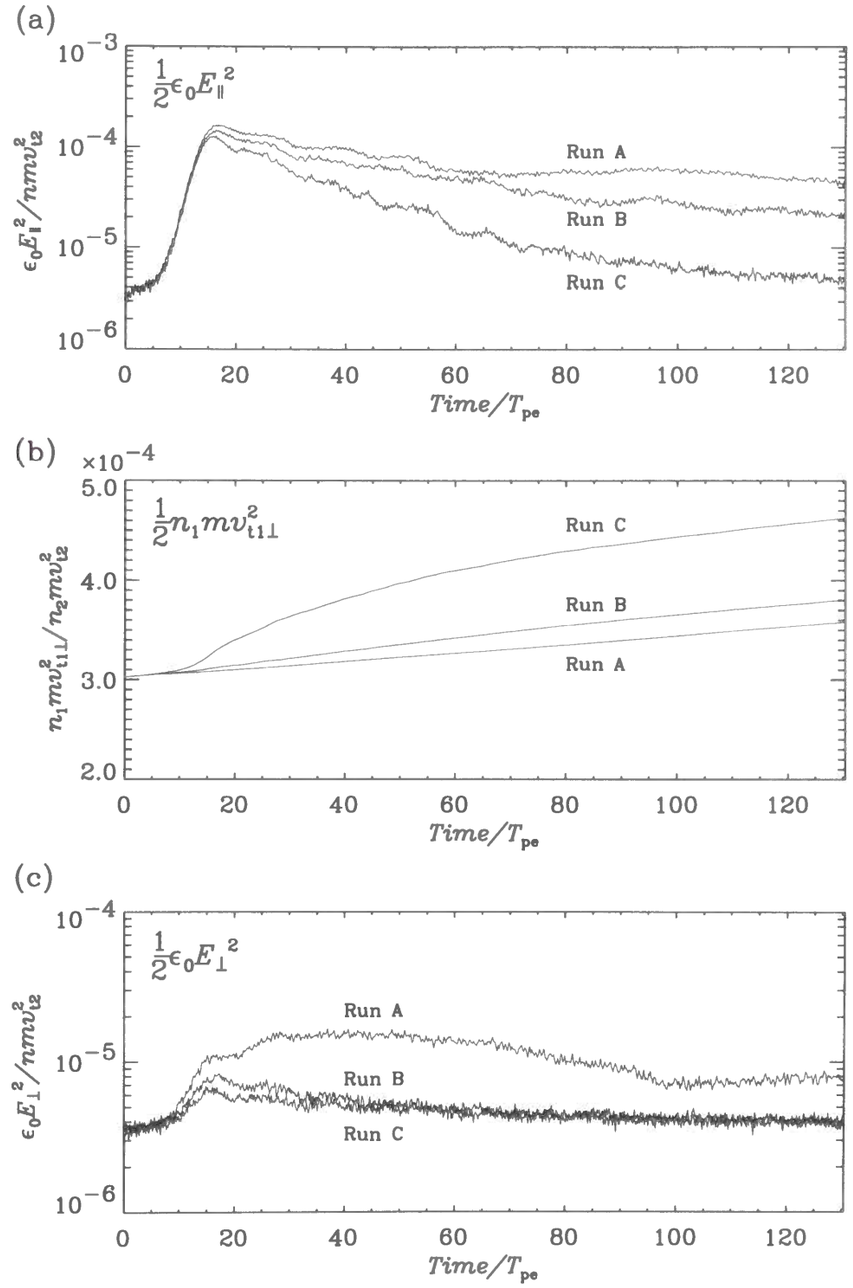

Figure 6.4: Time histories of energy densities in simulation Runs A∼C: (a):$\frac{1}{2}\epsilon_0 E_\parallel^2$, (b):$\frac{1}{2}n_1 m v_{i1\perp}^2$, and (c):$\frac{1}{2}\epsilon_0 E_\perp^2$.

possible explanations for this enhancement of the saturation level. One is that the oblique mode waves have larger growth rate in the larger magnetic field. As analyzed in Section 3.2, oblique mode waves have larger growth rates in the case with a strong magnetic field than those in the case with a weak magnetic field. In addition, the saturation periods are almost same in each run as shown in this figure. The oblique mode waves in Run A are thought to be excited up to higher level at the saturation time. Since the presented $E_{\parallel}$ energy is the summary of all the waves including oblique mode waves, the saturation level of $E_{\parallel}$ in Run A is higher than those of other runs. The other explanation is that the beam electrons forming the electrostatic potential and the resulting $E_{\parallel}$ are restricted to the one-dimensional motion along the magnetic field and that diffusion of the $E_{\parallel}$ energy is suppressed in the case of the strong magnetic field [Run A].

After the $E_{\parallel}$ energy saturation, all three lines decrease in quasi-stepwise. These quasi-stepwise changes correspond to the times when two adjoining potentials coalesce with each other. In the coalescence process, the $E_{\parallel}$ energy is transformed to the thermal energy of the electrons. In addition, after the initial wave growth phase, the $E_{\parallel}$ energy in Run C ($\Omega_e/\Pi_e = 0.2$) represents very different changes from the other two runs. The $E_{\parallel}$ energies in Run A and B ($\Omega_e/\Pi_e = 1.0$ and 0.4) reach higher peaks and stay at high values for a long time, while that in Run C reaches a lower peak, and then it gradually decreases to the thermal noise level where the beam instability started. Corresponding to the $E_{\parallel}$ energy decrease in Run C, the perpendicular thermal energy of the electron beam increases substantially as shown in Figure 6.4(b). This indicates that the beam electrons, which form the potentials trapped therein through their oscillatory motion along the magnetic field, are diffused in the perpendicular direction.

In Figure 6.4(c), the $E_{\perp}$ energy of Run A has much higher value than those of the other two runs. This indicates that there are larger perpendicular potential structures in Run A than those in the other two runs. This is also due to the electron cyclotron motion. In the present three runs with $\Omega_e/\Pi_e = 1.0$, 0.4 and 0.2, the Larmor radius of the background electrons r_L are 1.0, 2.5, and 5.0, respectively. Because the electron Larmor radius is smaller in Run A with $\Omega_e/\Pi_e = 1.0$, initially excited potentials are localized in the perpendicular direction (top panel in Figure 6.1). These localized potentials make perpendicular structures of potentials corresponding to the larger $E_{\perp}$ energy. These perpendicular structures of potentials, however, are diffused through potential striation process in the perpendicular direction. In the final state, one uniform potential trough is formed, and $E_{\perp}$ energy decrease to the thermal noise level.

Spectrum analysis In the simulation run of the bump-on-tail instability with a relatively weak magnetic field [Run B], we can find clear one-dimensional potentials are formed. We analyzed spatial and frequency spectrums in this simulation.

In Figure 6.5, we present $k_{\parallel}$-$k_{\perp}$ (k_x-k_y) diagrams of potentials at different times in Run B. These are obtained by Fourier transformation of potential structures at $t = 4.07$, 8.15, 16.30 and $32.59\times T_{pe}$, respectively. The first panel (a) shows that waves are almost isotropic in the initial state. The initial bump-on-tail instability excite electrostatic potential structure along the ambient magnetic field (in the x direction). These potentials have perpendicular structures in the initial phase as shown in the panel (b). These potentials grow and coalesce with each other, forming clear one-dimensional potentials uniform in the perpendicular direction (y direction). These uniform potentials correspond to the strongest spectrum at $k_{\parallel} \sim 4$ in the last panel (d)

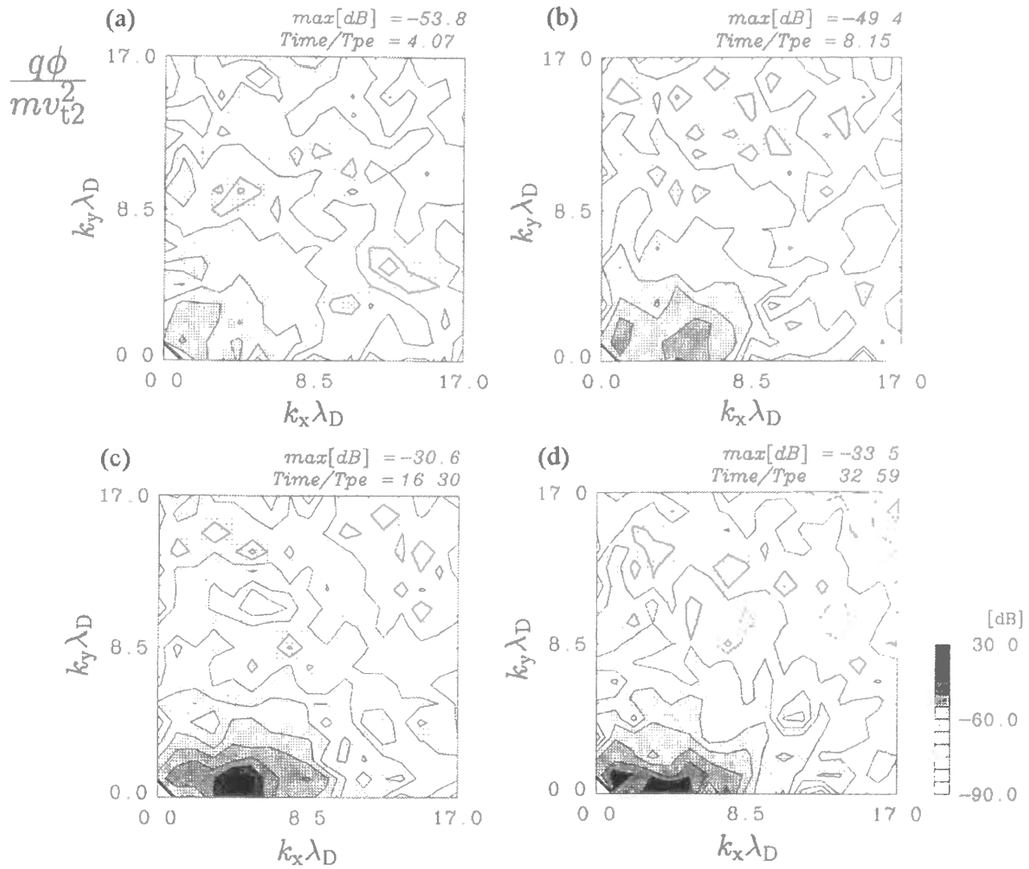

Figure 6.5: The $k_{\parallel}$-$k_{\perp}$ diagrams of potentials at different times, $t = 4.07$, 8.15, 16.30, $32.59\times T_{pe}$ in Run B ($\Omega_e/\Pi_e = 0.4$). These are obtained by Fourier transformation of potential structures at each time.

of Figure 6.5.

We also present the ω-k diagram of the $E_\parallel$ field for Run B in Figure 6.6. We find clear $E_\parallel$ spectra which correspond to the ESW potentials moving along the ambient magnetic field, shown in Figure 6.2. The solitary waves have broadband spectra in wavenumbers, which are Doppler shifted to give broadband spectra in frequency. These broadband spectra in frequency correspond to the high-frequency part of the BEN emissions.

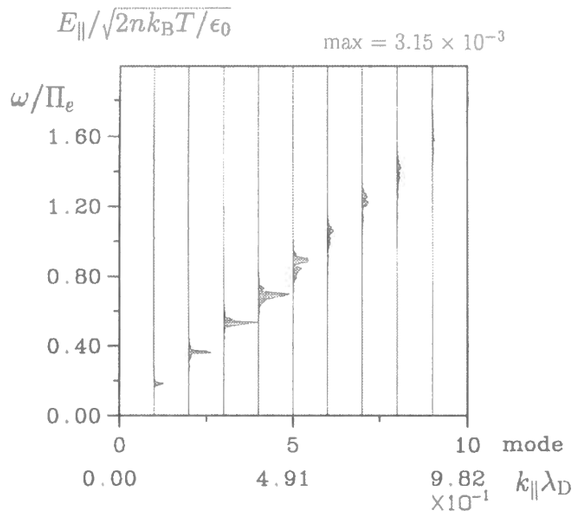

Figure 6.6: The ω-k diagram of the $E_\parallel$ field in Run B with $\Omega_e/\Pi_e = 0.4$. The spectra are obtained by Fourier transforming the $E_\parallel$ field in space and time ($t = 0.0 \sim 130.37 \times T_{pe}$). The plotted modes are parallel to the ambient magnetic field.

6.3 Two-dimensional particle simulations of ESW in the auroral region

6.3.1 Models and Parameters

According to the one-dimensional particle simulations in the previous chapter, it is most possible that ESW with very large amplitudes are excited by the strong electron two-stream instability in the auroral region. In this section, we performed a series of two-dimensional electrostatic particle simulations of the two-stream instability with different parameters as the possible generation model of ESW in the auroral region.

Parameters of the simulation system are almost the same with those in the simulations of the bump-on-tail instability, presented in the previous section, except for the grid points. In these simulations, the simulation system is taken in the x-y plane with 128×128 grid points. The ambient magnetic field is taken along the x axis and an electron beam is drifting along the magnetic field, as schematically illustrated in Figure 4.5. Common plasma parameters in these simulations of the bump-on-tail instability are listed in Table 6.3. In all these simulations,

Total electron plasma frequency	Π_e	=	1.0
Density ratio of electron beam	R	=	0.5
Drift velocity of electron beam	v_d	=	4.0
Drift velocity of ions	v_{di}	=	0.0
Thermal velocity of ions	v_{ti}	=	1.0

Table 6.3: Common plasma parameters of electrons in all the two-dimensional simulations of the two-stream instability.

frequencies are normalized to the total electron plasma frequency Π_e which is kept constant as 1.0. Times are also normalized to the plasma oscillation period of the electrons $T_{pe} = 2\pi/\Pi_e$. Velocities are scaled by the thermal velocity of the electrons in the warm electron beam instability (v_t in Runs G, H and J). Potentials also scaled by the thermal energy density of the warm electron beam ($|n_0 m_e v_t^2/q|$ in Runs G, H and J).

As mentioned in Section 6.1, we performed simulation runs of the two-stream instability both with and without ion dynamics. Ions have infinite mass ($m_i/m_e = \infty$) in simulation runs without ion dynamics, and ion to electron mass ratio is 100 ($m_i/m_e = 100$) in simulation runs with ion dynamics. At first, we performed a series of simulation runs without ion dynamics. Ions are distributed uniformly and fixed as neutralizing particles with infinite mass in all over the simulation system. We have two plasma parameters varied in these simulations, the magnitudes of the ambient magnetic fields and the temperatures of the electron beams, which are defined by the ratio of the electron cyclotron frequency and the electron plasma frequency Ω_e/Π_e and the thermal velocity of the beam electrons v_t, respectively. We performed four simulation runs of the electron two-stream instability without ion dynamics varying the above two parameters, and investigated their effects on the formation process and the spatial structures of ESW in the two-dimensional system.

Next, we performed two simulation runs with ion dynamics, and investigated effects of ions on the stability and the spatial structures of ESW. Ions are regarded as a background component without drift velocity ($v_{di} = 0.0$), and distributed uniformly in all over the simulation system. The one-dimensional simulations with ion dynamics presented in the previous chapter demonstrated that in the case that ions are very cold in comparison with electrons ($T_i/T_e \ll 1$), ion acoustic waves are excited, diffusing electrostatic potentials induced by the two-stream instability and electrons trapped therein. Finally, these ion acoustic waves diffuse solitary waves. In this series of simulations, therefore, we have to satisfy $T_i/T_e \geq 1$ after the initial electron two-stream instability saturated, to suppress the excitation of ion acoustic waves. We set up the thermal velocity of mobile ions as 1.0 ($v_{ti} = 1.0$), as shown in Table 6.3. According to the one-dimensional simulations, the thermal velocity of the electrons which are thermalized by the initial instabilities are almost equal to a half of the drift velocity of the electron beam ($v_d/2 = 2.0$). Therefore, the ratio of ion to electron temperatures after the initial instability is about 25 ($T_i/T_e \sim 25$).

Plasma parameters varied for different simulation runs are listed in Table 6.4. In this table, Runs E∼H are simulation runs without ion dynamics, and Runs I and J are simulation runs with ion dynamics. The total simulation period in all the simulation runs is 260×T_{pe}.

We use 4,194,304 superparticles for the electrons (256 particles/grid) in all the simulations,

Run	v_t	Ω_e/Π_e	m_i/m_e
Run E	0.5	0.4	—
Run F	0.5	1.0	—
Run G	1.0	0.4	—
Run H	1.0	1.0	—
Run I	0.5	1.0	100
Run J	1.0	1.0	100

Table 6.4: Plasma parameters varied for different simulation runs of the two-stream instability.

and 8,388,608 particles for the background thermal ions (512 particles/grid) in the simulations with mobile ions [Runs I and J]. This number of superparticles is smaller than that in the simulation runs of the bump-on-tail instability performed in the previous section. The one-dimensional computer simulations demonstrated that two-stream instability is very strong instability in comparison with the bump-on-tail instability. Electrostatic potentials excited by the two-stream instability have large amplitudes, and they are not so strongly affected by the enhanced thermal fluctuations. Therefore, we can decrease the number of superparticles in these simulation runs of the two-stream instability in comparison with those in the simulation runs of the bump-on-tail instability. Since we can perform the two-dimensional simulations of the two-stream instability with a smaller number of superparticles, we can deal with ion dynamics in these simulation runs [Runs I and J].

6.3.2 Time evolutions of ESW formation

We performed two-dimensional computer simulations of the electron two-stream instability as the possible generation model of the isolated two-dimensional ESW observed in the auroral region. At first, we performed simulation runs without ion dynamics [Runs A∼D]. In these runs, we have two parameters, one is thermal velocity of electrons v_{th} and the other is the magnitude of the ambient magnetic field represented by Ω_e/Π_e.

Cold two-stream instability We performed two simulation runs of the two-stream instability formed by cold electron beams [Runs E and F]. In Figure 6.7, we plot snapshots of the spatial profiles of the electrostatic potentials at different times, $t = 8.15,\ 32.59,\ 65.18\times T_{pe}$. The left and right column shows the results of simulation runs with different magnitudes of the ambient magnetic fields. The left column corresponds to the simulation run of the cold two-stream instability with a weak magnetic field [Run E], and the right column corresponds to the simulation run of the cold two-stream instability with a strong magnetic field [Run F]. In this figure, potential are normalized by the thermal energy density of the thermalized electrons $(nmv_d^2/4q)$.

As analyzed in Section 3.2, since we have positive linear growth rates for the oblique mode as well as the parallel modes in the two-stream instability formed by cold electron beams, we find two-dimensional wavy structures in the initial phase of both runs with a weak and a strong magnetic fields. In the run with a weak magnetic field [Run E], presented in the left column of

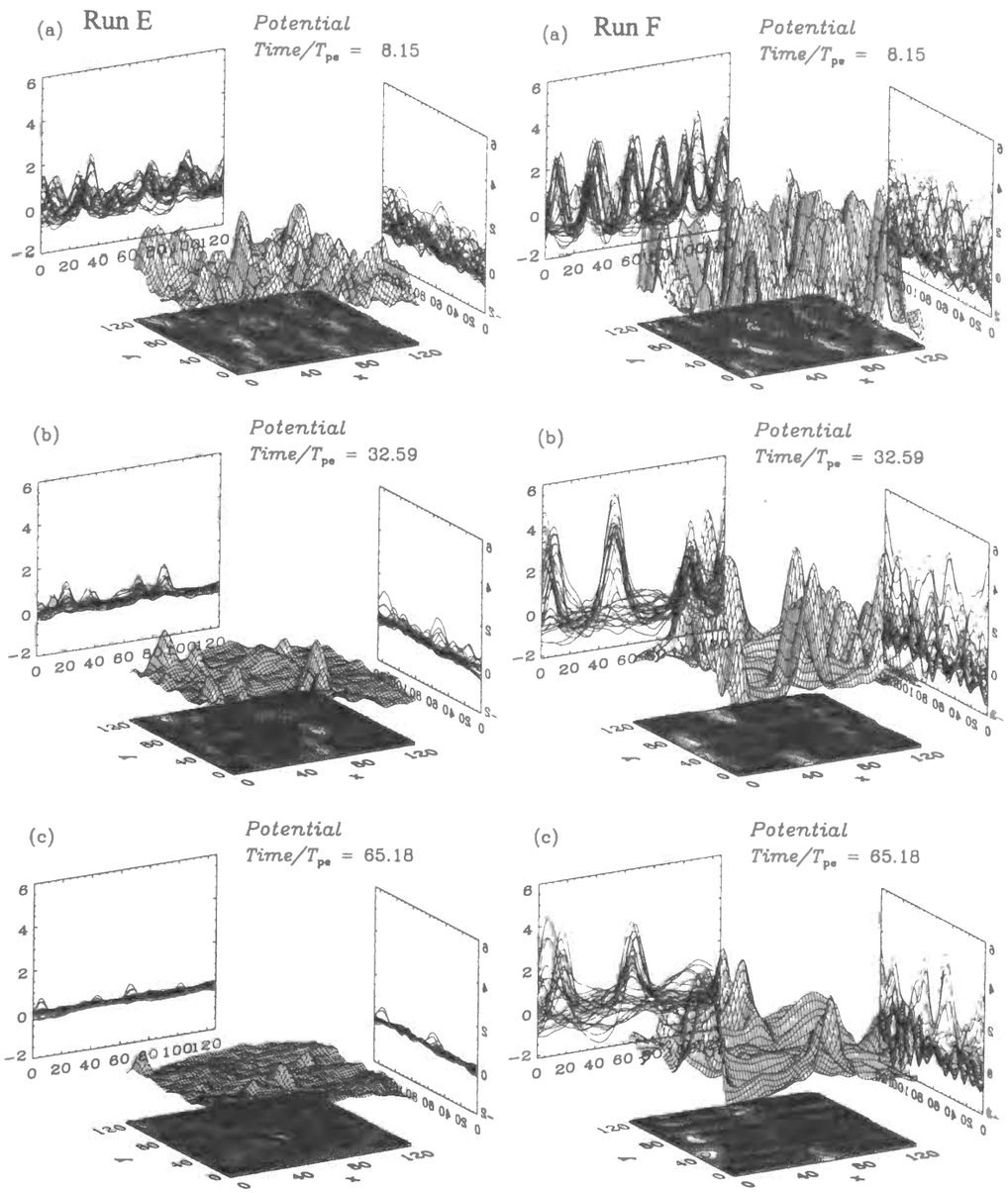

Figure 6.7: Spatial profiles of potentials at different times, $t = 8.15,\ 32.59,\ 65.18\times T_{pe}$, in Runs E and F of Table 6.4. Left column correspond to Run E, the simulation run with a weak magnetic field ($\Omega_e/\Pi_e = 0.4$), and right column correspond to Run F, the simulation run with a strong magnetic field ($\Omega_e/\Pi_e = 1.0$). The ambient magnetic field is taken along the x axis.

this figure, these potentials are diffused in time, and no significant structure exist in the bottom panel.

While in the run with a strong magnetic field [Run F], presented in the right column, these potentials are very stable at least for 65 electron oscillation periods as shown in the bottom panel ($t = 65.18 \times T_{pe}$). Though these potentials become aligned in the perpendicular direction, their two-dimensional structures are not changed. We can find a coherent perpendicular propagating wave which modulate the potentials in the almost perpendicular direction in the final state of this simulation. This quasi-perpendicular wave is an electrostatic whistler mode wave, and nonlinear evolution of this wave for a longer time is studied by *Goldman et al.* [1999]. In a long time evolution. this whistler mode wave grow larger, and electrostatic potentials corresponding to ESW are completely diffused. During this decay process, potentials are separated in the direction perpendicular to the ambient magnetic field, and isolated two-dimensional potentials are observed. Such isolated two-dimensional potentials, however, are very unstable and diffused in a short period.

Warm two-stream instability As a next step, we increase the thermal velocity of the electron beams, and performed two simulation runs of the electron two-stream instability formed by warm electron beams with different magnitudes of the ambient magnetic fields [Runs G and H]. Figure 6.8 show the spatial profiles of potentials in these runs at different times, $t = 8.15$, 32.59, $65.19 \times T_{pe}$. The left and right columns represent the results of the simulation run of the warm electron two-stream instability with a weak magnetic field [Run G], and those of the run with a strong magnetic field [Run H], respectively.

Contrary to the previous runs of the two-stream instability formed by cold electron beams, we can find almost one-dimensional potentials in both runs. In such warm electron beams, oblique mode waves are subject to the Landau and the cyclotron damping. The parallel mode wave becomes dominant, and electrostatic potentials excited by the initial instabilities are almost coherent in the perpendicular direction. These one-dimensional potentials coalesce with each other in the parallel direction, forming larger potentials. They are no longer subject to the influence of the magnetic field, and very stable for a long time.

In the run with a weak magnetic field [Run G], presented in the left column of this figure, one-dimensional potentials are diffused gradually, and some two-dimensional potentials are formed with a finite structure in the perpendicular direction. These two-dimensional potentials, however, are not stable, and diffused gradually as time goes on. While in the run with a strong magnetic field [Run H], presented in the right column, one-dimensional potentials, excited by the initial electron beam instability, coalesce with each other, forming larger potentials. In the final state, two clear one-dimensional potentials are formed, which are coherent in the direction perpendicular to the ambient magnetic field. In these simulations of the two-stream instability formed by warm electron beams, no whistler mode wave is observed. This is because such perpendicular propagating waves are damped in the warm electrons.

Two-stream instability with mobile ions The above four simulations with immobile ions (without ion dynamics) demonstrated that the both clear potentials with one- and two-dimensional spatial structures are formed in the runs with a strong magnetic field. In the simulation run of the cold electron two-stream instability with the strong magnetic field [Run F], clear two-dimensional potentials are formed, which are indicating isolated two-dimensional

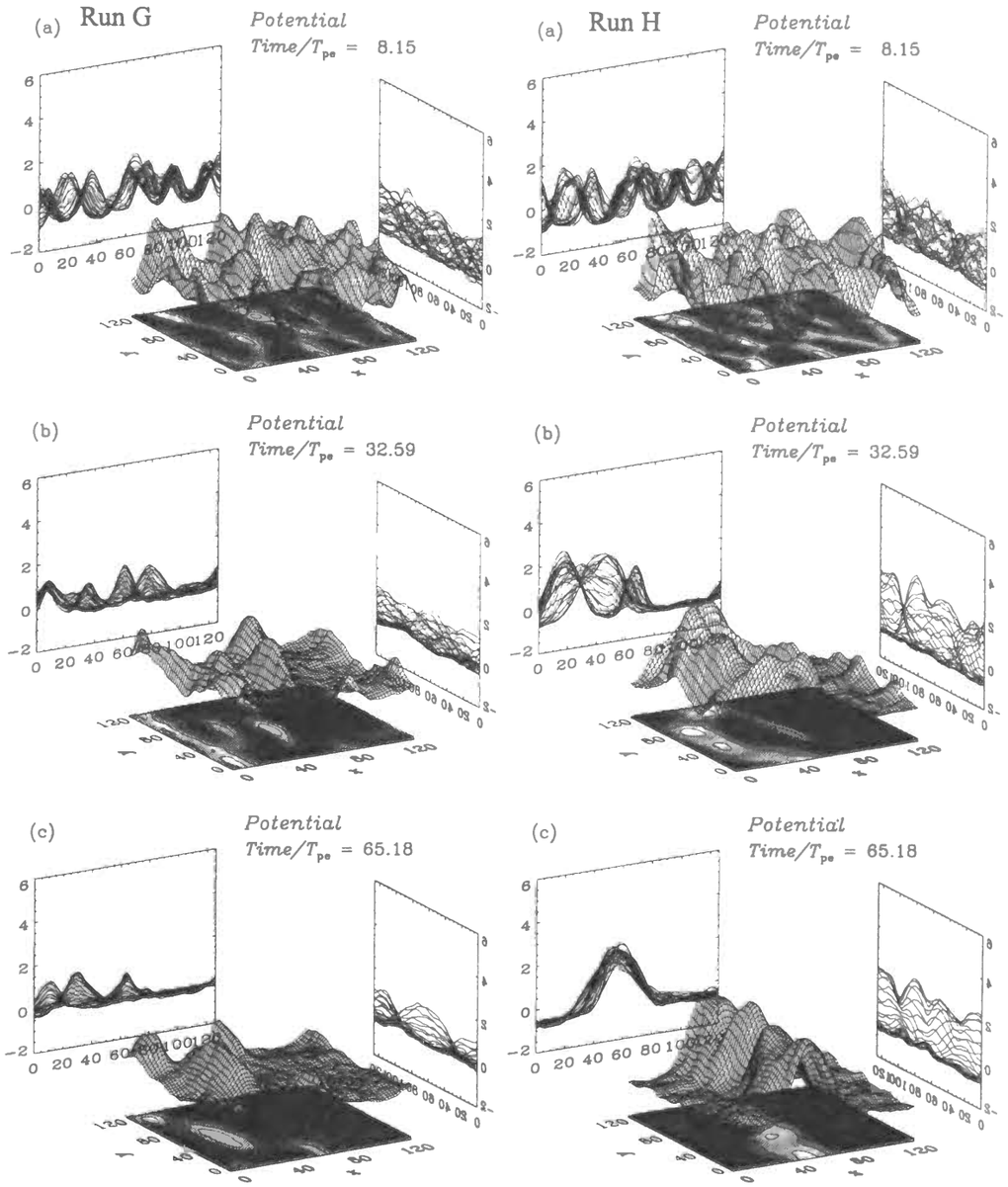

Figure 6.8: Spatial profiles of potentials at different times, $t = 8.15$, 32.59, $65.19 \times T_{pe}$, in Runs G and H of Table 6.4. Left column correspond to Run G, the simulation run with a weak magnetic field ($\Omega_e/\Pi_e = 0.4$), and right column correspond to Run H, the simulation run with a strong magnetic field ($\Omega_e/\Pi_e = 1.0$).

ESW observed in the auroral region. While in the simulation run of the warm electron two-stream instability with a strong magnetic field [Run H], clear one-dimensional potentials are formed.

Next, we performed these two simulation runs with using mobile ions (with ion dynamics), and investigated effects of ion dynamics on the formation mechanism and the spatial structures of ESW formed by the electron two-stream instability. Simulation parameters are listed in Run I and J of Table 6.4. In the left column of Figure 6.9, the time histories of $E_{\parallel}$ and $E_{\perp}$ energy densities in Runs I and J are presented. Spatial profiles of potentials in the final state of each simulations ($t = 260.72 \times T_{pe}$) are presented in the right column of this figure.

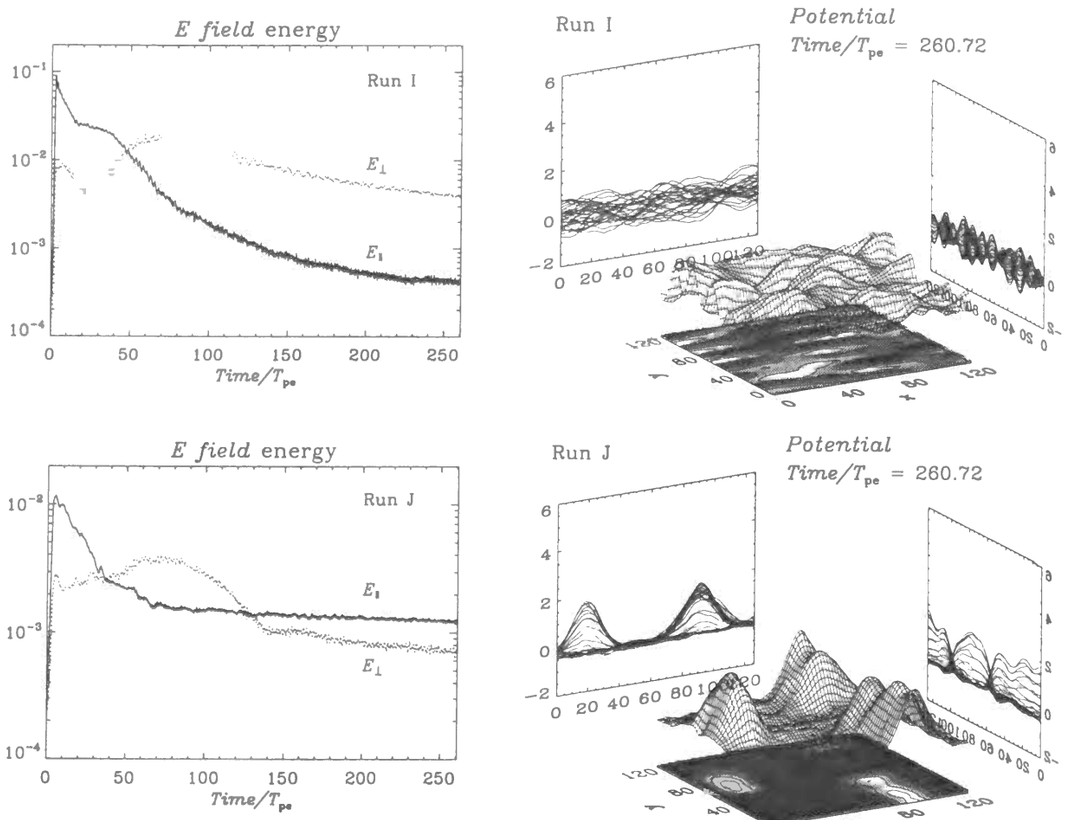

Figure 6.9: Left panels show time histories of $E_{\parallel}$ and $E_{\perp}$ energy densities in Runs I and J, and right panels show spatial profiles of potentials in the final state of each simulation ($t = 260.72 \times T_{pe}$). Upper and lower panels correspond to Runs I and J of Table 6.4, respectively.

In the simulation run of the cold electron two-stream instability with a strong magnetic field ($\Omega_e = 1.0 \times \Pi_e$) [Run I], presented in the upper panels, electrostatic potentials are diffused completely, and a coherent quasi-perpendicular wave is observed. This is the quasi-perpendicular whistler mode wave, which is also observed in the previous simulation run [Run F]. Since the ion dynamics is neglected in the previous simulation run, this whistler mode wave is excited due to

the pure electron dynamics. The energy of the two-dimensional electrostatic potentials, which are excited by the initial two-stream instability, decay into the quasi-perpendicular whistler mode wave. Correspondingly, the $E_{\parallel}$ energy decay into the $E_{\perp}$ energy as presented in the left panel. The $E_{\perp}$ energy keeps a high value in the whole simulation time, while the $E_{\parallel}$ energy decrease to the noise level.

In the simulation run of the warm electron two-stream instability with a strong magnetic field ($\Omega_e = 1.0 \times \Pi_e$) [Run J], presented in the lower panels, clear two-dimensional potentials are formed in the final state. Such two-dimensional potentials are not observed in the previous simulation run without ion dynamics [Run H]. Therefore, these two-dimensional potentials are formed due to the ion dynamics. Correspondingly, the $E_{\perp}$ energy increase at $t = 20 \sim 70 \times T_{pe}$, which indicates that some waves are excited in the direction perpendicular to the ambient magnetic field. These perpendicular waves separate the one-dimensional potentials, which are formed due to the electron dynamics, in the perpendicular direction, forming the isolated two-dimensional potentials. Contrary to the previous simulation of the cold electron two-stream instability, the $E_{\parallel}$ energy do not decrease to the noise level, and it keeps a relatively high value in the whole simulation time. This is because clear two-dimensional potentials exist very stably in the whole simulation time. In addition, the scale length of these potentials in the direction perpendicular to the ambient magnetic field is almost equal to that of ion gyroradius. This is because potentials are separated due to the ion dynamics in the perpendicular direction.

Parametric dependence

The above six simulation runs for the different parameters demonstrated that clear ESW are formed in the simulation runs with a strong magnetic field [Runs F, H]. The electrostatic potentials excited by the cold electron two-stream instability have the isolated two-dimensional structure, as shown in the right column of Figure 6.7 [Run F]. Such isolated two-dimensional potentials are consistent with the two-dimensional ESW observed in the auroral region, as presented in Section 2.3. These two-dimensional potentials, however, decay into the quasi-perpendicular whistler mode waves, and diffused completely in a long time evolution, as shown in the upper panel of Figure 6.9.

On the other hand, the electrostatic potentials excited by the warm electron two-stream instability have the one-dimensional structures, as shown in the right column of Figure 6.8 [Run H]. These one-dimensional potentials, however, separated in the direction perpendicular to the ambient magnetic field due to the ion dynamics, forming the isolated two-dimensional potentials, as shown in the lower panel of Figure 6.9. Contrary to the two-dimensional potentials excited by the cold two-stream instability, these two-dimensional potentials are very stable at least more than 260 $\times T_{pe}$. These two-dimensional structures of the potentials are consistent with the two-dimensional ESW in the auroral region. In addition, the scale length of ESW in the perpendicular direction is reported to be that of the local ion gyroradius by the FAST observations [*Ergun et al.*, 1998]. This is also consistent with the above simulation result of the warm two-stream instability with mobile ions [Run H].

According to these simulation results, we can assume that the two-dimensional ESW observed in the auroral region are excited by the warm electron two-stream instability. Especially the ion dynamics plays an important role in the formation mechanism of such two-dimensional structures. In the following subsection, we will examine further analysis of the effect of the ion dynamics in the formation mechanism of the isolated two-dimensional ESW from the warm

electron two-stream instability.

6.3.3 Effects of ion dynamics on two-dimensional ESW formation

As presented in the previous subsection, we assumed that the two-dimensional ESW in the auroral region are formed by the two-stream instability formed by warm electron beams. During the formation mechanism of such two-dimensional ESW, effects of the ion dynamics are very important. In this subsection, therefore, we further investigate the simulation results of the warm two-stream instability with mobile ions [Run J]. By comparing two simulation runs with and without ion dynamics, we estimated effects of ion dynamics on the formation mechanism of the two-dimensional ESW [*Miyake et al*, 1999]. We performed two-dimensional electrostatic particle simulations of the two-stream instability formed by warm electron beams with and without ion dynamics [Runs H and J in Table 6.4]. To confirm effects of the ion dynamics in the present simulations, we executed new simulation runs with the same plasma parameters for much longer time than the previous simulations. The total simulation time of the run without the ion dynamics [Run H] is $260\times T_{pe}$, and that of the run with the ion dynamics [Run J] is over $1{,}000\times T_{pe}$.

Spatial profiles of potentials Figure 6.10 presents spatial profiles of potentials at different times, $t = 8.15,\ 32.59,\ 65.18\times T_{pe}$. The left and right panels show the results of Runs H (with immobile ions) and J (with mobile ions), respectively. In this figure, potential values are normalized by the initial thermal energy density of electrons ($|n_0 m_e v_t^2/q|$), spatial lengths are scaled by the Debye length of background electrons (v_t/Π_e), and times are scaled by the total electron plasma oscillation period (T_{pe}).

During the initial phase, these is no significant difference between Run H and J, as shown at $t = 8.15 \times T_{pe}$ in the both left and right columns of Figure 6.10. Two-dimensional potentials are excited by the initial two-stream instability in both runs. As time goes on, however, these potentials coalesce with each other, and a clear difference appears between these two runs. In the left column of this figure [Run H], two-dimensional potentials are aligned in the direction perpendicular to the ambient magnetic field, then become a clear one-dimensional potential. In the right column [Run J], on the other hand, potentials are separated in the perpendicular direction as well as parallel direction, forming isolated two-dimensional potentials. This difference is, of course, due to the ion dynamics. In the absence of ion dynamics [Run H], an one-dimensional potential is formed at $t = 65.18 \times T_{pe}$. Including ion dynamics [Run J], on the other hand, potentials are divided in the perpendicular direction, the isolated two-dimensional potentials are formed. This simulation result suggests that two-dimensional potentials which are excited by the initial electron beam instability become one-dimensional structure due to the electron dynamics. These potentials, however, are divided in the perpendicular direction by the ions dynamics, forming isolated two-dimensional structures.

Time history of electric field energy The left column in Figure 6.11 shows time histories of $E_\parallel$ and $E_\perp$ energy densities in these simulation runs during $t = 0 \sim 200 \times T_{pe}$. The upper and lower panels correspond to Runs H and J, simulation runs without and with ion dynamics, respectively. The right column respectively shows contour plots of electrostatic potentials at $t = 97.77 \times T_{pe}$ in Runs H and J. In this figure, all the electric field energy densities are scaled

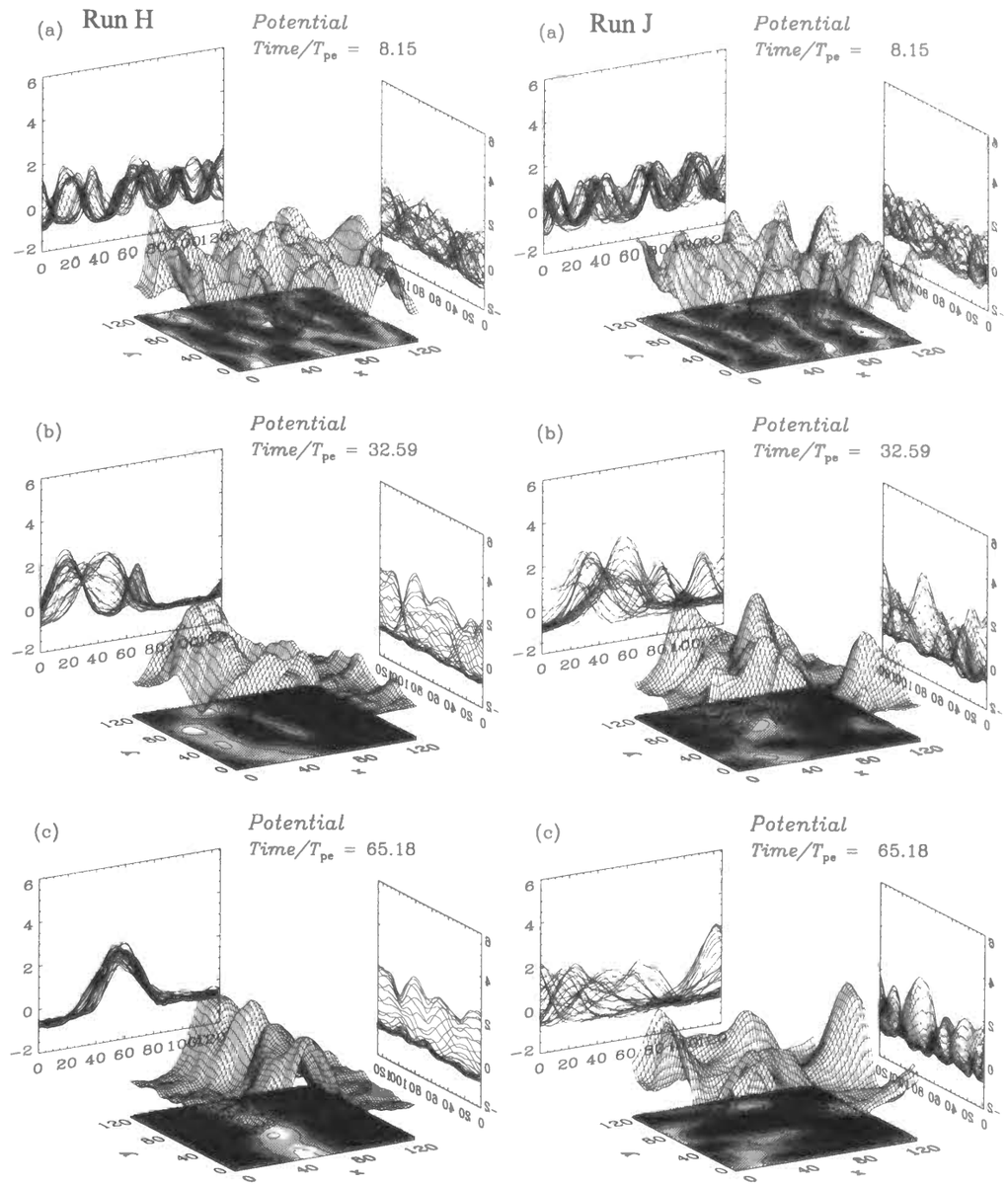

Figure 6.10: Spatial profiles of potentials at different times, $t = 8.15,\ 32.59,\ 65.18\times T_{pe}$, in Run H and J of Table 6.4, the simulation runs of the warm two-stream instability with a strong magnetic field ($\Omega_e/\Pi_e = 1.0$). Left and right columns present results of simulation Runs H and J, respectively.

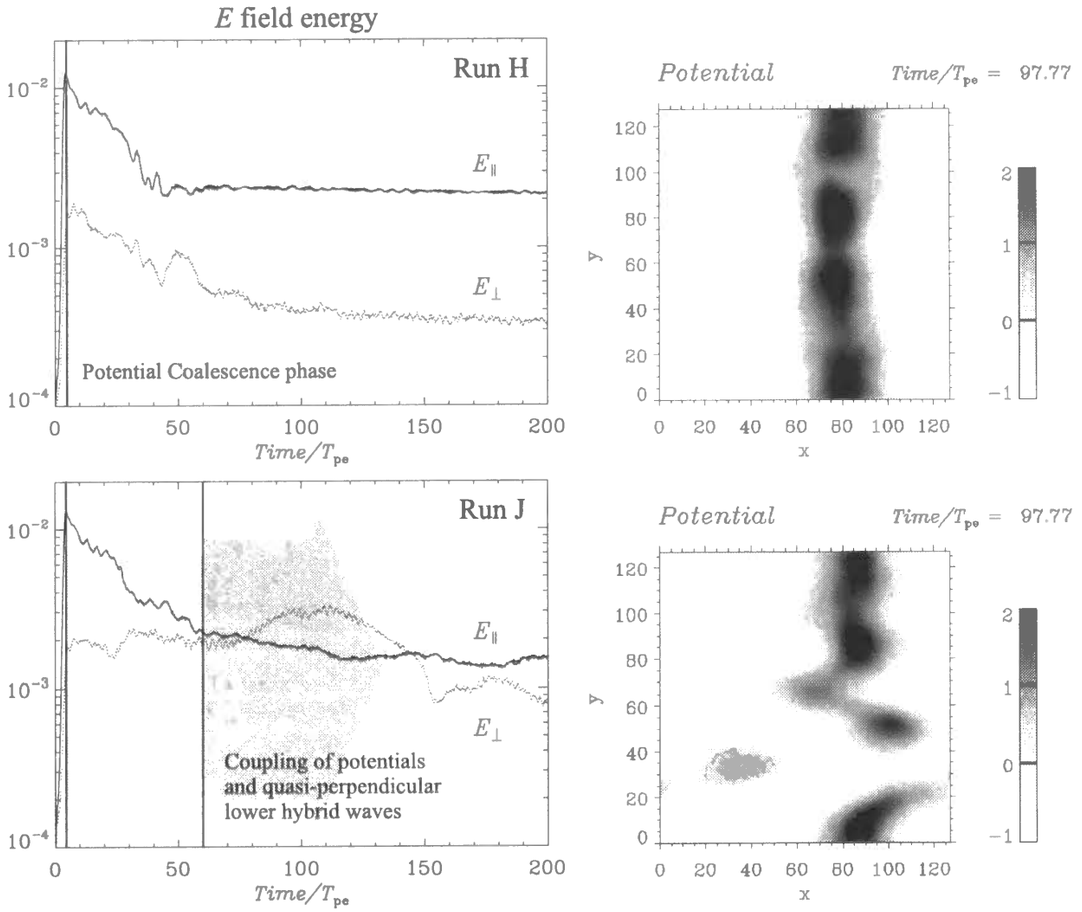

Figure 6.11: Left panels show time histories of $E_\parallel$ and $E_\perp$ energy densities in Runs H and J, and right panels show spatial profiles of potentials at $t = 97.77 \times T_{pe}$ in each run. Upper and lower panels correspond to Runs H and J of Table 6.4, respectively.

by the initial thermal energy density of electrons ($|n_0 m_e v_t^2|$).

As the initial electron beam instability develops, both $E_\parallel$ and $E_\perp$ energies increase. The electric field energies reach saturation due to the nonlinear trapping of electrons in electrostatic potentials. These electrostatic potentials coalesce with each other, forming larger potentials. Through this coalescence process of potentials, both $E_\parallel$ and $E_\perp$ field energies decrease. The quasi-stepwise changes in the $E_\parallel$ energy history represent the time when two potentials coalesce with each other and form large one potential. In the run with immobile ions, shown in the upper panel [Run H], the $E_\parallel$ energy stops decreasing after the coalescence phase. This is because a stable one-dimensional potential coherent in the direction perpendicular to the ambient magnetic field is formed at the end of the coalescence phase, as shown in the right panel of Figure 6.11. In the run with mobile ions, shown in the lower panel [Run J], on the other hand, the $E_\parallel$ energy continues to decrease even after the coalescence phase. At the same time, we can find the increase of the $E_\perp$ energy at $t = 70 \sim 140 \times T_{pe}$ in this figure. This indicates that the energy of the solitary waves drifting along the magnetic field decays into the perpendicular direction. During this decay phase, some waves are excited in the quasi-perpendicular direction as shown in the right panel. Figure 6.12 shows $k_\parallel$-$k_\perp$ profile of potentials at $t = 97.77 \times T_{pe}$ in this simulation [Run J]. The wavenumber spectrum shown in this figure indicates the excitation of electrostatic wave at an angle close to the perpendicular direction. The normal mode in this propagation angle is lower hybrid waves satisfying the condition $k_\perp \rho_i \simeq 1$.

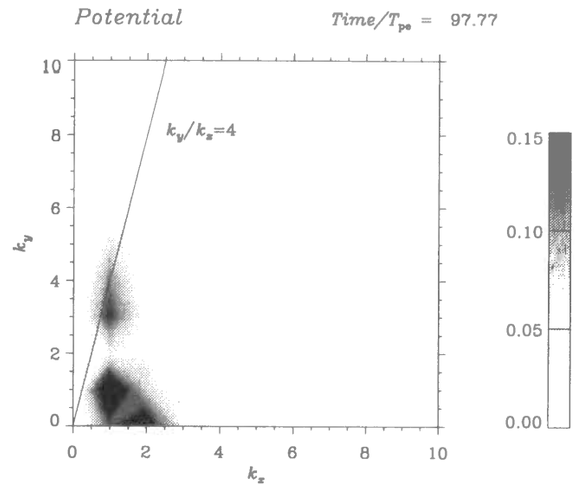

Figure 6.12: Wavenumber spectrum ($k_\parallel$-$k_\perp$) of potentials at $t = 97.77 \times T_{pe}$ in Run J (with mobile ions). This is obtained by Fourier transformation of electrostatic potential structures of all the simulation system.

Time evolution of potential structures Figure 6.13 shows time histories of $E_\parallel$ and $E_\perp$ energy densities for the whole simulation period of Run J, the run with mobile ions. In this figure, we can divide the time history into five phases, "Linear instability phase" ($t = 0 \sim 4 \times T_{pe}$), "Coalescence phase" ($t = 4 \sim 60 \times T_{pe}$), "Decay phase" ($t = 60 \sim 250 \times T_{pe}$), "Striation phase" ($t = 250 \sim 650 \times T_{pe}$) and "Stable phase" ($t = 650 \sim \times T_{pe}$). Among these five phases, the former three phases, "Linear instability phase", "Coalescence phase" and "Decay phase" are already shown in the lower panel of Figure 6.11.

In "Linear instability phase", the initial electron beam instability takes place resulting rapid increase of both $E_\parallel$ and $E_\perp$ field energy. At the end of this phase, these E field energies reach to the saturation due to nonlinear trapping of electrons in electrostatic potentials which are excited by the electron beam instability. These potentials have two-dimensional spatial structures as shown in the panel (a) of this figure. "Coalescence phase" follows the saturation of the initial

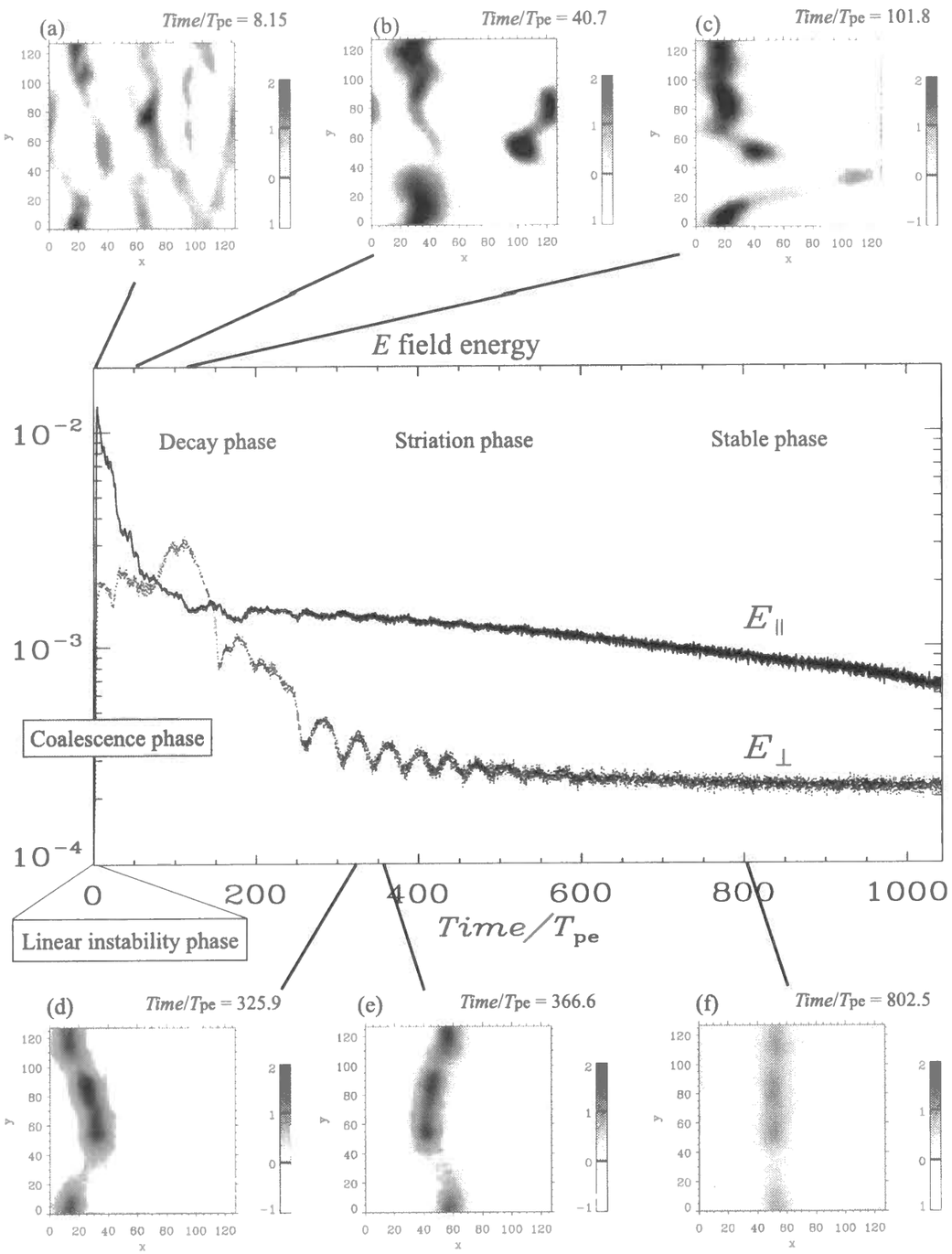

Figure 6.13: Time histories of $E_{\parallel}$ and $E_{\perp}$ energy densities for the whole simulation period of Run B, and corresponding potential structures are presented. We divide the time history into five different phases, "Linear instability phase" ($t = 0 \sim 4 \times T_{pe}$), "Coalescence phase" ($t = 4 \sim 60 \times T_{pe}$), "Decay phase" ($t = 60 \sim 250 \times T_{pe}$), "Striation phase" ($t = 250 \sim 650 \times T_{pe}$) and "Stable phase" ($t = 650 \sim \times T_{pe}$).

electron beam instability.

During "Coalescence phase", the two-dimensional potentials excited by the initial electron beam instability coalesce with each other in the direction parallel to the ambient magnetic field, and isolated in the parallel direction. When effects of ion dynamics are neglected, these potentials become one-dimensional being coherent in the perpendicular direction. In this simulation, however, the energy of the solitary waves decays to the perpendicular direction due to the ion dynamics. During this "Decay phase", strong quasi-perpendicular lower hybrid waves are excited as stated above. Potentials are divided in the perpendicular direction by these strong quasi-perpendicular waves, forming isolated two-dimensional potentials, as shown in the panel (b) of this figure.

After "Decay phase", isolated two-dimensional potentials are gradually aligned in the perpendicular direction, forming coherent one-dimensional potentials. During this "Striation phase", since potentials are stable, the $E_{\parallel}$ energy keep almost constant value. The $E_{\perp}$ energy, however, is decreasing. In Figure 6.13, $E_{\perp}$ energy is decreasing with oscillation during "Striation phase". This oscillation corresponds to variation of the relative drift velocity between two potentials, as shown in the panels (d) and (e) of this figure. The time period of this oscillation is almost equal to 10 electron plasma oscillation periods ($10 \times T_{pe}$). Since the electron plasma frequency is 1.0 ($\Pi_e = 1.0$), the electron cyclotron frequency is 1.0 ($\Omega_e = 1.0$) and the ion cyclotron frequency is 0.01 ($\Omega_i = 0.01$) in this simulation, this time period is equal to that of lower hybrid waves ($T_{LHR} = 2\pi/\sqrt{\Omega_e \Omega_i} \simeq 10 \times T_{pe}$).

At the end of "Striation phase" ($t = 650 \times T_{pe}$), an uniform one-dimensional potential is formed, as shown in the panel (f) of this figure. This one-dimensional potential is very stable and exists for a long time at least more than 10 ion gyro periods.

6.4 Discussion

6.4.1 Parametric dependence of one-dimensional ESW formation

In Section 6.2, we performed a series of two-dimensional electrostatic particle simulations of the electron bump-on-tail instability, as a possible generation instability of the one-dimensional ESW observed in the PSBL region by the Geotail spacecraft. In these simulations, we confirmed that stable one-dimensional potentials can be formed from the electron bump-on-tail instability. These potentials have uniform structures in the direction perpendicular to the ambient magnetic field, as predicted by the Geotail observation analyses. The present simulation results demonstrated that a certain magnitude of the ambient magnetic field is necessary for the formation of ESW potentials. To investigate the parametric dependence of ESW formation on the ambient magnetic field, we performed a series of simulation runs with different magnitudes of the ambient magnetic fields, $\Omega_e/\Pi_e = 0.2$, 0.4, and 1.0. Then we have confirmed that Runs A and B (the cases of $\Omega_e/\Pi_e = 1.0$ and 0.4) lead to the formation of stable one-dimensional ESW potentials. We can find clear one-dimensional ESW potentials in the final state ($t = 130.37 \times T_{pe}$) of Runs A and B, as shown in Figures 6.1 and 6.2.

In the simulation run with a strong magnetic field [Run A], electrostatic potentials excited by the electron bump-on-tail instability are not coherent in the initial state. Since the Larmor radius of the background electrons is small ($r_L = 1.0$) and the electrons are strongly bound to the ambient magnetic field, these potentials, which are formed by the trapped electrons,

are localized and incoherent in the perpendicular direction. These potentials, however, become coherent through striation process in the perpendicular direction, forming an uniform one-dimensional potential.

In the simulation run with a relatively weak magnetic field [Run B], on the other hand, electrostatic potentials are coherent even in the initial state. In this case, the coherency in the perpendicular direction is formed during the linear wave growth. In this simulation, the ratio of the linear growth rate of the most dominant parallel mode wave $E_\parallel$ ($\gamma_\parallel$) to that of a oblique mode E_θ (γ_θ), $\gamma_\parallel/\gamma_\theta$ is larger than that in the run with a strong magnetic field [Run A], as analyzed in Section 3.2. Growth rates of the oblique mode waves are smaller in this case, and the electrostatic potentials excited by the initial instability are more coherent in the direction perpendicular to the ambient magnetic field. Thus the coherency at the saturation of the linear wave growth of potentials is higher for a smaller magnetic field.

This result indicates that it takes much longer time to form one-dimensional ESW in a stronger magnetic field. This property of the linear growth rates is due to the coupling of the perpendicular electric fields $E_\perp$ and the cyclotron motion of the majority thermal electrons.

6.4.2 Parametric dependence of two-dimensional ESW formation

In Section 6.3, we performed a series of two-dimensional electrostatic particle simulations of the electron two-stream instability, as a possible generation instability of the two-dimensional ESW observed in the auroral region by several satellites, such as the FAST and the Polar satellites. In these simulation, we confirmed the formation of the isolated two-dimensional ESW from the cold and the warm electron two-stream instability.

Dependence on electron dynamics Figure 6.14 represents the spatial profiles of potentials at the end of the simulation time ($t = 260.72 \times T_{\rm pe}$) in all the simulation runs of the two-stream instability without ion dynamics [Runs E∼H]. This figure indicates the following conclusions.

- The formation of clear potentials from the two-stream instability needs a strong magnetic field.
- The cold electron two-stream instability excites the two-dimensional potentials.
- The warm electron two-stream instability excites the one-dimensional potentials.

These simulation results indicate that the spatial structure of ESW potentials, which are excited by the electron two-stream instability, is controlled by the temperature of electron beams. Especially, the quasi-perpendicular whistler mode waves play an important role in the controlling process of the spatial structure of ESW. In the cold two-stream instability [Run F], the quasi-perpendicular whistler mode waves are strongly excited and electrostatic potentials have clear perpendicular structures due to such strong perpendicular waves. While in the warm two-stream instability [Run H], the quasi-perpendicular whistler mode waves are not excited, and potentials have the one-dimensional structure coherent in the direction perpendicular to the ambient magnetic field. We have two different damping processes to attenuate oblique mode waves, the Landau damping and the cyclotron damping. The effect of the Landau damping is controlled by the thermal velocity of electrons in the parallel direction $v_{t\parallel}$. While the effect of

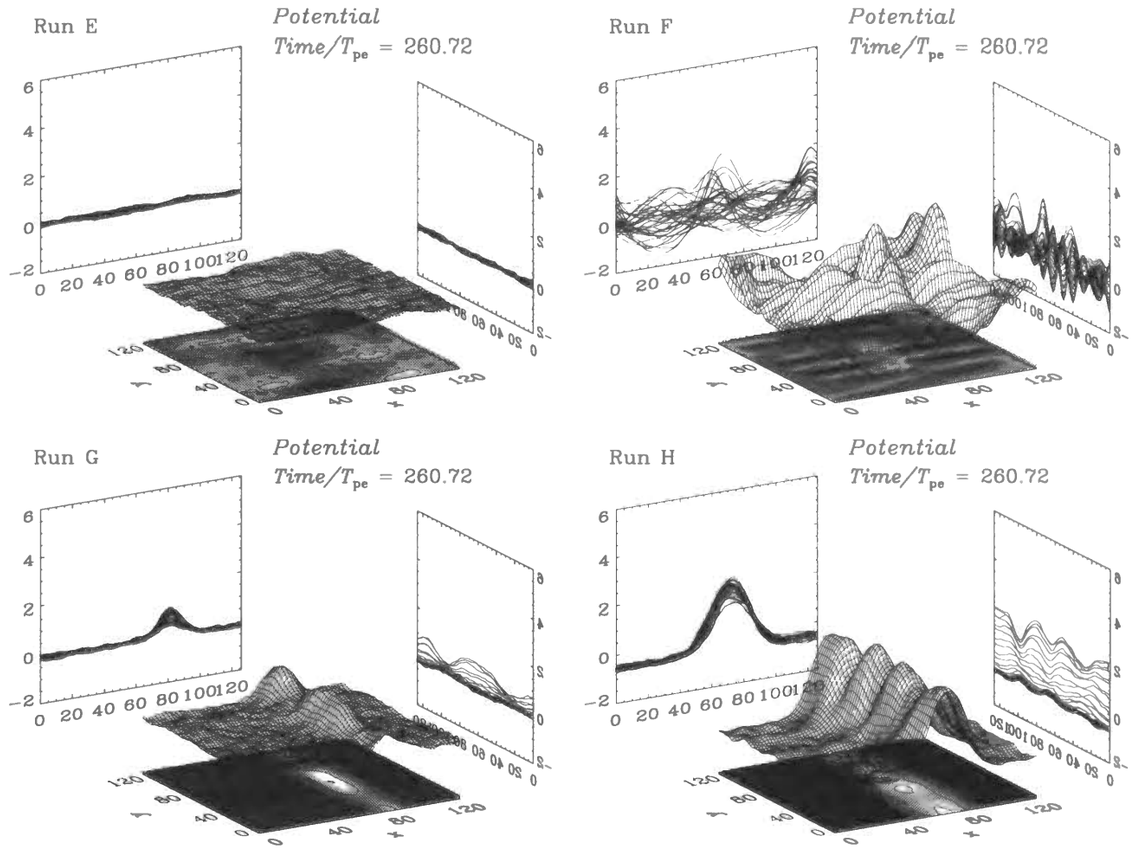

Figure 6.14: Spatial profiles of potentials at the end of the simulation time ($t = 260.72 \times T_{\rm pe}$) in Runs E∼H of Table 6.4.

the cyclotron damping is controlled by the thermal velocity of electrons in the perpendicular direction $v_{t\perp}$.

To confirm which damping process is dominant in these simulations, we performed another simulation run of the two-stream instability formed by anisotropic electron beams ($v_{t\parallel} \neq v_{t\perp}$) [Run F']. We assumed the cold electron two-stream instability with a warm perpendicular thermal velocity, $v_{t\parallel} = 0.5$ and $v_{t\perp} = 1.0$. Other simulation parameters are the same with those in Run F. When the cyclotron damping is dominant, we can expect that the quasi-perpendicular whistler mode waves are not excited due to the cyclotron damping, and one-dimensional potentials are formed in this simulation.

Figure 6.15 shows the result of this simulation, presenting a spatial profile of potentials in the final state, at $t = 260.72 \times T_{pe}$. We can find clear two-dimensional potentials with quasi-perpendicular whistler mode waves in this figure. This shows completely the same result with Run F, the simulation run of the cold two-stream instability, indicating that the cyclotron damping process is not effective in the present simulations. This simulation result presents that the quasi-perpendicular whistler mode waves are attenuated due to the Landau damping process, not the cyclotron damping. In other words, the thermal velocity of electrons in the direction parallel to the ambient magnetic field is supposed to be the controlling parameter of the spatial structure of ESW excited from the electron two-stream instability.

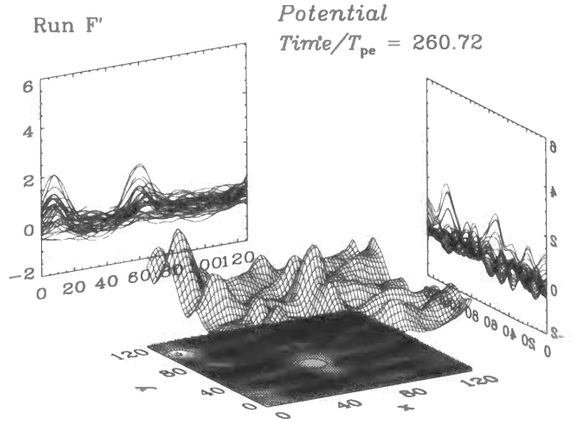

Figure 6.15: Spatial profile of potentials in the final state ($t = 260.72 \times T_{pe}$) of Run F', the simulation run of the two-stream instability formed by anisotropic electron beams, $v_{t\parallel} = 0.5$ and $v_{t\perp} = 1.0$.

Dependence on ion dynamics As studied in the previous subsection (Subsection 6.3.2), the two-dimensional potentials excited by the cold two-stream instability are unstable, and they decay into the quasi-perpendicular whistler mode waves in a long time evolution. Such unstable potentials are not suitable for a model of the two-dimensional ESW in the auroral region. On the other hand, the one-dimensional potentials excited by the warm two-stream instability are divided in the direction perpendicular to the ambient magnetic field, forming isolated two-dimensional potentials, in the existence of the ion dynamics. These two-dimensional potentials are very stable, and their spatial scale in the perpendicular direction is that of the ion Larmor radius. This is consistent with the nature of the two-dimensional ESW in the auroral region, reported by the FAST satellite.

6.4.3 Striation process of potentials

In the simulation runs of the both bump-on-tail and two-stream instabilities, potentials coalesce with each other, and they become isolated in the direction parallel to the ambient magnetic field, after the initial electron beam instability. This striation process of potentials is only due to electron dynamics, and explained as follows. At first, we assume two isolated potentials traveling along the ambient magnetic field with different drift velocities, v_{d1} and v_{d2}. Since these two potentials have a relative velocity $|v_{d1} - v_{d2}|$, they gradually come close, and they are aligned in the perpendicular direction at some time. At that moment, $E_\perp$ decrease between two potentials, and trapped electrons are mixed in the perpendicular direction. Since electrons are already balanced with potentials, these mixed electrons lose their parallel drift energy, being affected by a potential, which is oscillating with a different phase, and then the relative drift velocity of two potentials ($|v_{d1} - v_{d2}|$) decreases. Through this mixing process, the parallel drift energy of the mixed electrons is converted to thermal energy. In a long time evolution, two potentials are aligned completely in the perpendicular direction, forming a single coherent one-dimensional potential.

6.4.4 Trapping and cyclotron period

In the electron bump-on-tail instability, the magnetic field is effective for the perpendicular coherency, if the time period of electron cyclotron motion is as short as the characteristic time period of nonlinear evolutions. In the present simulations of the bump-on-tail instability, the characteristic time period is determined by electrons trapped in electrostatic potentials. During the perpendicular striation process, the potentials coalesce with each other to decrease total potential energy in the simulation system.

Run	Ω_e	ω_T	Ω_e/ω_T
Run A	1.0	0.184	5.43
Run B	0.4	0.187	2.14
Run C	0.2	0.185	1.08

Table 6.5: Electron cyclotron frequencies Ω_e, trapping frequency ω_T, and their ratios in Runs A$\sim$C, the simulation runs of the electron bump-on-tail instabilities.

As mentioned in Section 3.4, the resonant electrons trapped in electrostatic potentials are oscillating with a trapping frequency ω_T which is given by

$$\omega_T = \sqrt{\frac{eE_w k}{m}} \tag{6.1}$$

where E_w is the amplitude of the electrostatic wave in which electrons are trapped, k is the wave number, and e and m are the charge and the mass of an electron, respectively. For formation of uniform potentials through striation process in the perpendicular direction, the electron cyclotron frequency must be larger than the trapping frequency ($\Omega_e/\omega_T \geq 1$). This indicates that a certain magnitude of the ambient magnetic field is necessary for the formation of ESW potentials. In the present study, the ratios of Ω_e/ω_T in each run of the electron bump-on-tail

instability are presented in Table 6.5. For all the present simulation runs, the cyclotron motion yields a substantial effect on the striation process during one trapping period, while we could not find the ESW formation only in Run C with $\Omega_e/\Pi_e = 0.2$. We need to look for another mechanism that prevents ESW formation.

6.4.5 Enhanced thermal fluctuations

The formation process of one-dimensional ESW from the electron bump-on-tail instability is subject to the enhanced thermal fluctuations. In the present case ($k\lambda_D \ll 1$), the thermal fluctuations W are written as

$$W \simeq \frac{n_0 T_e}{n_0 \lambda_D^3} \simeq \frac{n_0 T_e}{\Lambda} \tag{6.2}$$

This equation indicates that the thermal fluctuations are inversely proportional to the plasma parameter Λ, i.e., the number of particles per Debye cube. In the real space plasma, for example in the PSBL, $\lambda_D \simeq 4.0 \times 10^2$ (m) and $n_0 \simeq 1.0$ (cm^{-3}). When we assume a two-dimensional system, where all the variations of spatial parameters are two-dimensional, the plasma parameter in such a two-dimensional system Λ_{2D} is written as $n_0\lambda_D^2$. With the parameters in the PSBL, $\Lambda_{2D} \simeq 1.6 \times 10^{11}$. In the present simulation systems, on the other hand, $\Lambda_{2D} = 34,603,008/(64 \times 64) = 8,448$. This is much smaller than that in the PSBL. This indicates that the thermal fluctuations are much more enhanced in the present simulations than those in the PSBL.

To confirm the influences of the enhanced thermal fluctuations, we performed a series of simulation runs of the bump-on-tail instability varying the number of superparticles in the simulation system. In Figure 6.16, we present the time evolution of spatial profiles of potentials in one of these simulation runs. In this simulation, we used only 8,650,752 superparticles as shown in Run D of Table 6.2, which are 1/4 of those in the previous runs [Runs A∼C]. All the other parameters are the same as those in Run B. In Figure 6.16, the spatial structures of potentials are less coherent with much noise in the initial phase. Since the coherent potential structures excited by the bump-on-tail instability are not so large, they are tend to be diffused because of the enhanced thermal fluctuations. For example, the $E_\parallel$ energy density in the final state of Run B, where two clear ESW potentials are formed, is almost the same order of the thermal noise level in Run D. Therefore, the electrostatic potential structures are almost completely diffused by the enhanced thermal fluctuations in Run D. In addition, we can also find the effects of these fluctuations even in the beginning of the coalescence process, as shown at $t = 32.58 \times T_{pe}$. The potentials contain much more fluctuations in the perpendicular direction at saturation time in Run D, which are less coherent than those in Run B.

The coherency of electrostatic potentials at the saturation can be expressed as a function of the thermal fluctuation level. Assuming that the most dominant parallel mode $E_\parallel$ with the maximum growth rate $\gamma_\parallel$ and an oblique mode E_θ with a smaller growth rate γ_θ ($\gamma_\theta < \gamma_\parallel$) grow from the same thermal fluctuation level E_T, we can derive the following relation,

$$\ln \frac{E_{\parallel,s}}{E_{\theta,s}} = \left(1 - \frac{\gamma_\theta}{\gamma_\parallel}\right) \ln \frac{E_{\parallel,s}}{E_T} \tag{6.3}$$

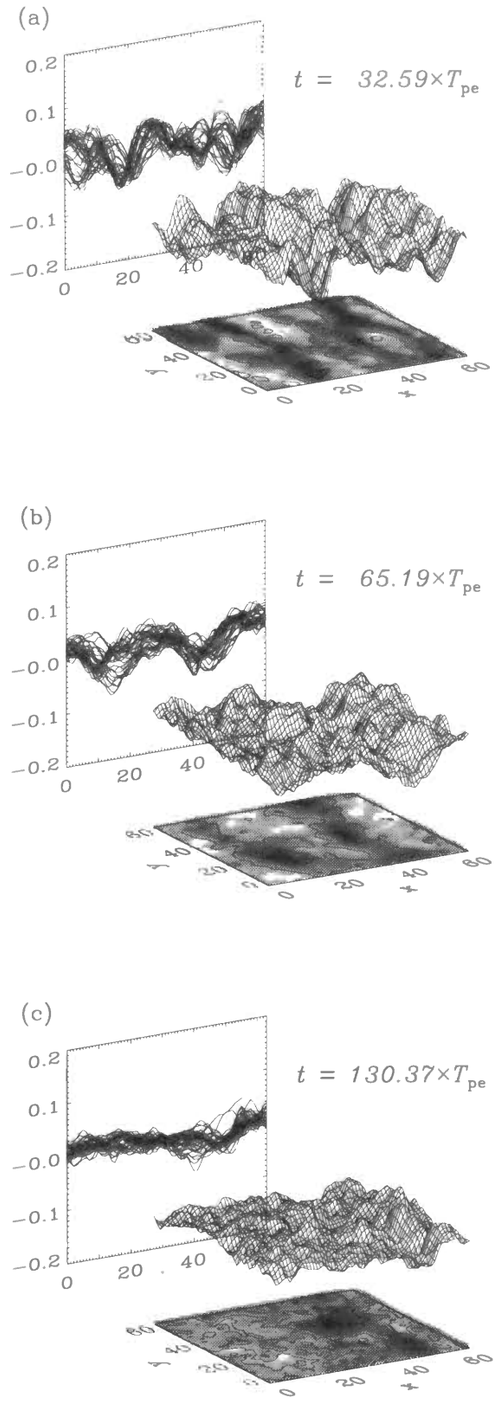

Figure 6.16: Spatial profiles of potentials at different times, $t = 32.59$, 65.19, $130.37 \times T_{pe}$ in Run D of Table 6.2. In this simulation, the number of superparticles is 8,650,752, and other parameters are the same as those in Run B ($\Omega_e/\Pi_e = 0.4$).

where $E_{\parallel,s}$ and $E_{\theta,s}$ are the saturation levels of $E_\parallel$ and E_θ, respectively. Therefore, a high coherency of the parallel mode, i.e., a large $E_{\parallel,s}/E_{\theta,s}$ can be attained when E_T is small enough. This effects of the enhanced thermal fluctuations are described in Section 4.2.

In a simulation run with a larger number of superparticles, the smaller thermal fluctuations will give a higher coherency of electrostatic potentials in the perpendicular direction. Although we did not find the formation of ESW in Run C ($\Omega_e/\Pi_e = 0.2$), use of a much larger number of superparticles would have yielded ESW formation.

6.4.6 Decay process through coupling of potentials and lower hybrid waves

During the formation process of the two-dimensional ESW from the warm electron two-stream instability [Run J], the parallel potential energy $E_\parallel$ is decreasing after coalescence phase, as shown in the lower panel of Figure 6.11. At the same time, the perpendicular potential energy $E_\perp$ is increasing, and strong quasi-perpendicular waves are excited. This suggests that parallel potential energy decay to perpendicular waves. These perpendicular waves are the lower hybrid waves as clearly shown in Figure 6.17. In this figure, we can find two clear branches of waves, the

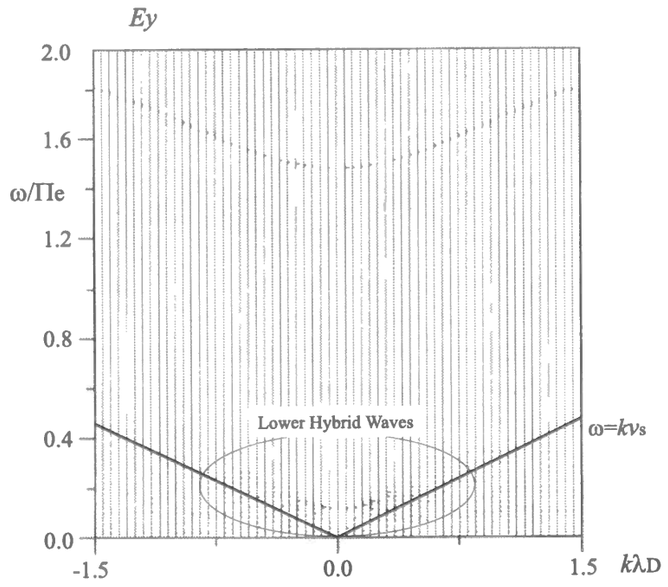

Figure 6.17: The ω-k diagram of the $E_\perp$ field for Run J. The spectra are obtained by Fourier transforming the $E_\perp$ field in space and time ($t = 0.25 \sim 1043.6 \times T_{pe}$). The plotted modes are perpendicular to the ambient magnetic field.

upper hybrid waves and the lower hybrid waves at high and low frequency regions, respectively. The dispersion relation of the lower hybrid waves in hot plasma is written as

$$\omega^2 = k_\perp^2 v_s^2 + |\Omega_i \Omega_e| \tag{6.4}$$

where v_s is the sound speed which is defined as

$$v_s = \sqrt{\frac{\gamma_e T_e + \gamma_i T_i}{m_i}} \tag{6.5}$$

where γ_e and γ_i are so-called the ratio of specific heats of electrons and that of ions, respectively. Equation 6.4 indicates that the branch of lower hybrid waves asymptomatically approaches the line of $\omega = kv_s$. Assuming adiabatic compressions in the two-dimensional system, we can take for $\gamma_e = 1$ and $\gamma_i = 2$, then $v_s \simeq 0.3$ in the present simulations. In Figure 6.17, the branch of the low frequency waves asymptomatically approaches this line. We can conclude that these low frequency waves, propagating in the direction almost perpendicular to the ambient magnetic field, are the lower hybrid waves.

The energy decay process occurred through coupling between potentials drifting along the magnetic field and quasi-perpendicular lower hybrid waves are explained as follows. As shown in Figure 6.18, since lower hybrid waves propagate in the almost perpendicular direction, their parallel phase velocity $v_{\phi\parallel}$ is very large. Thus these waves couple with potentials drifting along the ambient magnetic field with large drift velocities v_d. Parallel potential energy decay into lower hybrid waves through this coupling process. To confirm this assumption, we calculate drift velocities of potentials and parallel phase velocities of the lower hybrid waves in this simulation. As demonstrated in the one-dimensional simulations in the previous chapter, drift velocities of potentials formed from the two-stream instability are almost equal to a half of the initial drift velocity of the electron beam ($v_d \simeq 2$). On the other hand, the frequencies of the lower hybrid waves are almost equal to 0.12 ($\omega_{LHR} \simeq 0.12$), as shown in Figure 6.17. According to the dispersion relation of the lower hybrid waves defined as Equation 6.4, the perpendicular wave number of the lower hybrid waves are calculated as 0.22 ($k_\perp \simeq 0.22$). The phase velocity of the lower hybrid waves in the direction perpendicular to the ambient magnetic field $v_{\phi\perp}$, therefore, is almost equal to 0.54 ($v_{\phi\perp} = \omega_{LHR}/k_\perp \simeq 0.54$). The lower hybrid waves are propagating in the direction not completely perpendicular to the ambient magnetic field. They are oblique propagating waves as already presented in Figure 6.12 in the previous section. Figure 6.12 shows $k_\parallel$-$k_\perp$ profile of potentials at $t = 97.77 \times T_{pe}$ in Run J. Oblique line indicates the line of $k_\perp/k_\parallel \sim 4$. We can find clear quasi-perpendicular waves almost on this line. These waves are the quasi-perpendicular lower hybrid waves coupling with potentials drifting along the magnetic field. The phase velocities of the lower hybrid waves in the direction parallel to the ambient magnetic field, therefore, are about four times of those in the perpendicular direction ($v_{\phi\parallel} \simeq v_{\phi\perp} \times 4$). As a result, the phase velocities of the lower hybrid waves in the parallel direction are about 2.2

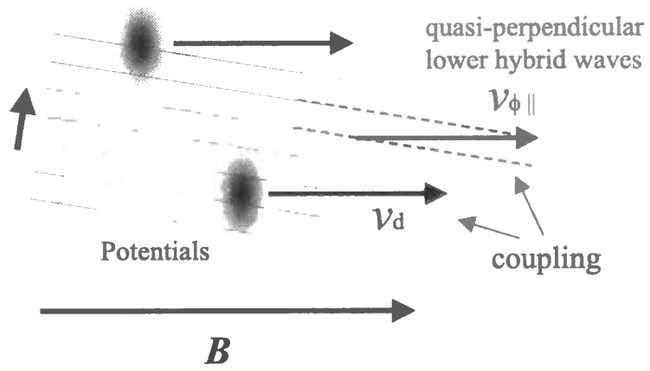

Figure 6.18: Schematic drawing of coupling between potentials drifting along the magnetic field and quasi-perpendicular lower hybrid waves.

($v_{\phi\parallel} \simeq 2.2$), which are almost equal to the drift velocities of the parallel drifting electrostatic potentials ($v_{\phi\parallel} \simeq v_d$). This result indicates that the electron hall potentials drifting along the magnetic field and the quasi-perpendicular lower hybrid waves are coupling with each other, and parallel potential energy decay to perpendicular lower hybrid waves through this coupling process.

During decay phase, the parallel drift energy of electron beams is decreasing and the perpendicular thermal energy of ions is increasing. Through this coupling process, the parallel drift energy of electron beams is also converted to the perpendicular thermal energy of ions.

6.5 Summary

In this chapter, we performed two-dimensional electrostatic particle simulations of the electron bump-on-tail instability and the electron two-stream instability. We confirmed the formation of the stable one-dimensional ESW in the bump-on-tail instability and the formation of the stable two-dimensional ESW in the warm two-stream instability owing to the ion dynamics. In this section, we summarize the results of these two-dimensional simulations, and present our conclusions of the generation mechanism of the one-dimensional ESW in the Earth's magnetotail and the two-dimensional ESW in the auroral region.

6.5.1 ESW formation in the Earth's magnetotail

The two-dimensional electrostatic particle simulations demonstrated that one-dimensional ESW, observed in the PSBL region of the Earth's magnetotail, can be formed from the electron bump-on-tail instability in the presence of some magnitudes of the ambient magnetic fields. The formation process of one-dimensional ESW are affected by the finite Larmor radius of electrons. In the simulation runs with weaker magnetic fields, ESW are much more coherent even in the initial state. This indicates that too strong magnetic field is not favorable for the formation of one-dimensional ESW. In the nonlinear stage, however, potentials are aligned in the perpendicular direction, forming uniform one-dimensional ESW due to the potential striation process, as shown in Figure 6.1.

It is difficult to estimate the lower and upper limits of the favorable magnitude of the magnetic field for ESW formation. This is because the formation process of ESW are critically subject to the diffusion by the enhanced thermal fluctuations. The perpendicular coherency of ESW at the saturation of the instability is also a function of the thermal fluctuations, which are much enhanced in the particle simulations, as stated in Section 4.2.

In the PSBL region, where ESW are frequently observed, the magnetic fields are very weak $\Omega_e/\Pi_e \sim 0.2$. According to the present analysis of the linear and nonlinear formation processes of ESW, we concluded that ESW can be formed with a magnetic field $\Omega_e/\Pi_e = 0.2$ or weaker in the real magnetotail plasma, where the thermal fluctuations are far less than those in particle simulations. ESW formed in such a weak magnetic field are expected to have very clear one-dimensional structure uniform in the direction perpendicular to the ambient magnetic field.

On the other hand, some ESW observed in the near Earth PSBL region are reported to have two-dimensional structures. In such near Earth PSBL region, the magnitude of the ambient magnetic field is larger than that in the distant magnetotail PSBL region. This is consistent with the above simulation results that not coherent potentials are excited in the case with a strong

magnetic field. These potentials, however, aligned in the perpendicular direction as time goes on, forming one-dimensional potentials. This is also consistent with the Geotail observations that most of ESW observed in the near Earth PSBL region still have one-dimensional structures uniform in the direction perpendicular to the ambient magnetic field. The tendency of the two-dimensional ESW observed by the Geotail spacecraft in the near Earth PSBL region based on our simulation results is investigated by *Kojima* [1998].

It is noted that the density ratio $R = 0.03$ is the minimum value with which we could find formation of ESW in the present particle simulations. In a run with a weaker electron beam, electrostatic potentials at saturation of the instability are very small, and they are diffused by the enhanced thermal fluctuations. The thermal fluctuations can be suppressed by increasing the number of superparticles in the simulation system. However, this requires larger memory area and longer computation time than available in the computer system used for the present study. Although the assumed density ratio may be larger than those observed in the PSBL region, we believe that the essential physical process of nonlinear evolutions of the bump-on-tail instability is successfully reproduced in the present simulation.

6.5.2 ESW formation in the auroral region

We performed two-dimensional electrostatic particle simulations of the electron two-stream instability, and confirmed that isolated two-dimensional structures, which are frequently observed in the auroral region, can be formed from the electron two-stream instability owing to the ion dynamics. The time evolution of potentials is summarized as follows. Large amplitude two-dimensional potentials are excited by the initial electron beam instability. After the saturation of the instability, they coalesce with each other and become isolated in the parallel direction. Then, these potentials are gradually aligned in the perpendicular direction, forming uniform one-dimensional potentials. These potentials, however, are divided in the perpendicular direction by quasi-perpendicular lower hybrid waves excited through coupling with potentials drifting along the ambient magnetic field, leading to formation of isolated two-dimensional potentials. In a long time evolution, these isolated two-dimensional potentials are gradually aligned in the perpendicular direction again. Finally they become one-dimensional potentials uniform in the direction perpendicular to the ambient magnetic field.

In the auroral region, where two-dimensional ESW are frequently observed, we can expect strong electron beams are drifting along the ambient magnetic field. When ion temperature is hot enough in comparison with electron temperature, such strong electron beam excite very strong instability, then isolated two-dimensional potentials are formed through coupling of electron hall potentials and quasi-perpendicular lower hybrid waves. We conclude that these isolated two-dimensional potentials are observed as two-dimensional ESW in the auroral region. In a long time evolution, however, these two-dimensional potentials are aligned in the perpendicular direction, forming stable one-dimensional potentials through the striation process. This suggests that the perpendicular spatial scale of the two-dimensional ESW becomes larger as time goes on. ESW will have more one-dimensional structures in a far region in comparison with those in a near region from their generation point. According to observations of two-dimensional ESW by the FAST and the Polar satellites, spatial scale of solitary waves in the perpendicular direction observed by the Polar satellite are larger than that observed by the FAST satellite. The Polar satellite observed two-dimensional ESW at radial distances of 2.02 to 8.5 R_E, and the FAST satellite observed two-dimensional ESW at much lower altitude,

the downward current regions of the mid-altitude auroral zone (~3000 km). This may indicate that the generation point of two-dimensional ESW in the auroral region are near the downward current regions of the mid-altitude auroral zone.

Chapter 7

Summary and Conclusions

7.1 Summary of the present study

This thesis investigated the formation mechanism of ESW via one- and two-dimensional electrostatic particle simulations. There are two types of ESW reported by satellite observations in different regions, in the Earth's magnetotail region and in the auroral region. These two ESW have different characteristics with respect to the spatial structure and the strength of the electric field. We confirmed these two types of ESW are generated by different electron beam instabilities by performing one- and two-dimensional electrostatic particle simulations. The followings are summaries of each chapter in the present thesis.

In Chapter 1, We presented a brief introduction of the present study and provided overviews of the Earth's magnetotail region and the auroral region, and plasma waves observed in each region. We also presented a review of BEN emissions. BEN has been observed by many satellites in many regions in space, and had been considered as "noise" by its broadband spectrum until BEN's waveform was observed by the Geotail spacecraft.

The Geotail spacecraft observed the waveform of BEN emission, and found they are composed of sequences of impulsive solitary waves. These impulsive solitary waves are termed ESW. In Chapter 2, we introduced two observations of ESW. One is observed by the Geotail spacecraft in the Earth's PSBL region, the other is observed by the FAST and the Polar satellites in the auroral region. The characteristics of ESW observed by the Geotail spacecraft are the weak electric fields and the one-dimensional spatial structure uniform in the direction perpendicular to the ambient magnetic field. On the other hand, the characteristics of ESW observed in the auroral region are the strong electric field and the two-dimensional spatial structure. The Geotail/PWI team proposed ESW potential model based on the Geotail/WFC data analyses that is the impulsive waveforms of ESW correspond to sequences of isolated electrostatic potentials traveling along the ambient magnetic field. According to the Geotail observations and previous simulation studies of electron beam instabilities, we proposed a generation model of ESW that the electrostatic potentials of ESW are stable BGK potentials, and these BGK potentials are generated through nonlinear evolutions of electron beam instabilities. We performed computer simulations to confirm our generation model of ESW.

Before performing computer simulations, we described linear and nonlinear theory of electron beam instabilities in Chapter 3. In this chapter, we defined the initial velocity distribution functions of electrons, the two-stream instability, the weak-beam instability and the bump-on-tail instability, which are referenced to the following one- and two-dimensional particle simulations. We analyzed linear dispersion relations of these electron beam instabilities, and discussed their parametric dependence on the magnitudes of the static magnetic fields and the propagation angles to the magnetic field. Then, we made a brief review of BGK equilibrium

and nonlinear trapping theory. Both of them are basic nonlinear theories in the present study.

To perform one- and two-dimensional electrostatic particle simulations efficiently, we developed a new electrostatic particle code based on KEMPO. In Chapter 4, we described this electrostatic particle code kuES2. This simulation code is specialized to one- and two-dimensional electrostatic particle simulations with a huge number of superparticles. In the present study, we performed one- and two-dimensional electrostatic particle simulations with kuES2. We also mention to two methods in parallelizing particle codes for parallel computers with multiple processors. In addition, we mentioned to effects of the enhanced thermal fluctuations in particle simulations. The thermal fluctuations are numerically enhanced in particle simulations, and affect simulation results, especially in the two-dimensional system, where oblique mode waves exist. We also explained the simulation systems and parameters used in the following one- and two-dimensional computer simulations.

In Chapter 5, we performed one-dimensional electrostatic particle simulations. At first, we performed one-dimensional simulations without ion dynamics of the above mentioned three typical electron beam instabilities, the two-stream instability, the weak-beam instability and the bump-on-tail instability. In these simulations, we confirmed that isolated electrostatic potentials are formed through nonlinear evolutions of the two-stream instability and the bump-on-tail instability. These potentials formed and balanced with trapped and untrapped electrons, and very stable for a long time. These stable potentials are BGK potentials, which is assumed as the stable potentials of ESW. We concluded that ESW can be excited through nonlinear evolutions of the two-stream instability and the bump-on-tail instability. The most clear difference is the strength of the electric fields between these two ESW. The electric fields of ESW excited by the two-stream instability are very strong, and those of ESW excited by the bump-on-tail instability are very weak.

Next, we further performed one-dimensional simulations with ion dynamics of the two-stream instability and the bump-on-tail instability, and estimated effects of the ion dynamics on the formation mechanism and the long time stability of ESW. We confirmed ESW formed from the two-stream instability are critically affected and tend to be diffused by the ion dynamics. On the other hand, ESW formed from the bump-on-tail instability are hardly affected by the ion dynamics.

Comparison between these results of the one-dimensional simulations and ESW observations of the Geotail spacecraft and those of the FAST and the Polar satellites lead us to the following conclusions. In the Earth's PSBL region, ESW are generated through the nonlinear evolutions of the bump-on-tail instability. While in the auroral region, ESW are generated through the nonlinear evolutions of the two-stream instability.

In Chapter 6, we performed two-dimensional electrostatic particle simulations of the electron two-stream instability and the electron bump-on-tail instability, and confirmed the spatial structures and the stability of ESW excited by these two electron beam instabilities in the two-dimensional system.

In Section 6.2, we performed two-dimensional simulations of the electron bump-on-tail instability as a generation mechanism of ESW in the Earth's PSBL region, and confirmed the formation of clear one-dimensional ESW. We examined three simulation runs without ion dynamics for different magnitudes of the ambient magnetic field, and estimated their effects on the formation mechanism and the stability of ESW. The strength of the magnetic field is a controlling parameter of the coherency of ESW in the direction perpendicular to the ambient magnetic field. In the simulation runs with weaker magnetic fields, ESW are much more coherent even in the initial state. In the nonlinear stage, however, potentials are aligned in the perpendicular direction, forming uniform one-dimensional potentials due to the potential striation process.

In the present simulations, though a weak magnetic field is favorable for the formation of one-dimensional ESW, we could not confirm the formation of ESW in the run with a very weak magnetic field. This is because the formation process of ESW is critically affected by the enhanced thermal fluctuations. Since ESW excited in the run with a very weak magnetic field have smaller potentials than those in the run with a stronger magnetic field, they are easily diffused due to the enhanced thermal fluctuations. The analysis of the linear and nonlinear formation processes of ESW indicated that very clear one-dimensional ESW can be formed with a very weak magnetic field in the real magnetotail plasma, where the thermal fluctuations are far less than those in the present simulations.

These simulation results are consistent with the Geotail observations that the clear one-dimensional ESW are observed in the Earth's magnetotail PSBL region, where the magnitude of the magnetic field is very weak. In addition, these are also consistent with the recent observations of the two-dimensional ESW in the near Earth PSBL region, where the magnitude of the magnetic field is relatively large.

In Section 6.3, we performed two-dimensional simulations of the electron two-stream instability as a generation mechanism of ESW in the auroral region, and confirmed the formation of isolated two-dimensional ESW. At first, we performed four simulation runs without ion dynamics for different parameters, the temperature of the electron beams and the magnitude of the ambient magnetic field. In these simulations, we confirmed clear potential structures in runs with a strong magnetic field. ESW excited from the two-stream instability formed by cold electron beams have isolated two-dimensional structures due to the existence of the quasi-perpendicular electrostatic whistler waves. In a long time evolution, however, these two-dimensional potentials gradually decay to the electrostatic whistler mode waves. On the other hand, ESW excited from the warm two-stream instability have one-dimensional structure. This is because the quasi-perpendicular whistler waves are subject to the Landau damping.

Further, we performed simulation runs with ion dynamics, and isolated two-dimensional ESW are formed from the warm electron two-stream instability. In the simulation run of the warm electron two-stream instability with ion dynamics, the quasi-perpendicular lower hybrid waves are excited through coupling with parallel drifting potentials. These lower hybrid waves separate potentials in the direction perpendicular to the ambient magnetic field, leading to the formation of isolated two-dimensional potentials. These potentials are very stable for a long time, and their spatial scale is almost equal to the Larmor radius of ions. These natures of the isolated two-dimensional potentials are consistent with the observations of ESW in the auroral region. In a long time evolution, however, these isolated two-dimensional potentials are gradually aligned in the perpendicular direction again due to the potential striation process. This suggests that the perpendicular spatial scale of the two-dimensional ESW becomes larger as time goes on. ESW will have more one-dimensional structures in a far region in comparison with those in a near region from their generation point.

7.2 Conclusions

BEN emissions were first observed in the Earth's magnetotail region by the IMP 8 spacecraft in 1976 [*Gurnett et al.*, 1976]. From this time, many satellites have observed similar broadband emissions and many scientists have tried to explain generation mechanisms of such broadband "noise". Most of them considered BEN emissions were generated via ion beam driven instabilities. However, the waveform observation by the Geotail spacecraft revealed the waveform of BEN emissions are not continuous "noise", but are composed of sequences of impulsive solitary waves, which are termed ESW. The impulsive waveforms of ESW correspond to sequences of isolated electrostatic potentials. This indicates that stable electrostatic potentials exist in the real space plasma.

Meanwhile, one-dimensional computer simulations of electron beam instabilities were first performed with Vlasov code in 1967 [*Berk and Roberts*, 1967]. In this simulation result, the formation of a clear vortex in x-v_x phase space, which corresponds to a electrostatic potential, is confirmed. From this time, many simulations of electron beam instabilities have been performed, and found the formation of similar potential structures. In addition, such potential structures were already confirmed in laboratory plasma [*e.g.*, *Saeki et al.*, 1979].

It is easily understood that such isolated electrostatic potentials correspond to impulsive spikes of the electric field, and that these spiky electric field have broadband spectra in frequency space. However, no one had combined these spiky electric fields and the broadband spectra of BEN emissions, until the Geotail observation revealed the spiky waveforms of BEN emissions in 1994 [*Matsumoto et al*, 1994b]. This is because such clear electrostatic potentials are considered to be unstable in the real space plasma where the magnetic field is weak and the plasma environment rapidly changes. The Geotail observations and the simulation results of the present study, however, demonstrated that stable electrostatic potentials can exist in the real space plasma, and the electron beam instabilities are frequently taking place in various regions of the Earth's magnetosphere, e.g., in the PSBL region.

The present simulation study also demonstrated that stable electrostatic potentials are excited by even a very weak electron beam in space plasma. In the electron bump-on-tail instability, since the modulations of electrons is limited in phase space, the initial instability saturate in a relatively short time, and nonlinear evolutions of potentials form stable BGK potentials through coalescence. In one-dimensional computer simulations, we further investigated parametric dependence of these electrostatic potentials on the ion dynamics. These simulations are the first attempt in terms of explaining the relation between the spiky waveforms of BEN emissions and the correspondingly observed high-energy ion flows.

The analysis of the long time evolutions of electrostatic potentials in two-dimensional system is, of course, a new approach in space plasma physics. Especially, the potential striation process in the direction perpendicular to the ambient magnetic field and the coupling process of potentials drifting along the magnetic field and quasi-perpendicular lower hybrid waves are new findings. Due to the potential striation process, the spatial scale of ESW in the perpendicular direction become larger, as time goes on. In other words, the perpendicular spatial scale of ESW are related to the distance from their generation points. Some statistical Geotail/WFC data analyses of the perpendicular spatial scale of ESW based on this simulation result are conducted by *Kojima* [1998] and *Omura et al* [1999b]. The results of these statistical analyses indicate the possibility of using the characteristics of ESW in remote sensing of particle acceleration

processes such as a magnetic reconnection and a shock formation.

On the other hand, the coupling process of potentials and lower hybrid waves is a new nonlinear physical process in plasma physics. Most of all the coupling processes in plasma physics are either wave-wave coupling or wave-particle coupling. While this coupling process is that of spatially isolated potentials and waves. Though the coupling process itself is very simple and easy to understand, this simulation study is the first finding and presenting of the coupling of waves and neither waves nor particles but electron hall potentials. This indicates that particle simulations are very useful in investigating a new aspect of nonlinear plasma physics.

7.3 Future works

Electromagnetic simulations

In the present study, all the simulations are performed based on the electrostatic approximation. Since ESW are revealed to be purely electrostatic waves, the generation mechanism of ESW should be expressed as electrostatic processes. In a long time evolution, however, it is enough possible that such solitary structures of potentials radiate some electromagnetic waves, and solitary structures, which are stable in the electrostatic environment, are diffused through such the radiation process. Especially, the isolated two-dimensional ESW in the auroral region are able to become sources of some electromagnetic radiations emitted from that region, for example, Auroral Kilometric Radiation (AKR), Auroral Myriametric Radiation (AMR) and some other waves. We have to perform electromagnetic particle simulations of long time evolutions of the electron beam instabilities in the near future.

Technical development

In two-dimensional computer simulations, we have two technical problems in terms of restrictions of memory area and calculating time. One is coarse spatial resolution, which gives rise to numerical damping of electric fields. This attenuation is suspected to affect the stability of ESW critically. The other is a limited number of superparticles, which gives rise to the enhanced thermal fluctuations as discussed in Sections 4.2 and 6.4. Currently we use 34 millions superparticles in the two-dimensional simulation system, but this is not sufficient to suppress the thermal fluctuation. These two problems are related to each other. For example, if we increase grid points, the number of superparticles in one grid of the simulation system is decreased and the thermal fluctuations are enhanced.

Two-dimensional Vlasov code In the present study, we could not ignore numerical thermal fluctuation, which may suppress plasma phenomena with weak amplitudes. We cannot avoid this fluctuation as far as using particle code. Two-dimensional Vlasov code is a very effective tool to suppress numerical thermal fluctuation drastically. In this code, Vlasov equation and Poisson's equation are self-consistently solved. Since all the variables used in this code are Eulerian, which are defined on the fixed spatial grid points, vectorization and parallelization would work very effectively in performing simulations by this code. Although a very huge memory area is also necessary, this is expected to be a very effective tool for analysis of various

plasma phenomena, especially such phenomena that are critically affected by the enhanced thermal fluctuation.

Boundary condition Since the boundary condition is taken as periodic, one-dimensional ESW in the simulation system correspond to those with infinite width in the perpendicular direction. In the real space, however, any potential cannot have infinite structure, and must be localized. In studying the stability of the localized potential structure, it is very important to include the effects of the boundary condition in the perpendicular direction. We will have to study differences due to the boundary condition by performing computer simulations with another boundary condition, such as a free boundary condition. In such simulation runs, we need a large simulation system in the perpendicular direction.

References

[1] Akasofu, S. -I., and Y. Kamide, The Aurora, in *The Solar Wind and the Earth*, p. 143, Terra Scientific Publishing Company, 1987.

[2] Akimoto, K., and N. Omidi, The generation of broadband electrostatic noise by an ion beam in the magnetotail, *Geophys. Res. Lett., 13*, 97, 1986.

[3] Akimoto, K., Y. Omura, and H. Matsumoto, Rapid generation of Langmuir wave packets during electron beam-plasma instabilities, *Phys. Plasmas, 3*, 2556, 1996.

[4] Akiyama, Y., K. Misoo, Y. Omura, H. Matsumoto, M. Saito, T. Noguchi, and K. Onizuka, Parallelization of Space Plasma Particle Simulation (in Japanese), *High-performance Computing, 66*, 1, 1997.

[5] Albert, R. D., and P. J. Lindstrom, auroral-particle precipitation and trapping caused by electrostatic double layers in the ionosphere, *Science, 170*, 1398, 1970.

[6] Anderson, R. R., C. C. Harvey, M. M. Hoppe, B. T. Tsurutani, T. E. Eastman, and J. Etcheto, Plasma waves near the magnetopause, *J. Geophys. Res., 87*, 2087, 1982.

[7] Ashour-Abdalla, M., and H. Okuda, Electron acoustic instabilities in the geomagnetic tail, *Geophys. Res. Lett., 13*, 366, 1986a.

[8] Ashour-Abdalla, M., and H. Okuda, Theory and simulations of broadband electrostatic noise in the geomagnetic tail, *J. Geophys. Res., 91*, 6833, 1986b.

[9] Baker, D. N., S. J. Bame, J. Birn, W. C. Feldman, J. T. Gosling, E. W. Hones, Jr., R. D. Zwickl, J. A. Slavin, E. J. Smith, B. T. Tsurutani, and D. G. Sibeck, *Geophys. Res. Lett., 10*, 1042, 1984.

[10] Bame, S. J., J. R. Asbridge, H. F. Felthauser, E. W. Hones, Jr., and I. B. Strong, Characteristics of the plasma sheet in the Earth's magnetotail, *J. Geophys. Res., 72*, 113, 1967.

[11] Berk, H. L., and K. V. Roberts, Nonlinear Study of Vlasov's Equation for a Special Class of Distribution Functions, *Phys. Fluids, 10*, 1595, 1967.

[12] Berk, H. L., C. E. Nielsen, and K. V. Roberts, Phase space hydrodynamics of equivalent nonlinear systems: Experimental and computational observations, *Phys. Fluids, 13*, 980, 1970.

[13] Bernstein, I. B., J. M. Greene, and M. D. Kruskal, Exact nonlinear plasma oscillations, *Phys. Rev., 108*, 546, 1957.

[14] Bernstein, I. B., Waves in a plasma in a magnetic field, *Phys. Rev., 109*, 10, 1958.

[15] Berthomier, M., R. Pottelette, and M. Malingre, Solitary waves and weak double layers in a two-electron temperature auroral plasma, *J. Geophys. Res., 103*, 4261, 1998.

[16] Boström, R., G. Gustafsson, B. Holback, G. Holmgren, H. Koskinen, and P. Kintner, Characteristics of solitary waves and weak double layers in the magnetospheric plasma, *Phys. Rev. Lett., 61*, 82, 1988.

[17] Borovsky, J. E., Properties and dynamics of the electron beams emanating from magnetized plasma double layers, *J. Geophys. Res., 93*, 5713, 1988.

[18] Borovsky, J. E., Double layers do accelerate particles in the auroral zone, *Phys. Rev. Lett., 69*, 1054, 1992.

[19] Borovsky, J. E., The Strong-Double-Layer Model of Auroral Arcs: An Assessment, in *Auroral Plasma Dynamics, AGU Monograph, 80*, p. 113, 1993.

[20] Bryant, D. A., D. S. Hall, and D. R. Lepine, Electron acceleration in an array of aurora arcs, *Planet. Space Sci., 26*, 81, 1978.

[21] Burch, J. L., Diagnosis of auroral acceleration mechanisms by particle measurements, in *Auroral physics*, p. 97, Cambridge University Press, 1991.

[22] Burinskaya, T. M., and C. -V. Meister, Contribution of the ion-beam acoustic instability to the generation of broadband electrostatic noise in the earth's magnetotail, *Planet. Space Sci., 37*, 145, 1989.

[23] Burinskaya, T. M., and C. -V. Meister, Contribution of the ion-beam acoustic instability to the generation of broadband electrostatic noise -Three dimensional quasilinear approach-, *Planet. Space Sci., 38*, 695, 1990.

[24] Cattell, C. A., and F. S. Mozer, Experimental determination of the dominant wave mode in the active near-earth magnetotail, *Geophys. Res. Lett., 13*, 221, 1986.

[25] Chapman, S., The absorption and dissociative or ionizing effect of monochromatic radiation in an atmosphere on rotating Earth, *Proc. Phys. Soc., 43*, 26, 1931.

[26] Chapman, S., and V. C, A. Ferraro, A new theory of magnetic storms, *Terr. Magn. Atmos. Electro., 36*, 77, 1931.

[27] Cowley, S. W. H., R. J. Hynds, I. G. R. Richardson, P. W. Daly, T. R. Sanderson, K. P. Wenzel, J. A. Slavin, and B. T. Tsurutani, Energetic ion regions in the deep geomagnetic tail: ISEE-3, *Geophys. Res. Lett., 11*, 275, 1984.

[28] DeCoster, R. J., and L. A. Frank, Observations pertaining to the dynamics of the plasma sheet, *J. Geophys. Res., 84*, 5099, 1979.

[29] Dovner, P. O., A. I. Eriksson, R. Boström, and B. Holback, Freja multiprobe observations of electrostatic solitary structures, *Geophys. Res. Lett., 21*, 1827, 1994.

[30] Dubouloz, N., R. Pottelette, M. Malingre, and R. A. Treumann, Generation of broadband electrostatic noise by electron acoustic solitons, *Geophys. Res. Lett., 18*, 155, 1991a.

[31] Dubouloz, N., R. Pottelette, M. Malingre, G. Holmgren, and P. A. Lindqvist, Detailed analysis of broadband electrostatic noise in the dayside auroral zone, *J. Geophys. Res., 96*, 3565, 1991b.

[32] Dubouloz, N., R. A. Treumann, R. Pottelette, and M. Malingre, Turbulence generated by a gas of electron acoustic solitons *J. Geophys. Res., 98*, 17415, 1993.

[33] Dupree, T. H., Theory of phase-space density holes, *Phys. Fluids, 25*, 277, 1982.

[34] Dusenbery, P. B., and L. R. Lyons, The generation of electrostatic noise in the plasma sheet boundary layer, *J. Geophys. Res., 90*, 10935, 1985.

[35] Dusenbery, P. B., Generation of broadband noise in the magnetotail by the beam acoustic instability, *J. Geophys. Res., 91*, 12005, 1986.

[36] Ergun, R. E., C. W. Carlson, J. P. McFadden, F. S. Mozer, G. T. Deloy, W. Peria, C. C. Chaston, M. Temerin, I. Roth, L. Muschietti, R. Elphic, R. Strangeway, R. Pfaff, C. A. Cattell, D. Klumpar, E. Shelley, W. Peterson, E. Moebius, and L. Kistler, FAST satellite observations of large-amplitude solitary structures, *Geophys. Res. Lett., 25*, 2041, 1998.

[37] Eriksson, A. I., A. Mälkki, P. O. Donver, R. Boström, G. Holmgren, and B. Holback, A statistical survey of auroral solitary waves and weak double layers, 2. Measurement accuracy and ambient plasma density, *J. Geophys. Res., 102*, 9821, 1997.

[38] Evans, D. S., Evidence for the low altitude acceleration of auroral particles, in *Physics of Hot Plasma in the Magnetosphere*, Plenum, 1975.

[39] Feldman, W. C., S. J. Schwartz, S. J. Bame, D. N. Baker, J. Birn, J. T. Gosling, E. W. Hones, Jr., D. J. McComas, J. A. Slavin, E. J. Smith, and R. D. Zwickl, Evidence for Slow-Mode Shocks in the Deep Geomagnetic Tail, *Geophys. Res. Lett., 11*, 599, 1984.

[40] Fennel, R. N., R. R. Mackinley, P. D. Edgley, and D. N. Wall, Non linear behavior of a finite amplitude electron plasma wave, III The sideband instability, *Proc. R. Soc. Lond., A360*, 229, 1981.

[41] Fox, G. C., R. D. Williams, and P. C. Messina, Parallel Computing Works!, in *Plasma Particle-in-Cell Simulations of and Electron Beam Plasma Instability*, 1994.

[42] Frank, L. A., K. L. Ackerson, and R. P. Lepping, On hot tenuous plasmas, fireballs, and boundary layers in the Earth's magnetotail, *J. Geophys. Res., 81*, 6059, 1976.

[43] Franz, J. R., P. M. Kintner, J. S. Pickett, POLAR observations of coherent electric field structures, *Geophys. Res. Lett., 25*, 1277, 1998.

[44] Fukunishi, H., Plasma Wave Phenomena in the Earth's Magnetosphere, in *The Solar Wind and the Earth*, p. 185, Terra Scientific Publishing Company, 1987.

[45] Goldman, M. V., M. M. Oppenheim, and D. L. Newman, Nonlinear two-stream instabilities as an explanation for auroral bipolar wave structures, *Geophys. Res. Lett., 26*, 1821, 1999.

[46] Grabbe, C. L., and T. E. Eastman, Generation of broadband electrostatic noise by ion beam instabilities in the magnetotail, *J. Geophys. Res., 89*, 3865, 1984.

[47] Grabbe, C. L., New results on the generation of broadband electrostatic noise by ion beam instabilities in the magnetotail, *Geophys. Res. Lett., 12*, 483, 1985.

[48] Grabbe, C. L., Numerical study of the spectrum of broadband electrostatic noise in the magnetotail, *J. Geophys. Res., 92*, 1185, 1987.

[49] Grabbe, C. L., Wave propagation effects of broadband electrostatic noise in the magnetotail, *J. Geophys. Res., 94*, 17299, 1989.

[50] Gurnett, D. A., L. A. Frank, and R. P. Lepping, Plasma waves in the distant magnetotail, *J. Geophys. Res., 81*, 6059, 1976.

[51] Heikkila, W. J., Satellite observations of soft particle fluxes in the auroral zone, *Nature, 225*, 369, 1970.

[52] Hoffman, R. A., and D. S. Evans, Field-aligned electron bursts at high latitudes observed by OGO 4, *J. Geophys. Res., 73*, 6201, 1968.

[53] Huba, J. D., N. T. Gladd, and K. Papadopolous, Lower hybrid drift wave turbulence in the distant magnetotail, *J. Geophys. Res., 83*, 5217, 1978.

[54] Hudson, M. K., W. Lotko, I. Roth, and E. Witt, Solitary waves and double layers on auroral field lines, *J. Geophys. Res., 88*, 916, 1983.

[55] Hwang, K. S, N. H. Stone, K. H. Wright, Jr., and U. Samir, The emissions of broadband electrostatic noise in the near vicinity of the shuttle orbiter, *Planet. Space Sci., 35*, 1372, 1987.

[56] Kadomtsev, B. G., Collective Phenomena in Plasmas, Nauka, 1976.

[57] Karpman, V. I., Ja. N. Istomin, and D. R. Shklyar, Effects of nonlinear interaction of monochromatic waves with resonant particles in the inhomogeneous plasma, *Physica Scripta, 11*, 278, 1975.

[58] King, J. H., Additional spacecraft data sources contributing to the ISTP program, *Adv. Space Res., 20*, 595, 1997.

[59] Knorr, G., and C. K. Goertz, Existence and stability of strong potential double layers, *Astrophys. Space Sci., 31*, 209, 1974.

[60] Kojima, H., H. Matsumoto, T. Miyatake, I. Nagano, A. Fujita, L. A. Frank, T. Mukai, W. R. Paterson, and R. R. Anserson, Relation between Electrostatic Solitary Waves and hot plasma flow in the plasma sheet boundary layer: GEOTAIL Observations, *Geophys. Res. Lett., 21*, 2919, 1994.

[61] Kojima, H., H. Matsumoto, S. Chikuba, S. Horiyama, M. Ashour-Abdalla, and R. R. Anderson, Geotail waveform observations of broadband/narrowband electrostatic noise in the distant tail, *J. Geophys. Res., 102*, 14439, 1997.

[62] Kojima, H., H. Matsumoto, and Y. Omura, Electrostatic solitary waves observed in the geomagnetic tail and other regions, *Advanced Space Research, 23*, 1689, 1998.

[63] Kojima, H., Study on the Plasma Waves in the Geomagnetic Tail Region, Ph.D. thesis, Dep. of Electr. Eng., Kyoto Univ., Kyoto, Japan, 1998.

[64] Koskinen, H. E. J., R. Boström, and B. Holback, Viking observations of solitary waves and weak double layers on auroral field lines, *Phys. of Space Plasmas, SPI conference proceedings and reprints series, 7*, 147, 1987.

[65] Koskinen H. E. J., R. Lundin, and B. Holback, On the plasma environment of solitary waves and weak double layers, *J. Geophys. Res., 95*, 5921, 1990.

[66] Krasovsky, V. L., H. Matsumoto, and Y. Omura, Bernstein-Green-Kruskal analysis of electrostatic solitary waves observed with Geotail, *J. Geophys. Res., 102*, 22131, 1997.

[67] Krasovsky, V. L., H. Matsumoto, and Y. Omura, Interaction of Small Phase Density Holes, *Physica Scripta, 60*, 438, 1999.

[68] Lakhina, G. S., and B. T. Tsurutani, A generation mechanism for the polar cap boundary layer broadband plasma waves, *J. Geophys. Res., 104*, 279, 1999.

[69] Lepine, D. R., D. A. Bryant, and D. S. Hall, *Proc. 7th annual meeting on upper atmosphere studies by optical methods*, University of Tromso, p. 8, 1979.

[70] Liewer, P. C., and V. K. Decyk, A general concurrent algorithm for plasma particle-in-cell simulation codes, *J. Comput. Phys., 85*, 302, 1989

[71] Lotko, W., and C. F. Kennel, Spiky ion acoustic waves in collisionless auroral plasma, *J. Geophys. Res., 88*, 381, 1983.

[72] Lui, A. T. Y., Magnetotail physics, The Johns Hopkins university press, 1987.

[73] Mälkki, A., H. Koskinen, R. Boström, and B. Holback, On theories attempting to explain observations of solitary waves and weak double layers in the auroral magnetosphere, *Physica Scripta, 39*, 787, 1989.

[74] Mälkki, A., A. I. Eriksson, P. O. Dovner, R. Boström, B. Holback, G. Holmgren, and H. Koskinen, A statistical survey of auroral solitary waves and weak double layers 1. Occurrence and net voltage, *J. Geophys. Res., 98*, 15521, 1993.

[75] Mälkki, A., and R. Lundin, Altitude distributions of upward flowing ion beams and solitary structures in the Viking data, *Geophys. Res. Lett., 21*, 2243, 1994.

[76] Marchenko, V. A., and M. K. Hudson, Beam-driven acoustic solitary waves in the auroral acceleration region, *J. Geophys. Res., 100*, 19791, 1995.

[77] Matsumoto, H., and Y. Omura, Particle Simulation of Electromagnetic Waves and Its Application to Space Plasma, in *Computer Simulation of Space Plasma*, p. 43, Terra Scientific Publishing Company, 1984.

[78] Matsumoto, H., Coherent nonlinear effects on electromagnetic wave-particle interactions, in *Space Plasma Simulations*, p. 429, D. Reidel Publishing Company, 1985.

[79] Matsumoto, H., I. Nagano, R. R. Anderson, H. Kojima, K. Hashimoto, M. Tsutsui, T. Okada, I. Kimura, Y. Omura, and M. Okada, Plasma Wave Observations with GEOTAIL Spacecraft, *J. Geomag. Geoelectr., 46*, 59, 1994a.

[80] Matsumoto, H., H. Kojima, T. Miyatake, Y. Omura, M. Okada, I. Nagano, and M. Tsutsui, Electrostatic Solitary Waves (ESW) in the Magnetotail: BEN wave forms observed by GEOTAIL, *Geophys. Res. Lett., 21*, 2915, 1994b.

[81] Matsumoto, H., H. Kojima, Y. Kasaba, T. Miyake, R. R. Anderson, and T. Mukai, Plasma waves in the upstream and bow shock regions observed by GEOTAIL, *Advanced Space Research, 20*, 683, 1997.

[82] Matsumoto, H., H. Kojima, Y. Omura, and I. Nagano, Plasma waves in geospace: Geotail observations, in *New perspectives on the Earth's magnetotail, AGU Monograph, 105*, p. 261, 1998.

[83] Matsumoto, H., L. A. Frank, Y. Omura, H. Kojima, W. R. Paterson, M. Tsutsui, R. R. Anderson, S. Horiyama, S. Kokubun, and T. Yamamoto, Generation Mechanism of ESW based on GEOTAIL Plasma Wave Observation, Plasma Observation and Particle Simulation, *Geophys. Res. Lett., 26*, 421, 1999.

[84] McEwen, D. J., E. Yee, B. A. Whalen, and A. W. Yau, Electron energy measurements in pulsating auroras, *Can. J. Phys., 59*, 1106, 1970.

[85] McPherron, R. L., Physical processes producting magnetospheric substorms and magnetic storms, in *Geomagnetism Vol. 4*, p. 593, Academic Press, 1991.

[86] Miyake, T., Y. Omura, H. Matsumoto, and H. Kojima, Two-dimensional computer simulations of electrostatic solitary waves observed by Geotail spacecraft, *J. Geophys. Res., 103*, 11841, 1998.

[87] Miyake, T., Y. Omura, H. Matsumoto and H. Kojima, Electrostatic particle simulations of solitary waves in the auroral region, *submitted to J. Geophys. Res.*, 1999.

[88] Morse, R. L., and C. W. Nielson, Numerical simulation of warm two-beam plasma, *Phys. Fluids, 12*, 2418, 1969.

[89] Mozer, F. S., C. A. Cattell, M. K. Hudson, R. L. Lysak, M. Temerin, and R. B. Torbert, Satellite measurements and theories of low altitude auroral particle acceleration, *Space Sci. Rev., 27*, 155, 1980.

[90] Mozer, F. S., R. Ergun, M. Temerin, C. Cattell, J. Dombeck, and J. Wygant, New features of time domain electric-field structures in the auroral acceleration region, *Phys. Rev. Lett., 79*, 1281, 1997.

[91] Mukai, T., S. Machida, Y. Saito, M. Hirahara, T. Terasawa, N. Kaya, T. Obara, M. Ejiri, and A. Nishida, The low energy particle (LEP) experiment onboard the Geotail Satellite, *J. Geomag. Geoelectr., 46*, 669, 1994.

[92] Nagai, T., R. Nakamura, T. Mukai, T. Yamamoto, A. Nishida, and S. Kokubun, Substorms, tail flows and plasmoids, *Adv. Space Res., 20*, 961, 1997

[93] Nagai, T., M. Fujimoto, Y. Saito, S. Machida, T. Terasawa, R. Nakamura, T. Yamamoto, T. Mukai, A. Nishida, and S. Kokubun, Structure and dynamics of magnetic reconnection for substorm onsets with Geotail observations, *J. Geophys. Res., 103*, 4419, 1998.

[94] Ness, N. F., The Earth's magnetic tail, *J. Geophys. Res., 70*, 2989, 1965.

[95] Nicholson, D. R., Introduction to Plasma Theory, John Wiley & Sons, 1983.

[96] Nishida, A., T. Hada, K. A. Anderson, R. R. Anderson, S. J. Bame, and E. W. Hones, Jr., Broadband electrostatic noise in the magnetotail; Its relation to plasma sheet dynamics, *J. Geophys. Res., 90*, 4453, 1985.

[97] Nishida, A., T. Mukai, T. Yamamoto, Y. Saito, and S. Kokubun, Magnetotail convection in geomagnetically active times, 1. Distance to the neutral lines, *J. Geomag. Geoelectr., 48*, 489, 1996.

[98] Okuda, H., Introduction to Particle Simulation Models and Other Application to Electrostatic Plasma Waves, Computer Simulation of Space Plasma, in *Computer Simulation of Space Plasma*, p. 3, Terra Scientific Publishing Company, 1984.

[99] Omholt, A., Studies on the excitation of aurora borealis II, *Geophys. Publ., 21*, 1, 1959.

[100] Omidi, N., Broadband electrostatic noise produced by ion beams in the Earth's magnetotail, *J. Geophys. Res., 90*, 12330, 1985.

[101] Omura, Y., Study on Nonlinear Wave-Particle Interactions in Space Plasma via Computer Simulations, Ph.D. thesis, Dep. of Electr. Eng., Kyoto Univ., Kyoto, Japan, 1985.

[102] Omura, Y., and H. Matsumoto, KEMPO1: Technical guide to one-dimensional electromagnetic particle code, in *Computer Space Plasma Physics*, p. 21, Terra Scientific Publishing Company, 1993.

[103] Omura, Y., H. Kojima, and H. Matsumoto, Computer simulation of electrostatic solitary waves: A nonlinear model of broadband electrostatic noise, *Geophys. Res. Lett., 21*, 2923, 1994.

[104] Omura, Y., H. Matsumoto, T. Miyake, and H. Matsumoto, Electron beam instabilities as generation mechanism of electrostatic solitary waves in the magnetotail, *J. Geophys. Res., 101*, 2685, 1996.

[105] Omura, Y., H. Kojima, N. Miki, T. Mukai, H. Matsumoto, and R. Anderson, Electrostatic solitary waves carried by diffused electron beam observed by the Geotail spacecraft, *J. Geophys. Res., 104*, 14627, 1999a.

[106] Omura, Y., H. Kojima, N. Miki, and H. Matsumoto, Two-dimensional Electrostatic Solitary Waves Observed by GEOTAIL in the Magnetotail, *Advanced Space Research, 24*, 55, 1999b.

[107] Onsager, T. G., M. F. Thomsen, J. T. Gosling, and S. J. Bame, Electron distributions in the plasma sheet boundary layer: Time-of-flight effects, *Geophys. Res. Lett., 17*, 1837, 1990.

[108] Onsager, T. G., M. F. Thomsen, R. C. Elphic, J. T. Gosling, R. R. Anderson, and G. Kettmann, Electron generation of electrostatic waves in the plasma sheet boundary layer, *J. Geophys. Res., 98*, 15509, 1993.

[109] Parker, E. N., Dynamics of interplanetary gas and magnetic field, *Astrophys. J., 128*, 664, 1958.

[110] Parks, G. K., M. McCarthy, R. J. Fitzenreiter, J. Etcheto, K. A. Anderson, R. R. Anderson, T. E. Eastman, L. A. Frank, D. A. Gurnett, C. Huang, R. P. Lin, A. T. Y. Lui, K. W. Oglivie, A. Pedersen, H. Reme, and D. J. Williams, Particle and field characteristics of the high-latitude plasma sheet boundary layer, *J. Geophys. Res., 89*, 8885, 1984.

[111] Petschek, H. E., Magnetic Field Annihilation, *AAS-NASA Symposium on the Physics of Solar Flares*, NASA Spec. Pun. SP-50, p. 425, 1964.

[112] Pottelette, R., M. Malingre, N. Dubouloz, B. Aparicio, R. Lundin, G. Holmgren, and G. Marklund, High-frequency waves in the cusp/cleft regions, *J. Geophys. Res., 95*, 5957, 1990.

[113] Saeki, K., P. Michelsen, H. L. Pécseli, and J. Juul Rasmussen, Formation and Coalescence of Electron Soliatry Holes, *Phys. Rev. Lett., 42*, 501, 1979.

[114] Scarf, F. L., L. A. Frank, K. L. Ackerson, and R. P. Lepping, Plasma wave turbulence associated with the Earth's bow shock, *Geophys. Res. Lett., 1*, 189, 1974.

[115] Scarf, F. L., F. V. Coroniti, C. F. Kennel, E. J. Smith, J. A. Slavin, B. T. Tsurutani, S. J. Bame, and W. C. Feldman, Plasma Wave Spectra Near Slow Mode Shocks in the Earth's Magnetotail, *Geophys. Res. Lett., 11*, 1050, 1984.

[116] Schriver, D. and M. Ashour-Abdalla, Generation of high-frequency broadband electrostatic noise: The role of cold electrons, *J. Geophys. Res., 92*, 5807, 1987.

[117] Schriver, D. and M. Ashour-Abdalla, Broadband electrostatic noise due to field-aligned currents, *Geophys. Res. Lett., 16*, 899, 1989.

[118] Schriver, D. and M. Ashour-Abdalla, Cold plasma heating in the plasma sheet boundary layer: Theory and simulations, *J. Geophys. Res., 95*, 3987, 1990.

[119] Slavin, J. A., and Y. Kamide, Solar wind-magnetosphere coupling: Introduction, in *Solar wind-magnetosphere coupling*, p. 9 Terra Scientific Publishing Company, 1986

[120] Speiser, T. W., Geomagnetic tail, *Geomagnetism Vol. 4*, Academic Press, 1991.

[121] Shawhan, S. D., G. B. Murphy, and J. S. Picket, Plasma diagnostics package assessments of the STS-3 Orbiter plasma environment, *J. Spacecraft Rockets, 21*, 387, 1984.

[122] Temerin, M., K. Cerny, W. Lotko, and F. S. Mozer, Observations of double layers and solitary waves in the auroral plasma, *Phys. Rev. Lett., 48*, 1175, 1982.

[123] Tsurutani, B. T., G. S. Lakhina, C. M. Ho, J. K. Arballo, C. Galvan, A. Boonsiriseth, J. S. Pickett, D. A. Gurnett, W. K. Peterson, and R. M. Thorne, Broadband plasma waves observed in the polar cap boundary layer: Polar, *J. Geophys. Res., 103*, 17351, 1998.

[124] Tsutsui, M., R. J. Strangewy, B. T. Tsurutani, H. Matsumoto, J. L. Phillips, and M. Ashour-Abdalla, Wave mode identification of electrostatic noise observed with ISEE 3 in the deep tail boundary layer, *J. Geophys. Res., 96*, 14065, 1991.

[125] Ueda, H., Y. Omura, H. Matsumoto, and T. Okuzawa, A study of the numerical heating in electrostatic particle simulations, *Comput. Phys. Commun., 79*, 249, 1994.

[126] Ueda, Y., Y. Omura, H. Usui, and H. Matsumoto, Electromagnetic Particle Simulations via Parallel Virtual Machines, *Proc. 5th Int'l Symposium/School for Space Simulations*, p. 399, 1997.

[127] Ueki, T., Study of Linear Dispersion Relation of Space Plasma Waves (in Japanese), Master Thesis, Dep. of Electr. Eng., Kyoto Univ., Kyoto, Japan, 1987.

[128] Wygant, J. R., M. Bensadoun, and F. S. Mozer, Electric field measurements at subcritical, oblique bow shock crossings, *J. Geophys. Res., 92*, 11109, 1987.

Publication list

Refereed Journals

1. Omura, Y., H. Matsumoto, T. Miyake, and H. Kojima, Electron beam instabilities as generation mechanism of electrostatic solitary waves in the magnetotail, *Journal of Geophysical Research, 101*, 2685-2697, 1996.

2. Matsumoto, H., H. Kojima, Y. Kasaba, T. Miyake, R. R. Anderson, and T. Mukai, Plasma waves in the upstream and bow shock regions observed by Geotail, *Advances in Space Research, 20*, 683-693, 1997.

3. Miyake, T., Y. Omura, H. Matsumoto, and H. Kojima, Two-dimensional simulations of electrostatic solitary waves observed by Geotail spacecraft, *Journal of Geophysical Research, 103*, 11841-11850, 1998.

4. Miyake, T., Y. Omura, H. Matsumoto, and H. Kojima, Electrostatic particle simulations of solitary waves in the auroral region, *submitted to Journal of Geophysical Research*, 1999.

Symposium Proceedings

1. Miyake, T., Y. Omura, H. Matsumoto, and H. Kojima, Two-dimensional computer experiments of Electrostatic Solitary Waves (ESW) in the Earth's magnetotail (in Japanese), *KDK Research Report '94*, 117-120, 1995

2. Omura, Y., H. Matsumoto, T. Miyake, M. Ashout-Abdalla, and H. Kojima, Electron Beam Instabilities as Generation Mechanism of Electronstatic Solitary Waves in the Magnetotail (in Japanese), *KDK Research Report '94*, 113-116, 1995

3. Miyake, T., Y. Omura, H. Matsumoto, and H. Kojima, Two-dimensional computer experiments of Electrostatic Solitary Waves observed by GEOTAIL Spacecraft (in Japanese), *KDK Research Report '95*, 115-118, 1996

4. Miyake, T., Y. Omura, H. Matsumoto, and H. Kojima, Computer Experiments of Electrostatic Solitary Waves Observed by GEOTAIL Spacecraft, *The Fifth International School/Symposium for Space Simulations*, 51-54, 1997.

5. Miyake, T., Y. Omura, H. Matsumoto, and H. Kojima, Computer Experiments of Electrostatic Solitary Waves Observed by GEOTAIL Spacecraft (in Japanese), *KDK Research Report '97*, 59-62, 1998

6. Miyake, T., Y. Omura, H. Matsumoto, and H. Kojima, Computer Experiments of Electrostatic Solitary Waves Observed by GEOTAIL Spacecraft (in Japanese), *KDK Research Report '98*, 69-73, 1999

Oral Presentations

1. Miyake, T., Y. Omura, H. Matsumoto, and H. Kojima, Two-dimensional computer experiments of Electrostatic Solitary Waves (ESW) in the Earth's magnetotail (in Japanese), *97th Society of Geomagnetism and Earth, Planetary, and Space Sciences (SGEPSS)*, Tokyo, Mar. 1995.

2. Miyake, T., Y. Omura, H. Matsumoto, and H. Kojima, Effects of the ambient magnetic field on the formation mechanism of ESW from the electron beam instability : two-dimensional electrostatic particle simulations (in Japanese), *98th Society of Geomagnetism and Earth, Planetary, and Space Sciences (SGEPSS)*, Kyoto, Oct. 1995.

3. Miyake, T., Y. Omura, H. Matsumoto, and H. Kojima, Two-Dimensional Computer Experiments of Electrostatic Solitary Waves observed by GEOTAIL (in Japanese), *GEOTAIL Joint Workshop*, ISAS, Oct. 1995.

4. Miyake, T., Y. Omura, H. Matsumoto, and H. Kojima, Two-Dimensional Computer Experiments of Electrostatic Solitary Waves observed by GEOTAIL, *American Geophysical Union, Fall Meeting*, San Francisco, Dec. 1995.

5. Miyake, T., Y. Omura, H. Matsumoto, and H. Kojima, Two-dimensional electrostatic particle simulations of the spatial structure of potentials observed by Geotail spacecraft : formation mechanism of ESW (in Japanese), *99th Society of Geomagnetism and Earth, Planetary, and Space Sciences (SGEPSS)*, Osaka, Mar. 1996.

6. Miyake, T., Y. Omura, and H. Matsumoto, Computer experiments of the formation mechanism of ESW with electrostatic Vlasov code (in Japanese), *100th Society of Geomagnetism and Earth, Planetary, and Space Sciences (SGEPSS)*, Osaka, Oct. 1996.

7. Miyake, T., Y. Omura, H. Matsumoto, and H. Kojima, Computer Experiments of Electrostatic Solitary Waves observed by GEOTAIL Spacecraft, *Chapman Conference*, Kanazawa, Nov. 1996.

8. Miyake, T., Y. Omura, H. Matsumoto, and H. Kojima, ESW formation from the electron beam instability : effects of the numerical thermal fluctuations in particle simulations (in Japanese), *101st Society of Geomagnetism and Earth, Planetary, and Space Sciences (SGEPSS)*, Nagoya, Mar. 1997.

9. Miyake, T., Y. Omura, H. Matsumoto, and H. Kojima, Effects of the ambient magnetic field on formation mechanism of ESW : two-dimensional electrostatic particle simulations (in Japanese), *102nd Society of Geomagnetism and Earth, Planetary, and Space Sciences (SGEPSS)*, Hokkaido, Oct. 1997.

10. Miyake, T., Y. Omura, H. Matsumoto, and H. Kojima, Two-dimensional Simulations of Electrostatic Solitary Waves observed by GEOTAIL Spacecraft, *3rd GEOTAIL Joint Workshop*, ISAS, Oct. 1997.

11. Miyake, T., Y. Omura, H. Matsumoto, and H. Kojima, Two-dimensional Simulations of Electrostatic Solitary Waves observed by GEOTAIL Spacecraft, *American Geophysical Union, Fall Meeting*, San Francisco, Dec. 1997.

12. Miyake, T., Y. Omura, H. Matsumoto, and H. Kojima, Two-dimensional computer experiments of the electron two-stream instability (in Japanese), *103rd Society of Geomagnetism and Earth, Planetary, and Space Sciences (SGEPSS)*, Tokyo, May 1998.

13. Miyake, T., Y. Omura, and H. Matsumoto, Computer simulations of two-dimensional potential structures in the auroral region, *COSPAR Meeting*, Nagoya, Jul. 1998.

14. Miyake, T., Y. Omura, and H. Matsumoto, Particle simulations of ESW in the auroral region (in Japanese), *104th Society of Geomagnetism and Earth, Planetary, and Space Sciences (SGEPSS)*, Ibaragi, Nov. 1998.

15. Miyake, T., Y. Omura, and H. Matsumoto, Particle simulations of ESW in the auroral region (in Japanese), *105th Society of Geomagnetism and Earth, Planetary, and Space Sciences (SGEPSS)*, Tokyo, Jun. 1999.

16. Miyake, T., Y. Omura, and H. Matsumoto, Particle simulations of solitary waves in the auroral region, *IUGG99 Conference*, Birmingham, Jul. 1999.

17. Miyake, T., Y. Omura, and H. Matsumoto, Particle simulations of solitary waves in the auroral region (in Japanese), *106th Society of Geomagnetism and Earth, Planetary, and Space Sciences (SGEPSS)*, Miyagi, Nov. 1999.